

INVESTIGATIONS OF PHASE TRANSFORMATIONS IN AISI 5160  
STEEL AND CERIA PARTIALLY STABILIZED ZIRCONIA VIA  
ELECTRON BACKSCATTER DIFFRACTION BASED TECHNIQUES

BY

WENXIA TAN

A THESIS

SUBMITTED TO THE FACULTY OF

ALFRED UNIVERSITY

IN PARTIAL FULFILLMENT OF THE REQUIREMENTS  
FOR THE DEGREE OF

DOCTOR OF PHILOSOPHY

IN

MATERIALS SCIENCE AND ENGINEERING

ALFRED, NEW YORK

DECEMBER, 2017

INVESTIGATIONS OF PHASE TRANSFORMATIONS IN AISI 5160 STEEL  
AND CERIA PARTIALLY STABILIZED ZIRCONIA VIA ELECTRON  
BACKSCATTER DIFFRACTION BASED TECHNIQUES

BY

WENXIA TAN

B.S. TIANJIN UNIVERSITY (2005)

M.S. HUAZHONG UNIVERSITY OF SCI. AND TECH. (2011)

SIGNATURE OF AUTHOR \_\_\_\_\_

APPROVED BY \_\_\_\_\_

DAVID W. LIPKE, ADVISOR

\_\_\_\_\_  
ERIC J. PAYTON, ADVISORY COMMITTEE

\_\_\_\_\_  
SCOTT T. MISTURE, ADVISORY COMMITTEE

\_\_\_\_\_  
STEVEN M. PILGRIM, ADVISORY COMMITTEE

\_\_\_\_\_  
S. K. SUNDARAM, ADVISORY COMMITTEE

\_\_\_\_\_  
HOLLY S. SHULMAN, CHAIR, ORAL THESIS DEFENSE

ACCEPTED BY \_\_\_\_\_

ALASTAIR N. CORMACK, INTERIM DEAN  
KAZUO INAMORI SCHOOL OF ENGINEERING

ACCEPTED BY \_\_\_\_\_

JAY CERIO, DEAN OF GRADUATE  
AND CONTINUING STUDIES  
ALFRED UNIVERSITY

Alfred University theses are copyright protected and may be used for education or personal research only. Reproduction or distribution in part or whole is prohibited without written permission from the author.

Signature page may be viewed at Scholes Library, New York State College of Ceramics, Alfred University, Alfred, New York.

## ACKNOWLEDGMENTS

Firstly, I would like to express my sincerest gratitude to my advisor Dr. David Lipke for the continuous support of my Ph.D. study. His patience, motivation, and immense knowledge influenced me much. His guidance helped me throughout the research and writing of this thesis. I'm very grateful to be a student of him.

I would also like to thank my former advisor Dr. Eric Payton for his guidance during the first one and a half year of my Ph.D. studies. Even after his departure from Alfred, I still got valuable suggestions from him.

Besides my advisor, I would like to thank the professors in my thesis committee: Dr. Misture, Dr. Pilgrim, and Dr. Sundaram, for their insightful comments and encouragement, and for the tough questions which inspired me to broaden my research from different perspectives.

My hearty thanks also go to Gerald Wynick, Swavek Zdzieszynski, Katie Decker, James Thiebaud, and many others, who trained me to operate the research facilities or gave me useful informations. With their experienced assistance and suggestions, the research was conducted professionally and smoothly.

I thank my fellow groupmates and friends for the stimulating discussions, for all the assistance with experiments, and for all the fun we have had in the past four years.

Last but not the least, I would like to thank my family for supporting me spiritually throughout my Ph.D. studying and my life on the whole. Without their support, I would not have survived mentally to be a successful Ph.D. student.

## TABLE OF CONTENTS

	<b>Page</b>
ACKNOWLEDGMENTS .....	III
TABLE OF CONTENTS.....	IV
LIST OF TABLES .....	VI
LIST OF FIGURES .....	VII
ABSTRACT.....	XI
I INTRODUCTION .....	1
A. Background on EBSD.....	2
B. Local Misorientation.....	12
C. Martensitic Transformation .....	16
II ON QUANTITATIVELY IDENTIFYING DIFFERENT CONSTITUENTS IN MULTICOMPONENT STEEL MICROSTRUCTURES BY EBSD .....	20
A. Introduction.....	20
1. Separation of Different Constituents for Steels by EBSD.....	22
B. Experimental Procedure.....	23
1. Isothermal Heat Treatment .....	23
2. Sample Preparation and Microhardness.....	26
3. Electron Microscopy and EBSD Analysis.....	26
4. Optical Microscopy and Color Segmentation.....	27
5. Calculation of volume fractions according to ASTM E562 .....	28
C. Results and Discussion .....	29
1. Results.....	29
2. Discussion.....	45
D. Conclusions.....	47
III EBSD INVESTIGATION OF TETRAGONAL TO MONOCLINIC PHASE TRANSFORMATION IN 10 MOL% CERIA DOPED ZIRCONIA.....	49

A. Introduction.....	49
B. Experimental Procedure.....	57
1. Sample Preparation and Phase Identification .....	57
2. PTMT Calculation .....	58
3. Electron Microscopy.....	58
C. Results and Discussion .....	59
1. Results.....	59
2. Discussion.....	70
D. Conclusion .....	75
IV SUMMARY AND CONCLUSIONS .....	77
V FUTURE WORK.....	81
REFERENCES .....	83
APPENDICES .....	89
A. The calculation of shape strain and the lattice invariant strain for martensitic transformation.....	89
B. The procedure of simulating pole figure in PTCLab to represent orientation relationship for tetragonal to monoclinic phase transformation in 10 mol% Ce-ZrO <sub>2</sub> . ....	91
C. TSL OIM DC 7 software setting ahead of EBSD data collection for 10 mol% Ce-ZrO <sub>2</sub> . ....	91
D. Software setting of plotting pole figures in TSL OIM Analysis 7 to show orientation relationship for tetragonal to monoclinic phase transformation in 10 mol% Ce-ZrO <sub>2</sub> experimentally.....	92
E. An example to show the band finding via Hough transform .....	92

## LIST OF TABLES

		<b>Page</b>
<b>Table I.</b>	Salt Bath Time and Temperature, as well as the Corresponding Vickers Hardness and Identified Microstructure Constituents.....	25
<b>Table II.</b>	Comparison of Volume Fraction Results by Color Etching and ASTM .....	31
<b>Table III:</b>	Comparison of Volume Fraction Results by KAM and ASTM .....	45
<b>Table IV.</b>	The Eight Variants for Correspondence A Following Hayakawa .....	53
<b>Table V:</b>	Lattice Parameters of Monoclinic and Tetragonal Phases 12mol% Ce-ZrO <sub>2</sub> <sup>60</sup> .....	56
<b>Table VI.</b>	Lattice Parameters of the Monoclinic and Tetragonal Ce-ZrO <sub>2</sub> Phases from the Closest Matching PDF Cards.....	60
<b>Table VII.</b>	PTCLab Output of the PTMT Calculation for Correspondence A .....	63
<b>Table VIII.</b>	PTCLab Output of the PTMT Calculation for Correspondence B .....	63
<b>Table IX.</b>	PTCLab Output of the PTMT Calculation for Correspondence C .....	64
<b>Table X.</b>	The Positions of the Ten Bands Located by Hough Transform, Together with Their Corresponding Reflectors, and the Information of the Reflectors in the Look-Up Table of the Tetragonal Phase in 10 mol% Ce-ZrO <sub>2</sub> .....	94

## LIST OF FIGURES

		Page
<b>Figure 1.</b>	The interaction of electron beam with sample, and where the backscattered electrons originate.....	3
<b>Figure 2.</b>	EBSD working procedure: (a) data collection; (b) Kikuchi pattern analysis to get the phase and orientation information of one point; (c) create maps, plots or charts for a region or several grains.....	4
<b>Figure 3.</b>	The schematic of showing how a Kikuchi pattern forms. ....	5
<b>Figure 4.</b>	(a) stereographic projection of a rectangular sheet of polycrystalline material which has a cubic crystal structure; (b) projection of the (100), (010), and (001) lattice planes for an arbitrarily oriented grain within the sample; (c) pole figure showing the discrete poles of the (100), (010), and (001) lattice planes for all grains in the sample; (d) pole figure showing the pole densities of the (100), (010), and (001) lattice planes for all grains in the sample. ....	8
<b>Figure 5.</b>	The relationships among the sample coordinates ( $w_i$ ), crystal coordinates ( $u_i$ ), and the phosphor screen coordinates ( $v_i$ ).....	9
<b>Figure 6.</b>	(a) the discrete inverse pole figure (IPF) of sample normal direction; (b) the corresponding IPF map of an AISI 5160 steel sample showing the pearlite microstructure and the distribution of the sample normal direction [001] in each grain.....	10
<b>Figure 7.</b>	The pole figures representing the parallel relationships of one orientation relationship between the parent and product phases during the tetragonal to monoclinic phase transformation in a zirconia sample.....	11
<b>Figure 8.</b>	IQ map of a pearlite microstructure from the AISI 5160 steel after austenization at 850°C for 15 minutes and then salt bath at 450°C for 60 seconds. ....	13
<b>Figure 9.</b>	The schematic of (a) the 2 <sup>nd</sup> nearest neighbor Kernel, hexagonal point; (b) the 1 <sup>st</sup> nearest neighbor Kernel, square point.....	14
<b>Figure 10.</b>	The schematic of the Kernel and the calculation of the KAM value (in degrees)....	15

<b>Figure 11.</b>	The 3NN KAM map of the bainitic microstructure from the AISI 5160 steel after austenization at 850°C for 15 minutes and then salt bath at 300°C for 30 minutes.....	16
<b>Figure 12.</b>	(a) Conventional FCC unit cell; (b) Relation between FCC and BCT cells of austenite; (c) BCT cell of austenite; (d) Bain strain deforming the BCT austenite lattice into a BCC martensite lattice .....	17
<b>Figure 13.</b>	Optical micrograph of the surface relief after martensitic transformation on a well-polished zirconia sample surface.....	18
<b>Figure 14.</b>	Schematic of the thermal processing steps for AISI 5160. Step 1: austenize, Step 2: soak, Step 3: quench. ....	26
<b>Figure 15.</b>	The schematic illustration of the KAM method. ....	27
<b>Figure 16.</b>	IQ maps of (a) Sample 5b and (b) Sample 7a.....	29
<b>Figure 17.</b>	Color enhanced optical images (left) and the corresponding images after segmentation by GIMP (right) (a) Sample 5b in Table III; (b) Sample 8b in Table III; (c) Sample 10b in Table III.....	32
<b>Figure 18.</b>	Time-temperature-transformation (TTT) diagram of the AISI 5160 steel .....	33
<b>Figure 19.</b>	The SE image and IQ+KAM maps at 1NN, 2NN, 3NN and 10NN of (a) Sample 8a; (b) Sample 2a; (c) Sample 12a; (d) Sample 6a in Table I.....	34
<b>Figure 20.</b>	(a) SE images of Sample 1a; (b) IPF maps of Sample 1a; (c) SE images of Sample 11a; (d) IPF maps of Sample 11a in Table I. ....	36
<b>Figure 21.</b>	KAM maps at 1NN, 2NN, 3NN and 10NN of (a) Sample 1a; and (b) Sample 11a in Table III .....	37
<b>Figure 22.</b>	KAM frequency distribution plots of Sample 2a in Table I. ....	38
<b>Figure 23.</b>	FWHM of KAM distribution vs NN# plots for (a) 300°C group, perimeter offers; (b) 300°C group, all points in the kernel offer; (c) 400°C group, perimeter offers; (d) 400°C group, all points in the kernel offer; (e) 450°C group, perimeter offers; (f) 450°C group, all points in the kernel offer.....	39
<b>Figure 24.</b>	(a) FWHM vs Hardness plots for 450°C group; (b) the change of slope, intercept and R-squared value with different curve number for 450°C group;	

(c) FWHM vs Hardness plots for 300°C group; (d) the change of slope, intercept and R-squared value with different curve number for 300°C group. ...40

**Figure 25.** (a) Linear relationship between FWHM and Hardness with the influence of NN#; (b) the change of slope, intercept and R-squared value with different NN# for all samples in series *a*. .....41

**Figure 26.** The typical  $d\lambda/d(NN\#)$  vs. NN# plots for Sample 2a (bainitic microstructure), 6a (martensitic microstructure), 8a (roughly 80% ferrite and 20% perlite) and 10a (perlite microstructure) in Table I. ....43

**Figure 27.** Fraction of the KAM values less than  $1^\circ$  (blue) in the KAM maps ( $\lambda$ ) vs NN# and 1<sup>st</sup> derivative  $d\lambda/d(NN\#)$  vs. NN# curves for (a) Sample 5b; and (b) Sample 7a both containing martensite and ferrite. ....45

**Figure 28.** The schematic of the three correspondences for one case of the tetragonal to monoclinic transformation in zirconia, and the two different ORs in each correspondence. ....52

**Figure 29.** The phase diagram of CeO<sub>2</sub>-ZrO<sub>2</sub>. ....57

**Figure 30.** XRD data of the 10 mol% Ceria Doped Zirconia sample. Cu K $\alpha_1$  radiation ( $\lambda=1.54 \text{ \AA}$ ), scanning rate 0.01°/s. ....59

**Figure 31.** Secondary electron image of the polished Ce-ZrO<sub>2</sub> sample surface indicating porous structure. ....60

**Figure 32.** The schematic of the deformation of unit cells during the tetragonal to monoclinic transformation for correspondence C of the 10 mol% Ce-ZrO<sub>2</sub> sample, (a) the tetragonal unit cell; (b) co-ordinate transformation from tetragonal unit cell with lattice parameters  $a_{t1}$ ,  $b_{t1}$ , and  $c_{t1}$  to tetragonal unit cell with lattice parameters  $a_{t2}$ ,  $b_{t2}$ , and  $c_{t2}$ ; (c) after Bain strain, the transformed monoclinic unit cell. ....61

**Figure 33.** The simulated pole figures, to denote the parallel relationships in OR A-1, A-2, B-1, B-2, C-1, and C-2. ....65

**Figure 34.** (a) The IQ + phase map and (b) the IQ + IPF map of a  $12.54 \times 36.67 \mu\text{m}^2$  region on the sample surface. ....66

**Figure 35.** (a) The IQ + phase map and (b) the IQ + IPF map of another  $12.54 \times 36.67 \mu\text{m}^2$  region on the sample surface. ....67

**Figure 36.** The EBSD maps and the pole figures of the multi-oriented martensite plates in a tetragonal grain (a) the phase map; (b) the IPF map of the extracted tetragonal grain; and (c) the IPF map after rotation; (d) the (100), (001), [100], [010] and [001] pole figures of the monoclinic phase after rotation.....68

**Figure 37.** The EBSD maps and the pole figures of the needle like martensite plates in another tetragonal grain (a) the phase map; (b) the IPF map of the extracted tetragonal grain; and (c) the IPF map after rotation; (d) the (100), (001), [100], [010] and [001] pole figures of the monoclinic phase after rotation.....69

**Figure 38.** The EBSD maps and the pole figures of the twin-related martensite laths in a tetragonal grain (a) the phase map; (b) the IPF map of the extracted tetragonal grain; and (c) the IPF map after rotation; (d) the (100), (001), [100], [010] and [001] pole figures of the monoclinic phase after rotation.....70

**Figure 39.** The schematic of the twin-related needle-like martensite plate pair. The arrangement is predicted by PTMT .....72

**Figure 40.** (a) the Kikuchi pattern after background noise subtraction; (b) the band finding via Hough transform; (c) the indexing of the pattern with CI and Fit value; and (d) the setting of the Hough page.....93

## ABSTRACT

In this dissertation, electron backscatter diffraction (EBSD) is applied to study the phase transformation in AISI 5160 steel and 10 mol% Ce doped ZrO<sub>2</sub>. For AISI 5160 steel, quantitative characterization of the volume fractions and spatial arrangements of the major constituents of microstructure is needed for continued progress toward the next generation of advanced steels. EBSD data can be used to simultaneously characterize orientation relationships as well as determine the volume fraction and size of grains of retained austenite and ferrite due to the difference in diffraction patterns caused by the different crystal structures of the two phases; however, distinguishing among martensite, ferrite, pearlite, and bainite using EBSD remains a challenge. A detailed analysis of the capabilities of EBSD-based methods for separation of the individual microstructural constituents is performed on samples of a commercial steel - AISI 5160. It is demonstrated that kernel average misorientation (KAM) data can be used to distinguish and quantify the constituents.

Zirconia is one of many materials that experiences a displacive phase transformation. In zirconia, the tetragonal to monoclinic martensitic transformation can be induced either thermally or by applied stress. Since transformation from tetragonal to monoclinic phase is accompanied by a volume increase, it may be engineered to utilize the martensitic transformation as a toughening mechanism. In the present work, EBSD was used to observe the morphology and orientation relationships simultaneously. According to the EBSD study, all six orientation relationships were present. The theoretical predictions based on the phenomenological theory of martensitic transformations were also calculated for 10 mol% ceria doped zirconia and compared with experimental findings. The calculation of the strains showed that the correspondence B has the lowest lattice invariant strain among the three correspondences, and for the shape strain, the three correspondences are nearly equivalent.

## I. INTRODUCTION

The study of structure-property relationships lies at the heart of materials science. Material microstructures are traditionally characterized by the morphology and distribution of constituent phases, as revealed in optical, scanning electron, and transmission electron micrographs. The traditional description of microstructure of a crystalline material specifies a host of parameters, such as dislocation substructure (overall density and distribution), grain structure (size, size distribution, and shape), second phase content (volume fraction, size, and distribution) and interface characteristics (grain boundaries and interphase boundaries). When employed as an additional characterization technique to scanning electron microscopy (SEM), electron backscatter diffraction (EBSD) enables individual grain orientations, local texture, point-to-point orientation correlations, and phase identification and distributions to be determined routinely on the surfaces of bulk polycrystals, which can provide a detailed description of microstructure of a crystalline material.

For steel, high variability among various techniques is often observed for the measurement of volume fractions of microstructural constituents. By EBSD, quantitatively distinguishing austenite from ferrite is straightforward due to their different crystal structures. However, distinguishing phase transformation products such as martensite, bainite, and ferrite is a much more challenging problem because they are comprised of phases featuring similar crystal symmetries which cannot be easily distinguished by EBSD. In the first part of this work, a detailed evaluation of the capabilities of EBSD-based methods for segmentation of the individual microstructural constituents is presented.

For ceramics, the martensitic transformation - especially the tetragonal to monoclinic transformation in zirconia - can enhance the fracture toughness owing to the effects of transformation toughening.<sup>1</sup> Transformation toughening is a phenomenon that manipulates the shape and volume distortion of the martensitic transformation as a toughening mechanism.<sup>1</sup> In the second part of this work, EBSD is used to observe the morphology and to analyze the orientation relationships between parent and product phases for a 10 mol% ceria doped zirconia sample. Theoretical predictions based on the phenomenological theory of martensite transformations (PTMT) were also calculated for this sample. The study via EBSD can observe the micron-scale regions on the sample surface and compare the microstructure and orientation relationships simultaneously, which is a valuable complement to the prior study of martensitic transformations in ceramics by TEM and AFM and could facilitate a more comprehensive understanding of the martensitic transformation in zirconia.

## **A. Background on EBSD**

The origin of EBSD technique lies with the work of Kikuchi who, in 1928, first observed diffraction patterns from diffuse scattering of electrons.<sup>2</sup> Full automation of EBSD in 1991<sup>3</sup> led to the mapping of crystal orientation over a sample surface and to a new metallography named "Orientation Imaging Microscopy". It was this innovation that gave rise to the current rapid growth and eventual full commercialization of EBSD.<sup>4</sup>

When incident electrons enter the specimen in SEM, they are scattered inelastically or elastically and emit several different kinds of signal, such as secondary electrons, backscattered electrons and characteristic x-rays.<sup>5</sup> Figure 1 shows the schematic of the interaction of electron beam with sample, and how deep in the interaction region the backscattered electrons originate.

The depth will be influenced by the settings of SEM, such as accelerating voltage, and sample itself. The backscattered electrons are high-energy electrons and can be used for diffraction analysis in SEM.

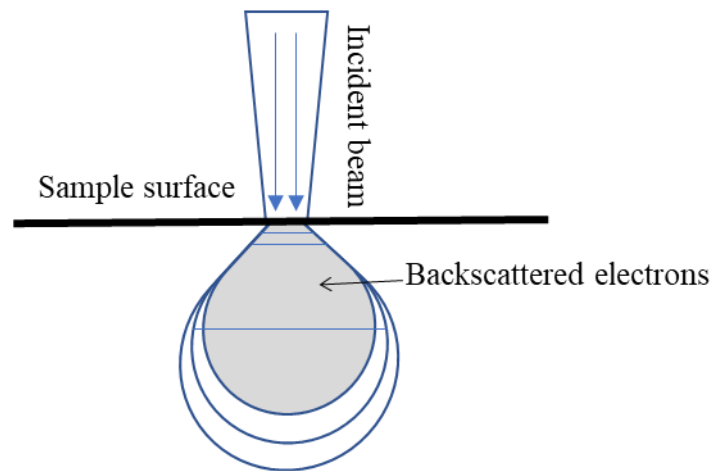


**Figure 1.** The interaction of electron beam with sample, and where the backscattered electrons originate.

Figure 2 shows how the automatic EBSD technique works. A sample is placed in an SEM chamber and tilted  $70^\circ$  from normal incidence of the electron beam so that the maximum number of escaped backscattered electrons can be collected by the EBSD detector (as shown on the left of the sample in Figure 2a).

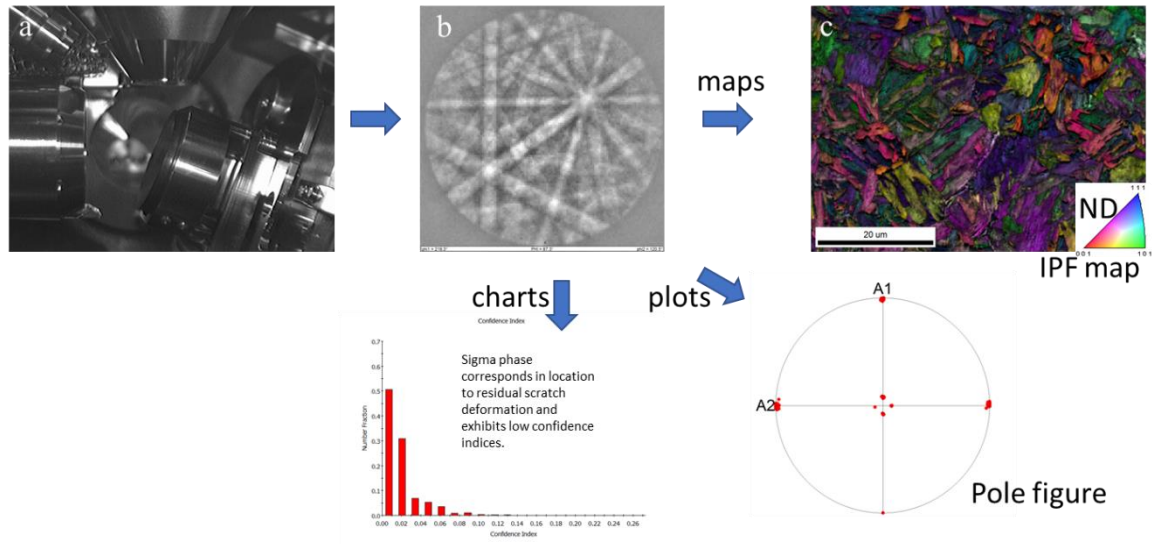


**Figure 2.** EBSD working procedure: (a) data collection; (b) Kikuchi pattern analysis to get the phase and orientation information of one point; (c) create maps, plots or charts for a region or several grains.

The incident electron beam interacts with the sample surface and is scattered in all directions. Figure 3 shows the schematic of how a Kikuchi band forms. When the scattered electrons at certain lattice planes satisfy Bragg's law, they will be diffracted and form strong beams. The diffracted electrons form two Kossel cones on the lattice plane. One is closer to the incident beam, which is called the deficient cone, and the other is far away from the incident beam, which is called the excess cone.<sup>6</sup> Since the diffraction angle is very small, the two cones appear on the screen of the EBSD detector as two parallel lines. We call these two parallel lines a "band". For one set of lattice planes (based on the symmetry of the plane in the crystal structure) which satisfy the Bragg's law, the bands intersect at one point. The point is defined as a "pole"/zone axis. For a crystal structure, there are at least several sets of lattice planes which satisfy Bragg's law and form intersected bands at different locations of the EBSD screen. All the bands on the screen together are called a Kikuchi pattern and at each point of the sample surface, it forms a Kikuchi pattern

(Figure 3). From Kikuchi pattern analysis, the phase and orientation information can be obtained for any point.

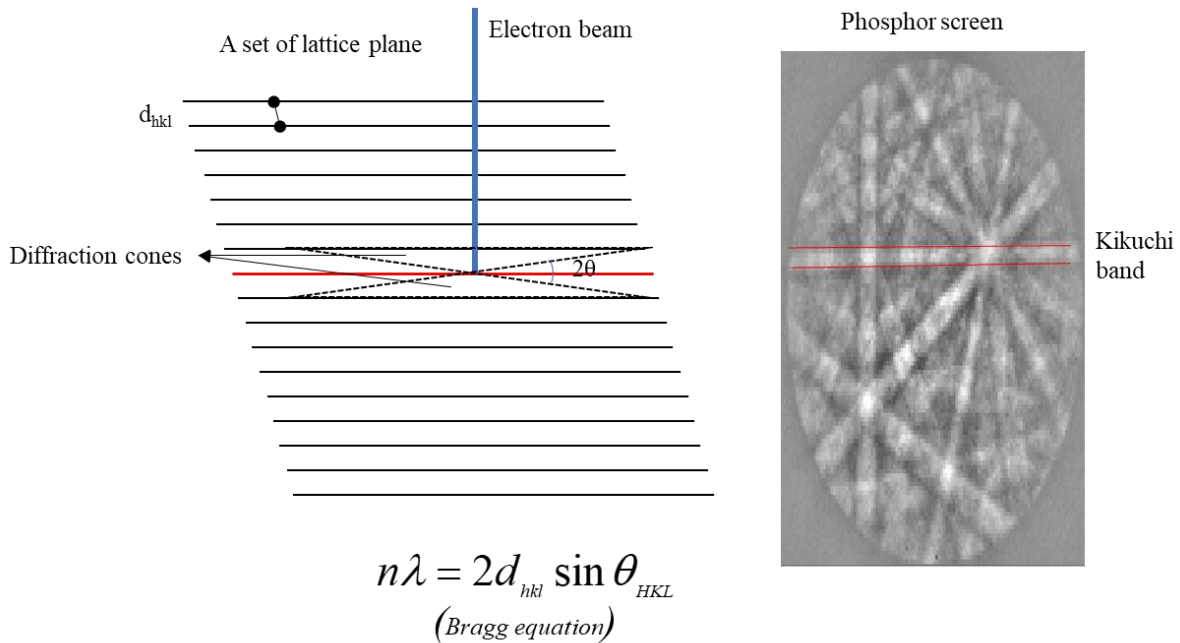


**Figure 3.** The schematic of showing how a Kikuchi pattern forms.

The automatic Kikuchi pattern indexing routine used in this work implements Wright's manual indexing methods for individual EBSD patterns.<sup>7,8</sup> The brief principle of those method is to measure the interplanar angle and the bandwidth angle of the Kikuchi pattern, and then compare with the calculated theoretical values of them to get the orientation and phase information. The detailed steps of the indexing routine are:

- a) construct an interplanar angle look-up table with related bandwidth angle for the crystal;
- b) calculate all the interplanar angles and the bandwidth angles from the bands in the Kikuchi pattern;

- c) generate a set of possible lattice plane family pairs for each of the three band pairs (a band pair correspond to an interplanar angle) by checking the look-up table for theoretical interplanar angles which lie within a given range (angular tolerance) of their calculated interplanar angle;
- d) reduce the three sets of lattice plane family pairs to a single set of legitimate triplets;
- e) identify the exact (hkl) indices within this set of plane family triplets. The rule for identifying is that not only must the interplanar angles be similar, but the triple products of the (hkl) indices and the triple products of the band normals must have the same sign. Two additional criteria are relevant. Linear band triplets must be assigned (hkl) whose triple products are zero, bandwidth angle must be considered if there is a symmetry for two bands;
- f) once a set of (hkl) triplets has been generated for a band triplet, the lattice orientation associated with each (hkl) triplet is calculated;
- g) a check is then made to ensure that each member of the set is unique. During this process, a check is made to see how well the experimental bandwidth angles fit the theoretical ones;
- h) each calculated lattice orientation from Step f is a possible solution. A search is made through all the sets of solutions obtained from all possible band triplets. Solutions which are similar are grouped together. Two solutions are considered similar if the misorientation angle between them is less than the tolerance (the same as the one in Step c);
- i) once the solutions groups are formed, they are ranked by the number of times the group appears in all the triplet solution sets

SEM-based EBSD can collect data for microscale regions on the polycrystalline sample surface. Based on the EBSD raw data, the orientation maps, pole figures and graphs can be produced for analysis. SEM-based EBSD features three primary capabilities: i) local crystallographic analysis: texture analysis, orientation relationships, epitaxy, twinning, misorientation analysis, phase transformation texture reconstruction;<sup>9,10</sup> ii) microstructure characterization: grain size distribution, grain shape, quantitative phase distribution, recrystallization, deformation, characterization of cracks;<sup>11</sup> and, iii) local stress analysis, in-situ high temperature experiments and 3D EBSD.<sup>12,13</sup>

Texture indicates the occurrence of preferred crystal orientations. The presence and character of texture can be visually represented using pole figures. Figure 4 shows schematically a pole figure to present texture. As an example, a rectangular sheet of polycrystalline material which has a cubic crystal structure, is placed at the center of the projection sphere (as shown in Figure 4a). the “ND” is the normal direction of the sample surface, “RD” (A1) connotes the rolling direction and “TD” (A2) is the transverse direction. In the stereographic projection (as shown in Figure 4a), the ND pole is located at the center of the projection plane which is parallel to the sample surface, the RD (A1) pole is on the top, and TD (A2) pole is on the left. Figure 4b shows the projection of one grain in the sample. The three lattice planes (100), (010), and (001) belong to the {100} family and perpendicular to each other. The three planes normal extend to intersect with the projection sphere at certain positions. On the projection plane, there are three corresponding poles. Figure 4c shows the pole figure with discrete poles and Figure 4d shows the pole figure with pole densities in the way of contour lines. If the three lattice planes (100), (010),

and (001) of all the grains in the sample are projected and the sample has a texture, the pole figure will appear as Figure 4c or 4d show.

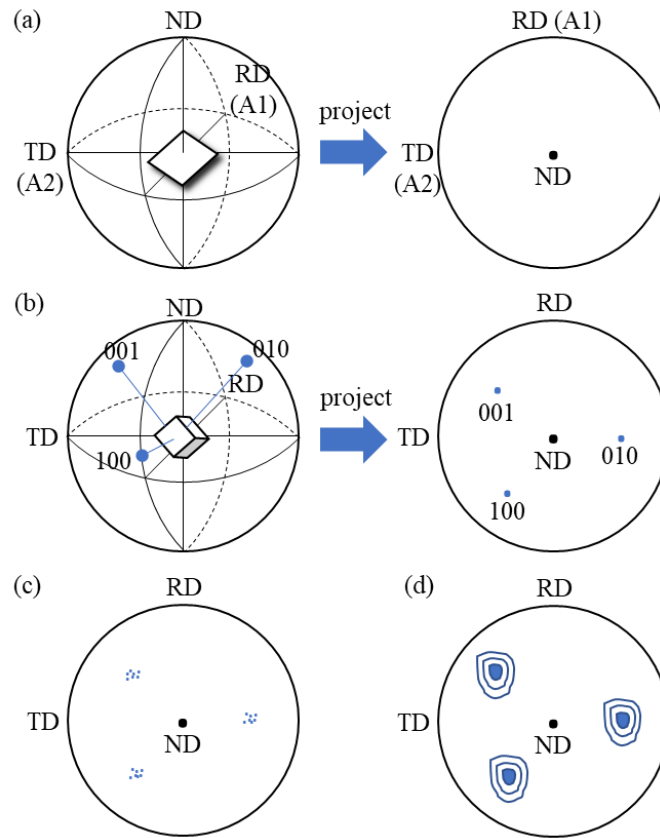


**Figure 4.** (a) stereographic projection of a rectangular sheet of polycrystalline material which has a cubic crystal structure; (b) projection of the (100), (010), and (001) lattice planes for an arbitrarily oriented grain within the sample; (c) pole figure showing the discrete poles of the (100), (010), and (001) lattice planes for all grains in the sample; (d) pole figure showing the pole densities of the (100), (010), and (001) lattice planes for all grains in the sample.

The analysis of the geometry of the EBSD pattern uses the sample coordinates as the reference frame, which greatly simplifies the data processing and increases the speed of data collection versus X-ray and neutron diffraction techniques.<sup>14</sup> Figure 5 shows the relationship among the sample coordinate, crystal coordinate, and the phosphor screen coordinates.<sup>15</sup>

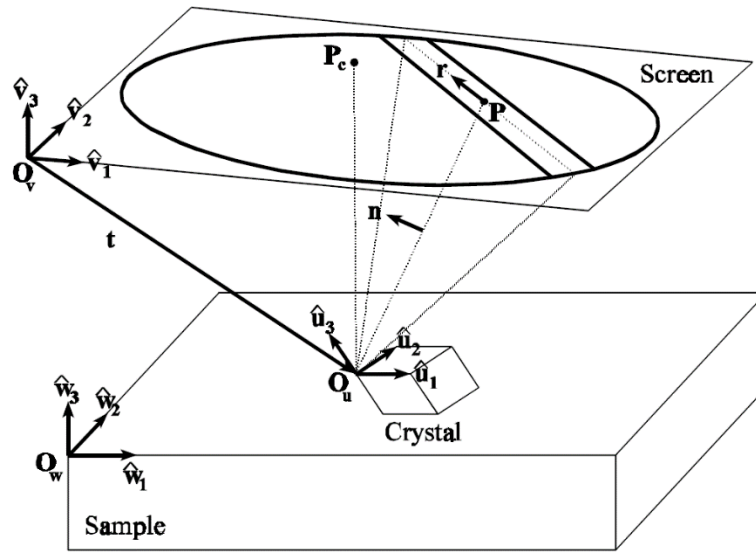


**Figure 5.** The relationships among the sample coordinates ( $\hat{w}_i$ ), crystal coordinates ( $\hat{u}_i$ ), and the phosphor screen coordinates ( $\hat{v}_i$ ). Reproduced with permission from ref. 10 (Copyright 1994 IMM).

Conventionally in X-ray and neutron diffraction techniques, pole figure analysis is included from the entire sample and needs a complex procedure to merge the physics of scattering and the diffraction intensities into an analysis of textures.<sup>16</sup> EBSD is a grain specific orientation technique, which can map or graphically represent local crystallographic information. For example, an inverse pole figure (IPF) shows the distribution of a selected direction (such as ND, RD or TD) of the sample in the crystal frame. The IPF map from EBSD is a color map which combines the IPF data and the microstructure information of certain surface region. Figure 6 shows the ND inverse pole figure and the corresponding IPF map of an AISI 5160 steel sample. Discrete pole figures reveal orientation relationships between the parent and product phases of a phase transformation or between twin-related grains.

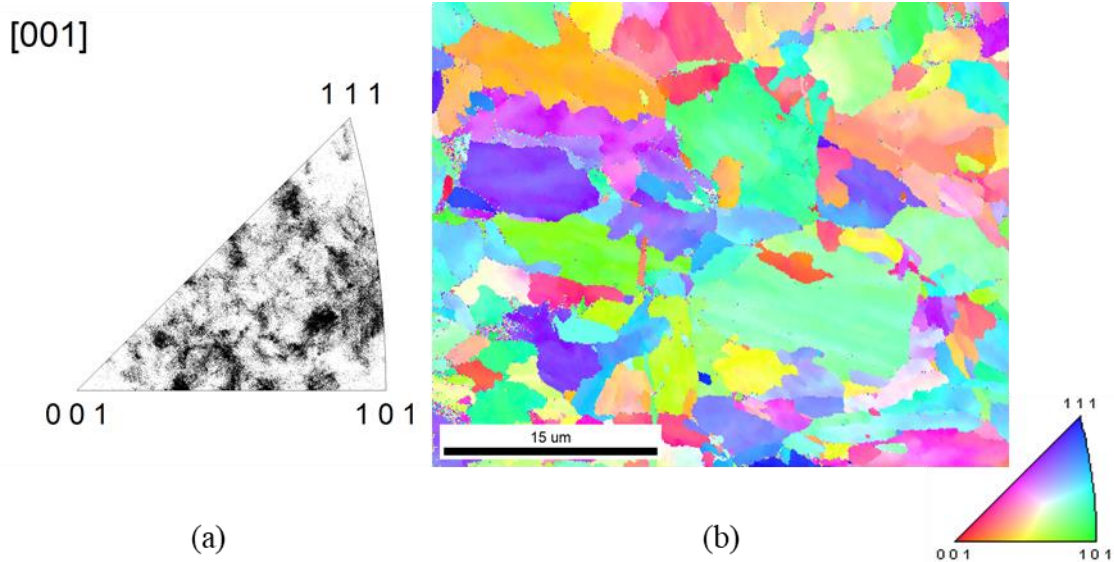


**Figure 6.** (a) the discrete inverse pole figure (IPF) of sample normal direction; (b) the corresponding IPF map of an AISI 5160 steel sample showing the pearlite microstructure and the distribution of the sample normal direction  $[001]$  in each grain.

The principle of plotting the pole figures to present the orientation relationships between the parent and product phases is that, taking one correspondence between the parent and product phases during the tetragonal to monoclinic phase transformation in zirconia as an example:

- a) suppose the coordinate of the tetragonal crystal is fixed and the  $c$  axis of the parent tetragonal crystal coincides with the sample normal direction, and  $a$  or  $b$  axis (these two axes are equivalent, and arbitrarily labeled for better understanding of the parallel relationships in the correspondences) intersect with the rolling direction of the sample with a  $45^\circ$  angular difference;
- b) for the correspondence, the  $c$  axis of the tetragonal crystal is parallel to the  $a$  axis of the monoclinic crystal, and the  $[1\bar{1}0]$  direction of the tetragonal crystal is parallel to  $b$  axis of the monoclinic crystal. For this correspondence, there are eight different variants -  $BCA$ ,  $\bar{B}\bar{C}\bar{A}$ ,  $\bar{C}BA$ ,  $C\bar{B}A$ ,  $\bar{B}C\bar{A}$ ,  $B\bar{C}\bar{A}$ ,  $\bar{C}\bar{B}\bar{A}$  and  $CB\bar{A}$ . Variant  $BCA$  means that the  $b$  axis of

the monoclinic crystal is equivalent to the  $[1\bar{1}0]$  direction of the tetragonal crystal,  $c$  axis of the monoclinic crystal is equivalent to the  $[110]$  direction of the tetragonal crystal,  $a$  axis of the monoclinic crystal is equivalent to the  $c$  axis of the tetragonal crystal. Variant  $\bar{B}\bar{C}A$  means that the  $b$  axis of monoclinic crystal is equivalent to the  $[\bar{1}10]$  direction of the tetragonal crystal,  $c$  axis of monoclinic crystal is equivalent to the  $[\bar{1}\bar{1}0]$  direction of the tetragonal crystal,  $a$  axis of monoclinic crystal is equivalent to the  $c$  axis of the tetragonal crystal. The other variants are defined in the same way according to the notations;

- c) according to the parallel relationships in different variants, such as in variant  $BCA$ , the  $a$  axis of the monoclinic crystal would coincide with the sample normal direction in the pole figure, and the  $b$  axis of the monoclinic crystal would coincide with the rolling direction (horizontal direction).

Figure 7 shows the pole figures representing the parallel relationships in one orientation relationship between the parent and product phases during the tetragonal to monoclinic phase transformation in a zirconia sample.

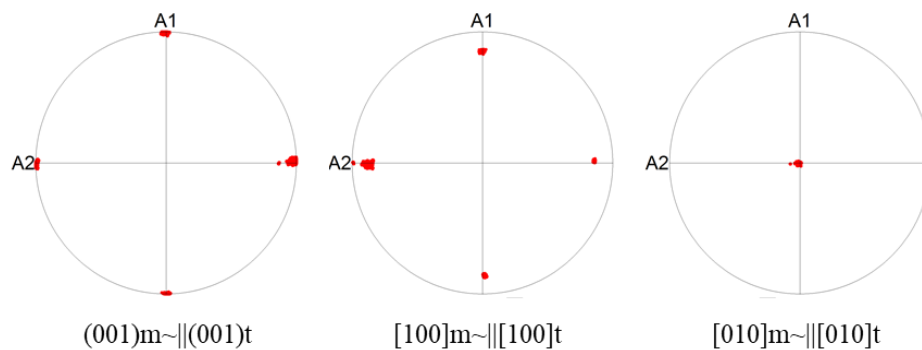


**Figure 7.** The pole figures representing the parallel relationships of one orientation relationship between the parent and product phases during the tetragonal to monoclinic phase transformation in a zirconia sample.

However, for identification of an unknown phase according to the Kikuchi pattern in EBSD, Energy-dispersive X-ray spectroscopy (EDS) or Wavelength-Dispersive X-Ray Spectroscopy (WDS) is needed to determine the chemical elements in the phase. The chemical information can narrow the range in searching the symmetry elements of the Kikuchi pattern and in identifying the point group of the phase in crystallographic databases. Phase identification by EBSD requires high quality (spatial resolution) Kikuchi pattern to accurately measure the interplanar angles and band width. Although advanced charge coupled device-based camera greatly improves the pattern quality,<sup>17</sup> the phase identification capability of EBSD is still much worse than X-ray diffraction technique.

Nevertheless, the advantage of using EBSD for phase identification is that it can map the phase distribution for the materials and simultaneously show the volume fraction of different phases in the legend of the phase map, such as retained austenite and ferrite within a steel sample. In addition, microstructure information such as the grain shape and grain size distribution information can be obtained from the EBSD map, such as IPF map, phase map, or image quality (IQ) map, a metric to describe the quality of the Kikuchi pattern that is often used to.

## **B. Local Misorientation**

Another valuable application of EBSD is identifying and quantifying residual strain. Strain can be divided into elastic strain and plastic strain, and they appear differently in the EBSD results. Gradients in elastic strain twist the crystal lattice, and manifest in the Kikuchi pattern by shifting the Kikuchi lines and zone axes by several pixels<sup>18,19</sup> or by blurring of the band edges in the Kikuchi pattern.<sup>20</sup> Plastic strain can be shown via the IQ method and the misorientation method.<sup>19</sup> Plastic strain occurs as dislocations or twinning. The plastic strain can degrade the pattern quality

as lattice bending around the defect area. Different amount of plastic strain appears in the image quality (IQ) map as the contrast of the map. Figure 8 shows the IQ map of a pearlite microstructure from an AISI 5160 steel after austenization at 850°C for 15 minutes and then salt bath at 450°C for 60 seconds. The areas which appear darker contain more strain than the bright area. However, the drawback of using IQ map to indicate plastic strain is that factors such as grain boundaries and sample preparation (mechanical polishing) can also influence the contrast of the IQ map, which makes it difficult to distinguish which factor is contributing to the IQ value.

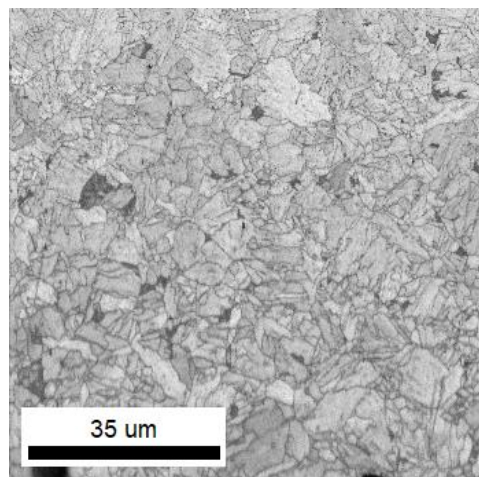


**Figure 8.** IQ map of a pearlite microstructure from the AISI 5160 steel after austenization at 850°C for 15 minutes and then salt bath at 450°C for 60 seconds.

Plastic strain can change the orientation in the polycrystalline material locally.<sup>21</sup> The local variation of the orientation is deemed “misorientation”. Misorientation is a good indicator of stored plastic strain in crystalline materials. Kernel is based on individual measurement points (pixels) in EBSD. There are two different shapes of the grid raster - hexagonal and square. A kernel can be defined for each pixel and consists of a set of neighboring points according to user specification. Pixel sets are typically defined by the number of nearest neighbors, although many alternative

pixel sets can be defined. The size of a kernel depends on the number of nearest neighbors (NN) taken in each pixel set. For EBSD patterns whose points are rastered in a hexagonal grid pattern the NN distance is constant, whereas a square grid pattern features variable NN distances (see Figure 9). As a result, hexagonal grid raster patterns are more frequently employed for misorientation mapping. Figure 9 shows the schematic of the kernel. The group of points/pixels in Figure 9 is named as a kernel. The size of the kernel depends on the nearest neighbor number (#NN), such as Figure 9a shows a 2NN kernel, and Figure 9b shows a 1NN kernel. The Kernel Average Misorientation measures the average misorientation between the center and other points in the kernel. In EBSD all the local misorientations can be mapped and the angular resolution of mapping local misorientation by standard EBSD system is on the order of  $0.5^\circ$ .<sup>21</sup>

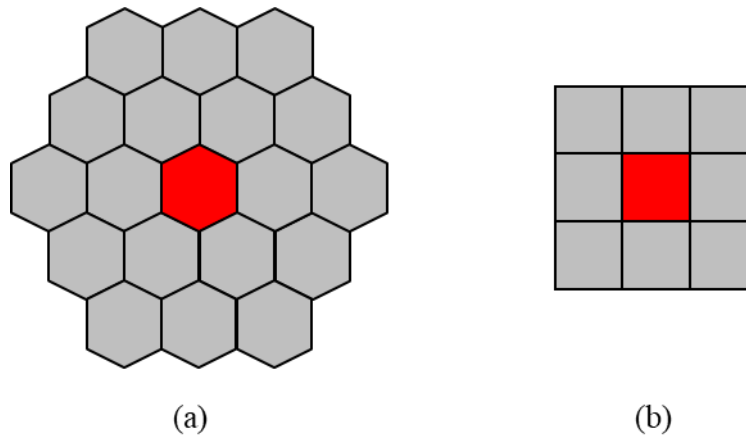


**Figure 9.** The schematic of (a) the 2<sup>nd</sup> nearest neighbor Kernel, hexagonal point; (b) the 1<sup>st</sup> nearest neighbor Kernel, square point.

Kernel Average Misorientation (KAM) mapping is often used for visualizing microscale plastic strain. The procedure for calculating the KAM value is that the average misorientation between the center of the kernel and all points, or between the center of the kernel and points on the perimeter of the kernel, is calculated with the condition that misorientations exceeding some

tolerance value are excluded from the averaging calculation. For example, misorientation around grain boundary or interphase boundary is usually larger than  $10^\circ$  and not related to plastic strain, and therefore are excluded from KAM calculations. Figure 10 shows the two ways to calculate of the KAM value. For ease of visualization, the calculated KAM value for the center point of the kernel can be assigned a color from an arbitrary color palette corresponding to KAM values up to the tolerance threshold. For a region of the sample, the allocated colors thus form a KAM map. Figure 11 shows a 3NN KAM map of the bainitic microstructure from the AISI 5160 steel after austenization at  $850^\circ\text{C}$  for 15 minutes and then soaked in salt bath at  $300^\circ\text{C}$  for 30 minutes.

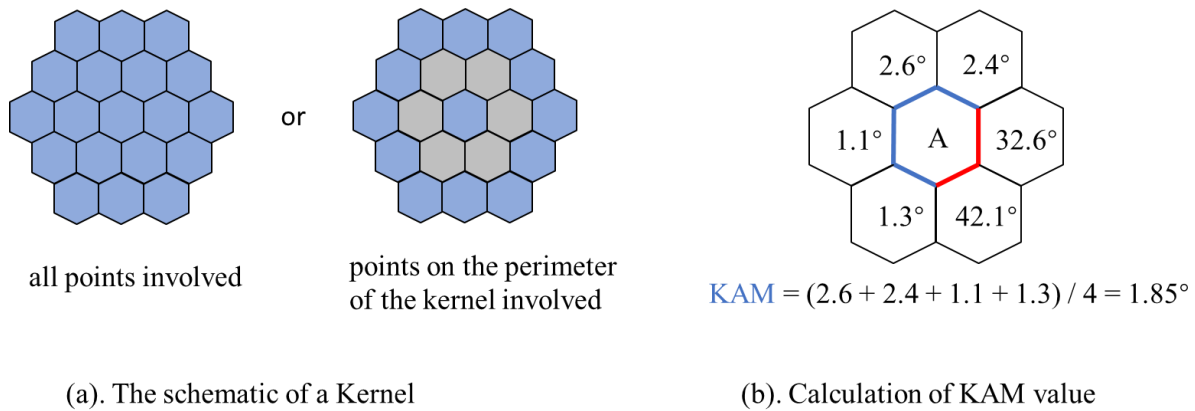


**Figure 10.** The schematic of the Kernel and the calculation of the KAM value (in degrees).

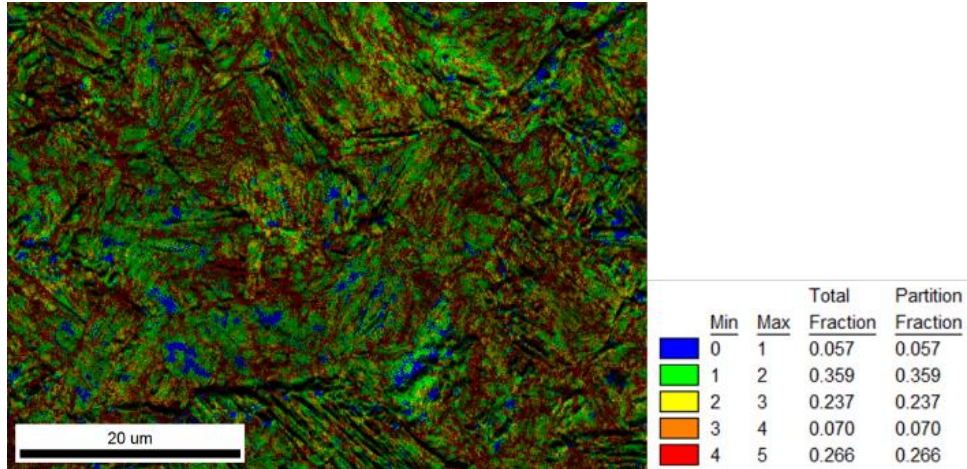


**Figure 11.** The 3NN KAM map of the bainitic microstructure from the AISI 5160 steel after austenization at 850°C for 15 minutes and then salt bath at 300°C for 30 minutes (Color legend shows average misorientation value ranges binned in one-degree increments).

### C. Martensitic Transformation

Martensitic transformations are defined as diffusionless, athermal phase transformations.<sup>22</sup> Attributed to this diffusionless quality is the speed of the transformation, which approaches 1100 m/s.<sup>22</sup> This velocity does not allow substantial diffusion to occur across microstructural length scales.<sup>23</sup> The “diffusionless” nature of martensitic transformations means that the movement of atoms must be coordinated, and that the parent and product lattices must have some correspondences composed of affine (preserving parallel relationships) transformations. Figure 12 shows a schematic of the correspondence between the austenite and martensite unit cells in steel.<sup>23</sup> Austenite has a face-centered cubic structure, whereas martensite has a body-centered cubic structure. As Figure 12a and 12b show, the  $[1\bar{1}0]$  direction and the  $[110]$  direction of the austenite lattice transform to the  $[100]$  direction and the  $[010]$  direction of the martensite lattice, respectively. The  $[001]$  direction of the austenite lattice transforms to the  $[001]$  direction of the martensite lattice. However, in the transformed body-centered tetragonal (BCT) unit cell (as Figure

12b shows) the unit cell length  $b_1$  equals  $b_2$  but is smaller than  $b_3$ , which is still not the martensite structure. In order to get the body-centered cubic structure of martensite, there must be a shape change from the body-centered tetragonal austenite to the body-centered cubic martensite as Figure 12d shows.

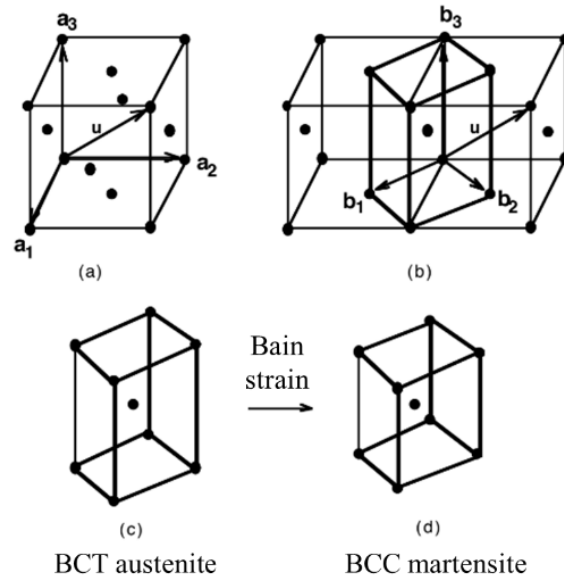


**Figure 12.** (a) Conventional FCC unit cell; (b) Relation between FCC and BCT cells of austenite; (c) BCT cell of austenite; (d) Bain strain deforming the BCT austenite lattice into a BCC martensite lattice. Reproduced with the permission from ref. 18 (Copyright 2001 Institute of Materials, Minerals and Mining).

There are three different morphologies of martensite microstructure – plate-like, needle-like, and lenticular. For steels, the plate or needle-like martensite microstructure usually forms in ultralow carbon steel, and the lenticular martensite microstructure usually forms in medium and high carbon steels.<sup>24</sup> Macroscopically the surface relief which shows the homogeneous shear taking place can be observed on the well-polished sample surface after the martensitic

transformation. Figure 13 shows the optical micrograph of the surface relief on a well-polished zirconia sample surface after martensitic transformation.<sup>25</sup>

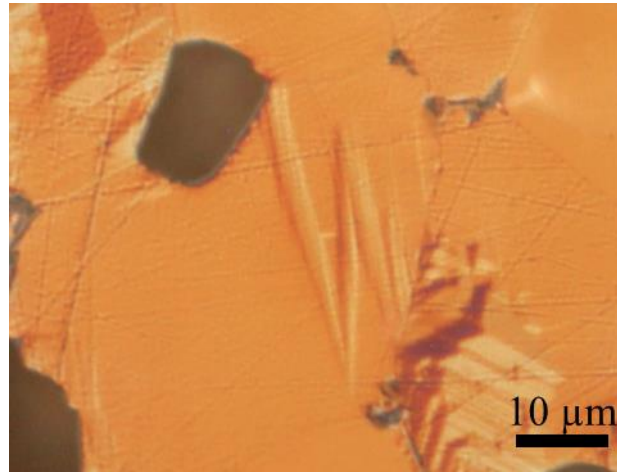


**Figure 13.** Optical micrograph of the surface relief after martensitic transformation on a well-polished zirconia sample surface. Reproduced with permission from ref. 19 (Copyright 2010 The Japan Institute of Metals and Materials).

For AISI 5160 steel, one of the most important heat treatment processes is quenching which can significantly harden the material and improve the strength. There is almost no time for diffusion to happen during the quenching process and a martensitic microstructure is formed in the steel. Therefore, there is no chemical composition difference between the parent austenite microstructure and the martensite microstructure.

Martensite, together with the other thermal process products, such as ferrite and bainite, can alter the mechanical properties for steels. Distinguishing martensite, bainite and ferrite, however, is still a challenging problem. The conventional methods used to distinguish or quantify different microstructural components are color etching and ASTM manual point count<sup>26</sup>. The color etching is based on optical microscopy whose spatial resolution is low compared with electron microscopy. This results in challenges during quantification of fine microstructures. The ASTM

manual point count method requires substantial manual work. Both the color etching and ASTM manual point count methods rely on etching, which can be inconsistent and sensitive to small differences in composition and environmental conditions. Alternatively, the EBSD-based technology can provide the required spatial resolution, is an automatic data collection processing, and can avoid the deleterious influences of etching. EBSD is thus very suitable to be used to distinguish and quantify different microstructural components for steel when compared with the color etching and ASTM manual point count methods.

For zirconia, transformation toughening is a technique that manipulates the shape and volume distortion of the martensitic transformation as a toughening mechanism. To engineer a zirconia for transformation toughening, it is important to fully understand the martensitic transformation. The microstructure and crystallographic features such as orientation relationships, habit planes, and martensite morphology from the tetragonal to monoclinic phase transformation for zirconia have been studied in abundance experimentally with techniques such as TEM, SAED and AFM.<sup>25,27-30</sup> The reported experimental results matched the PTMT very well. The advantages and disadvantages of TEM and SAED are that they can show the precise measurement of the angular difference between planes, habit plane and the local microstructure, but they cannot observe large scale features. The advantage of AFM is that it provides direct observation of the topography of the martensite plates at a large scale, but it cannot yield the orientation relationship information of the martensite plates to the parent phase. While such measurements of polycrystalline ceramics are useful for local and broad sample data, EBSD is a much more appropriate technique for the analysis of phase distribution, grain size, and orientation relationships between product and parent phases.

## **II. ON QUANTITATIVELY IDENTIFYING DIFFERENT CONSTITUENTS IN MULTICOMPONENT STEEL MICROSTRUCTURES BY EBSD**

### **A. Introduction**

Despite over a hundred years of microscopic study, the microstructure of steels remains one of the greatest challenges in the quantitative characterization of materials. High variability between various techniques is often observed for even the most seemingly simple characterization tasks, such as the measurement of volume fractions of microstructural constituents.<sup>31,32</sup> This is a critical problem, because mechanical behavior of different steel products is highly dependent on the volume fraction, size, and spatial distribution of key features in the microstructure and their constituent phases.<sup>33</sup> Accurate quantitative characterization of these parameters is important for continued development of modern ‘multi-phase’ steels, such as transformation induced plasticity (TRIP) steels and dual phase steels.

Several microstructural constituents (such as austenite, ferrite, martensite, or bainite) simultaneously co-exist in the class of steels to which TRIP steels, the so-called “dual phase” (DP), and “complex phase” (CP) steels belong. “Phase” is commonly used to refer to a primary microstructural constituent in steel, even if the constituent does not meet the generally accepted thermodynamic definition of a phase. Some of these constituents, such as pearlite, martensite and bainite, are loosely-defined mixtures of multiple phases that are identified by their distinct arrangement within the microstructure.<sup>34</sup> This high degree of complexity poses a significant challenge in terms of imaging and quantification of the microstructure.

Surface preparation is critical to the technique used to identify different microstructure of steels. An appropriate etchant can increase the contrast between phases and/or microstructural constituents,<sup>35,36</sup> but some factors such as the choice of different etchants or the etching time have a significant influence on the resulting appearance of the microstructure. For example, in optical metallography, the Klemm etchant results in regions with a higher carbon content having a white appearance (indicating austenite or carbides), while ferrite can appear in a continuum from blue to brown, and dark brown regions are identified as bainite or martensite; in contrast, the Le Pera technique results in martensite appearing in a range from white to brown, retained austenite appearing white, ferrite appearing blue, and bainite appearing brown.<sup>36,37</sup> Regardless, the reproducibility of color etching methods is not especially high, as the quality of etch is highly variable between samples and separation of the constituents which can appear in overlapping color ranges, requires interpretation by an experienced user. Furthermore, color etching methods are only applicable in optical microscopy, which has insufficient spatial resolution to identify low volume fraction and/or small particle constituents that are often observed in DP, CP, and TRIP steels, and etching methods become increasingly difficult for finer-grained samples.

When optical metallography cannot resolve the individual constituents of the microstructure, the constituents can sometimes be individually identified by scanning electron microscope (SEM) -based methods; however, the gray contrast levels of the constituents often overlap in the SEM images, complicating quantitative characterization. Identification of bainite remains a problem by standard SEM methods because it requires the user to identify regions that contain a characteristic internal morphology (as opposed to identifying regions of a specific color in optical metallography). It is clear that although the different constituents can often be

distinguished by the proper use of etchants, reproducibility of quantification still generally remains a major challenge.

For continued development of advanced steel microstructures, there is a necessity for knowledge of both the crystallographic texture and the spatial correlation among the constituents. For this reason, there is significant interest in the advancement of electron backscatter diffraction (EBSD)-based methods, since they can provide the required spatial resolution as well as microstructural information over a much more significant size scale than transmission electron microscopy.

In the scientific literature, there are several previous studies that have proposed and utilized EBSD-based methods for characterizing multi-constituents steel microstructures, but there has been very little work in the literature directly assessing the effectiveness of the suggested techniques by way of direct comparison with conventional metallography. In the present study, a detailed analysis of the capabilities of the EBSD KAM-based methods for segmentation of the individual microstructural constituents is performed for some samples of a commercial steel - AISI 5160. Results from EBSD-based methods are directly compared to results from ASTM E562-11<sup>38</sup> and color etching to assess the quantitative capabilities of the EBSD segmentation techniques.

## **1. Identification of Different Constituents of Steels by EBSD**

Distinguishing austenite from ferrite by EBSD is straightforward due to the difference in diffraction patterns caused by the different arrangements of atoms in the crystal lattices. Distinguishing martensite, bainite, and ferrite, however, is a much more challenging problem. The *c/a* ratio of the martensite phase is too low (smaller than 1.02), and thus cannot reliably be identified as tetragonal by automated EBSD. This degree of tetragonality is below the resolution of the commercial SEM-based EBSD imaging systems.<sup>39,40</sup> Bainite is a microstructural constituent

consisting of a mixture of phases, including martensite, austenite, and dislocation-rich ferrite.<sup>34</sup> The ferrite phase is observed to dominate the diffraction in the bainitic regions, such that bainite indexes as a body-centered cubic phase with a relatively poorer quality diffraction pattern than ferrite due to the influence of a higher dislocation density and/or small carbides and other phases in the diffracting volume.<sup>39,41,42</sup>

Analysis of the image quality (IQ) of the EBSD patterns has been used by several previous researchers for identification of martensite<sup>39,40,43</sup> and/or bainite.<sup>39,41,42</sup> Although bainite is generally observed to produce higher IQ values than martensite,<sup>39,41,42</sup> to the authors' knowledge there have been only two published reports showing the successful use of IQ analysis in steels containing both martensite and bainite.<sup>11,16</sup>

One means to compare technologies is Confidence index (CI). CI can be used to determine the correctness of the indexing of the orientation.<sup>44</sup> The CI value, in previous work, associated with martensitic regions<sup>42,45</sup> and bainitic regions<sup>46</sup>, and bainitic regions have been determined in both grain reference orientation deviation<sup>47</sup> and by kernel average misorientation<sup>48</sup>. To date, an optimal method for segmenting the various microstructural constituents that determine the mechanical behavior in multi-phase steels has not been determined.

## **B. Experimental Procedure for AISI 5160**

### **1. Isothermal Heat Treatment**

Two series of isothermal heat treatments were performed, one for verifying the EBSD-based methods for volume fraction and one for comparison of the volume fraction results between different measurement methods. To get different microstructures, samples of AISI 5160 steel (Fe: 97.085-97.84wt%, Mn: 0.750-1.0%, Cr: 0.7-0.9%, C: 0.56-0.64%, P: < 0.035%, Si: 0.15-0.3%, S:

< 0.04%) with dimensions of 1" x ½" x ¼" were austenized at 850°C for either 0.25 or 2 hours in air in a Thermolyne tube furnace, then transferred quickly to a molten potassium nitrate salt bath at 300°C, 400°C or 450°C for times ranging from 10 s to 40 minutes, then water quenched to lock in the microstructure. Figure 14 shows the schematic of the thermal processing steps. The detailed times and temperatures are given in Table I, where series *a* in the sample number indicates a 15 minute austenization time, and series *b* indicates a 2 hour austenization time. Samples with a 2-hour austenization time were used for comparison between color etching and ASTM E562<sup>38</sup>, because the larger prior austenite grain size makes it easier to reveal the features for optical microscopy. Both the time and temperature of the isothermal treatments in the test matrix were determined using the AISI 5160 TTT diagram.<sup>49</sup>

**Table I.** Salt Bath Time and Temperature, as well as the Corresponding Vickers Hardness and Identified Microstructure Constituents

<b>Sample number</b>	<b>Austenitizing time</b>	<b>Soaking temperature (°C)</b>	<b>Soaking time</b>	<b>Mean hardness (HV)</b>	<b>Identified constituents</b>
1a	15min	300	600s	490	B + M + F
2a	15min	300	1200s	453	B + F
3a	15min	300	1800s	512	B + F
4a	15min	300	2400s	434	B + F
5a	15min	400	20s	695	M + F + B
*5b	120min	400	20s	543	M + F + B
6a	15min	400	32s	766	M + F + B
7a	15min	400	51s	660	M + F + B
8a	15min	400	80s	156	F + P
*8b	120min	400	80s	234	P + F
9a	15min	400	126s	312	P + F
10a	15min	400	200s	309	P + F
*10b	120min	400	200s	264	P + F
11a	15min	450	10s	358	P + M + F
12a	15min	450	60s	330	P + F
13a	15min	450	100s	320	P + F
14a	15min	450	500s	318	P + F
15a	15min	450	1000s	320	P + F

\* used for comparison of the volume fraction results between color-etching and manual point count per ASTM E562-11 methods.

B: bainite, M: martensite, F: ferrite, P: pearlite

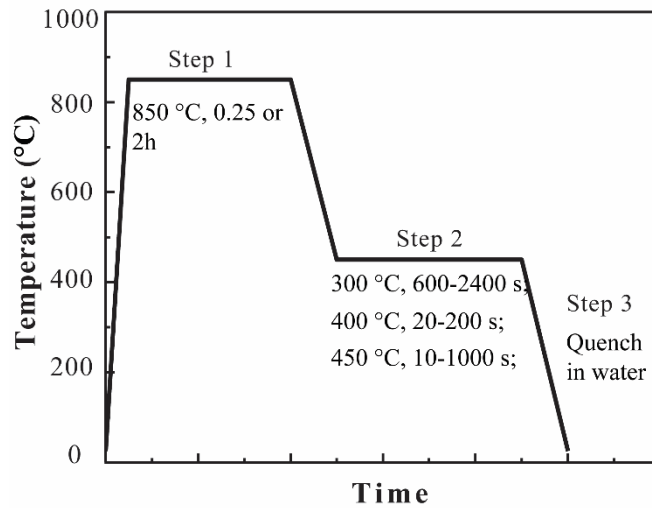


**Figure 14.** Schematic of the thermal processing steps for AISI 5160. Step 1: austenize, Step 2: soak, #tep 3: quench.

## 2. Sample Preparation and Microhardness

Samples were polished using standard metallographic techniques down to 1  $\mu\text{m}$  grit SiC, and then given a final polishing step to EBSD surface quality in a vibratory polisher with 0.05  $\mu\text{m}$  colloidal silica. After polishing, the series *b* samples were prepared by pre-etching with 4% picral (4 g dry picric acid in 100 ml ethanol). After pre-etching, the samples were color etched with the 10% aqueous solution of sodium metabisulfite (10 g  $\text{Na}_2\text{S}_2\text{O}_5$  in 100 ml distilled water). For the samples of series *a*, the surfaces were etched by 4% Nital. The microhardness of the samples was tested with a Shimadzu HMV-2000 (Shimadzu Inc., Kyoto, Japan) micro hardness tester according to ASTM E0384 using a load of 200 g, with five microhardness tests performed on each sample.<sup>50</sup>

## 3. Electron Microscopy and EBSD Analysis

Electron imaging and EBSD were performed on the samples using a JEOL 7800 scanning electron microscope (JEOL USA Inc., Peabody, MA USA). The EBSD data were collected by

TSL OIM Data Collection 7 (EDAX, Inc., Mahwah, NJ USA). The step size used for each EBSD scan was  $0.1\mu\text{m}$ . Kernel average misorientation (KAM) maps were calculated using the first through tenth nearest neighbors with  $5^\circ$  as the maximum misorientation using TSL OIM Analysis 7 (EDAX, Inc., Mahwah, NJ USA), investigating both perimeter only and all points in the kernel options. Then, Matlab (R2012a, Mathworks, Inc., Natick, MA USA) was used to make the frequency distribution plot of the KAM values for each KAM map and to calculate the full-width-at-half-maximum (FWHM) value for the frequency distributions. Finally, the FWHM was plotted against hardness for each set of samples and set of KAM map parameters. A schematic of this data processing and analysis procedure is given in Figure 15.

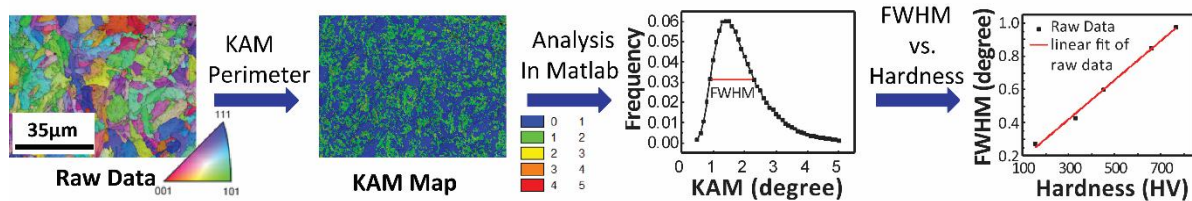


**Figure 15.** The schematic illustration of the KAM method.

For further detailed investigation of the applicability of the KAM method for the calculation of volume fractions, the blue fraction which represents the range of KAM value from  $0-1^\circ$  in the KAM maps at 1-10 Nearest Neighbor (NN) of Sample 5b and 7a were separately plotted versus the NN number. The first derivative at each point of the plot was also plotted with the NN number.

#### 4. Optical Microscopy and Color Segmentation

Optical micrographs of the color etched samples were taken at several magnifications using SPOT® Basic 4.7 imaging software (SPOT Imaging, Sterling Heights, Michigan, USA) on a

Reichert-Jung Polyvar MET optical microscope (Reichert Inc., Buffalo, NY). The contrast between the colored microstructures was insufficient for analysis in the as-taken images, so GNU Image Manipulation Program 2.8.10 (GIMP)<sup>51</sup> was used to enhance the micrographs and provide better definition to the microstructure boundaries. Regions of pearlite or martensite were then segmented from the rest of the image using the color select tool in GIMP with different color values for each region. A threshold was applied to these segmented images to provide a black and white image (black being pearlite or martensite and white being other constituents). The black pixel fractions of the binary images were then calculated by Matlab as the volume fractions of pearlite or martensite.

## **5. Calculation of Volume Fractions According to ASTM E562**

For comparison with the volume fraction result of color etching, a systematic manual point count was used to calculate the volume fractions of the Samples (#5b, 8b and 10b in Table I) according to ASTM E562-11.<sup>38</sup> In each case, the apparent volume fraction of the microstructure constituents is from color enhanced optical micrographs, and a 16-point test grid and 16 fields were used. To verify the quantification result of the KAM method, the ASTM manual point counting method was applied on the Image Quality (IQ) maps of Sample 5b and 7a. For Sample 5b, a 25-point test grid and 12 fields were used on the IQ map; For Sample 7a, a 49-point test grid and 12 fields were used on the IQ map. Figure 16a shows the IQ map of Sample 5b, and Figure 16b shows the IQ map of Sample 7a.

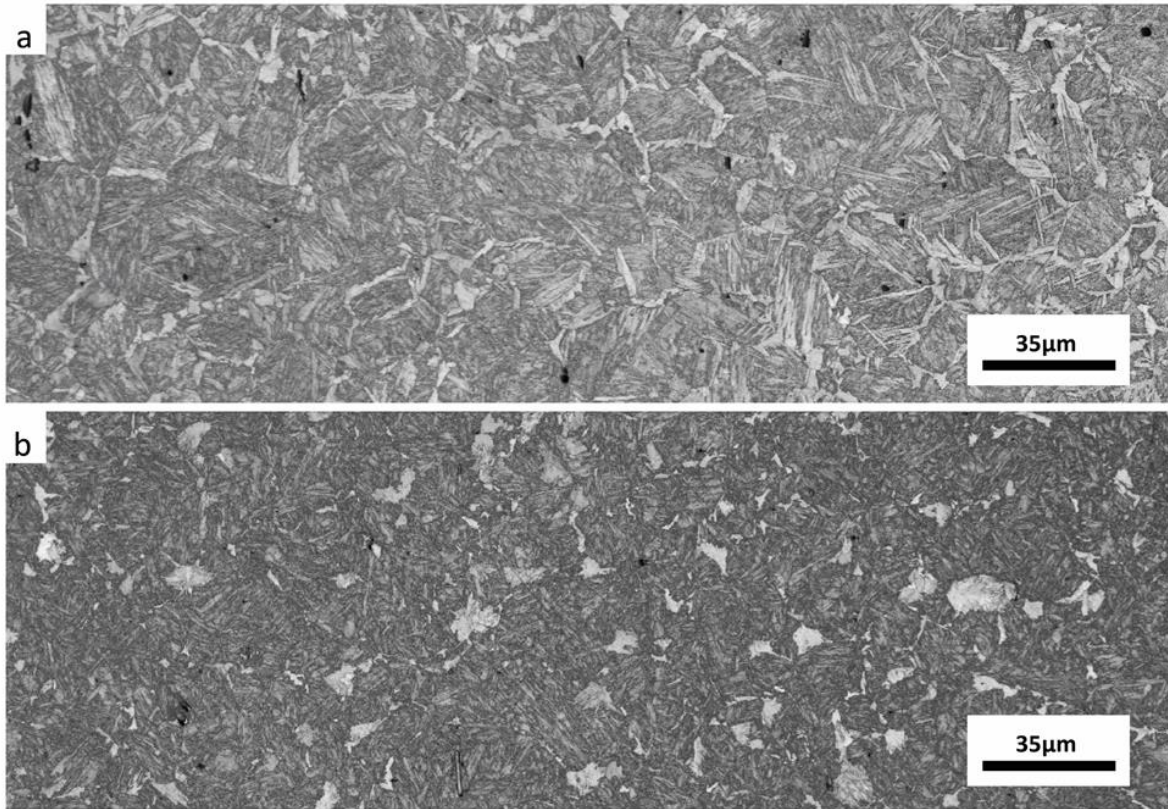


**Figure 16.** IQ maps of (a) Sample 5b and (b) Sample 7a.

## C. Results and Discussion for AISI 5160

### 1. Results

The possible constituents and Vickers hardness for sample in series *a* and *b* are given in the rightmost column of Table I. The possible constituents are identified according to secondary electron (SE) images of the etched samples and the KAM maps. All samples contain proeutectoid ferrite, even though for some samples the isothermal transformation is complete. That is because the AISI 5160 steel contains 0.56-0.64 wt% carbon, and during the cooling process, it will first precipitate proeutectoid ferrite. Then at the isothermal holding time, the proeutectoid ferrite will be gradually consumed, but it has not been consumed completely in many samples. Proeutectoid

ferrite, especially in the long-soak-time samples such as Sample 4a, 10a and 15a, can be found in the SE images or KAM maps of some isolated regions and in other regions it does not appear according to the SE images or KAM maps, indicating that the distribution of the proeutectoid ferrite is not uniform.

Figure 17 shows the results from the color optical metallography. The color-enhanced images are shown in the left column for Samples 5b, 8b, 10b while the color-based segmentations are shown in the right column. The dark constituent is martensite in Sample 5b (top row) while the bright part is ferrite and bainite. Although some features of the martensitic constituent become bright after segmentation (cf. Figure 17b), the two constituents in Figure 17b can be easily distinguished in a systematic manual point count because the points which belong to the other constituent can be deliberately ignored. Nevertheless, in the segmentation of the color images automated image processing only calculates the black and white part of the images as the volume fractions of pearlite or martensite and ferrite, so the results contain significant deviations from manual results (as shown in Table II), although the automated image processing significantly reduces the amount of manual labor required. Sample 8b (middle row) has the same problem when calculating the volume fraction by color segmentation method. For this sample, the dark constituent is pearlite and the bright part is ferrite. In the case of Sample 10b (bottom row), both the ferrite phase of the pearlite constituent and the proeutectoid ferrite appear bright after segmentation (Figure 17f). Thus, it is very difficult to separate these two ferrite constituents by color image segmentation. The results given in Table II show that the ferrite volume fraction determined by color segmentation is much larger than the results from ASTM E562-11 method.<sup>38</sup> For all three samples, ferrite volume fractions by color segmentation method were systematically higher than the ones calculated by ASTM E562-11 (shown in Table II).

**Table II.** Comparison of Volume Fraction Results by Color Etching and ASTM

<b>Sample number</b>	<b>Possible constituents</b>	<b>Calculated % by color etching</b>	<b>Calculated % by ASTM (based on OM) with 95% CI</b>
5b	M + B + F	M+B = 35.05-38.32 F = 64.95-61.68	M+B = 60.55±5.26 F = 39.45∓5.26
8b	P + F	P = 32.51-36.27 F = 67.49-63.73	P = 53.32±6.27 F = 46.68∓6.27
10b	P + F	P = 20.1-25.61 F = 79.9-74.39	P = 83.4±4.7 F = 16.4∓4.7

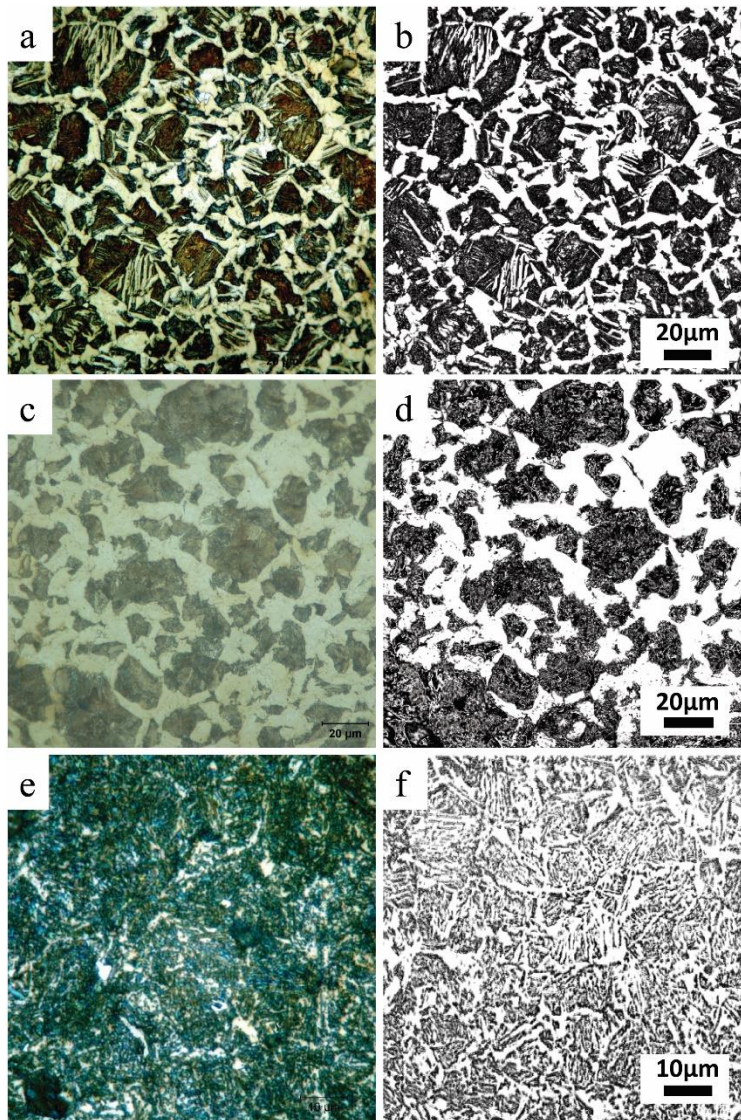
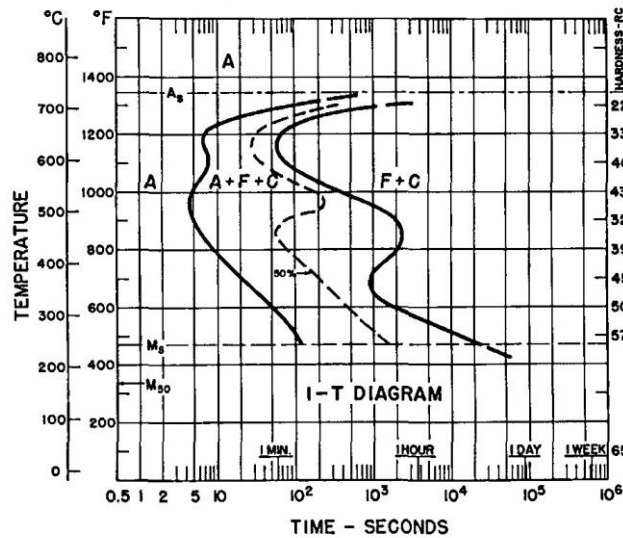


**Figure 17.** Color enhanced optical images (left) and the corresponding images after segmentation by GIMP (right) (a) Sample 5b in Table III; (b) Sample 8b in Table III; (c) Sample 10b in Table III.

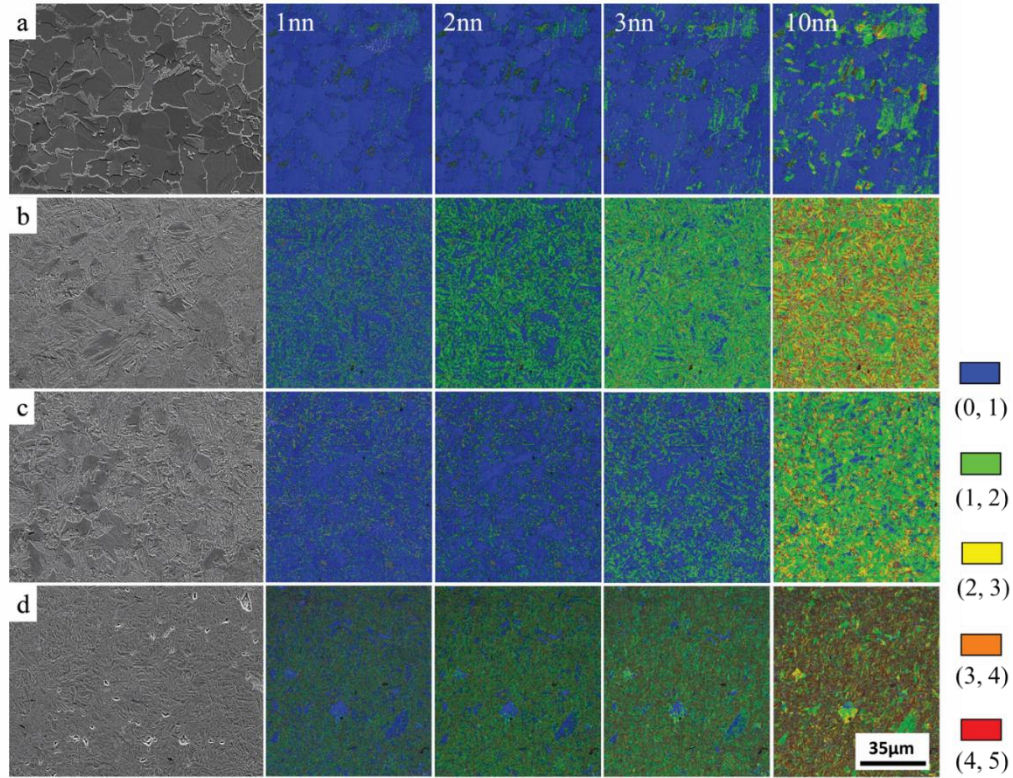
For the samples austenized for 15 minutes at 850°C (series *a*), then isothermally soaked at 300°C with the holding time ranging from 10 minutes to 40 minutes (Sample 1a-4a), all of the samples became solely bainite with ferrite except for the 10-minute sample (1a) which also contained martensite, indicating residual untransformed austenite existed at this short soak time at 300°C. Figure 18 shows the TTT diagram of the AISI 5160 steel.<sup>49</sup> Since no martensite was

observed in the samples with soak times greater than 10 minutes, all other specimens from this temperature series show coarsening of the transformed microstructure. For 400°C-soaks, when the holding time was less than 51s (Samples 5a and 6a), the final microstructure of the samples was martensite with a small amount of ferrite and bainite. For Sample 8a held for 80s, the microstructure became a combination of mostly ferrite with less than half of the volume consisting of pearlite. The last two samples held at 400°C (126s and 200s, 9a and 10a respectively) became almost 100% pearlite. For the samples held at 450°C, all became pearlite with very small amount of ferrite with the exception of the 10-second sample (11a), which contains some martensite.

**Type: 5160**  
**Composition: Fe - 0.61% C - 0.94% Mn - 0.88% Cr Grain size: 7**  
**Austenitized at 843°C (1550°F)**



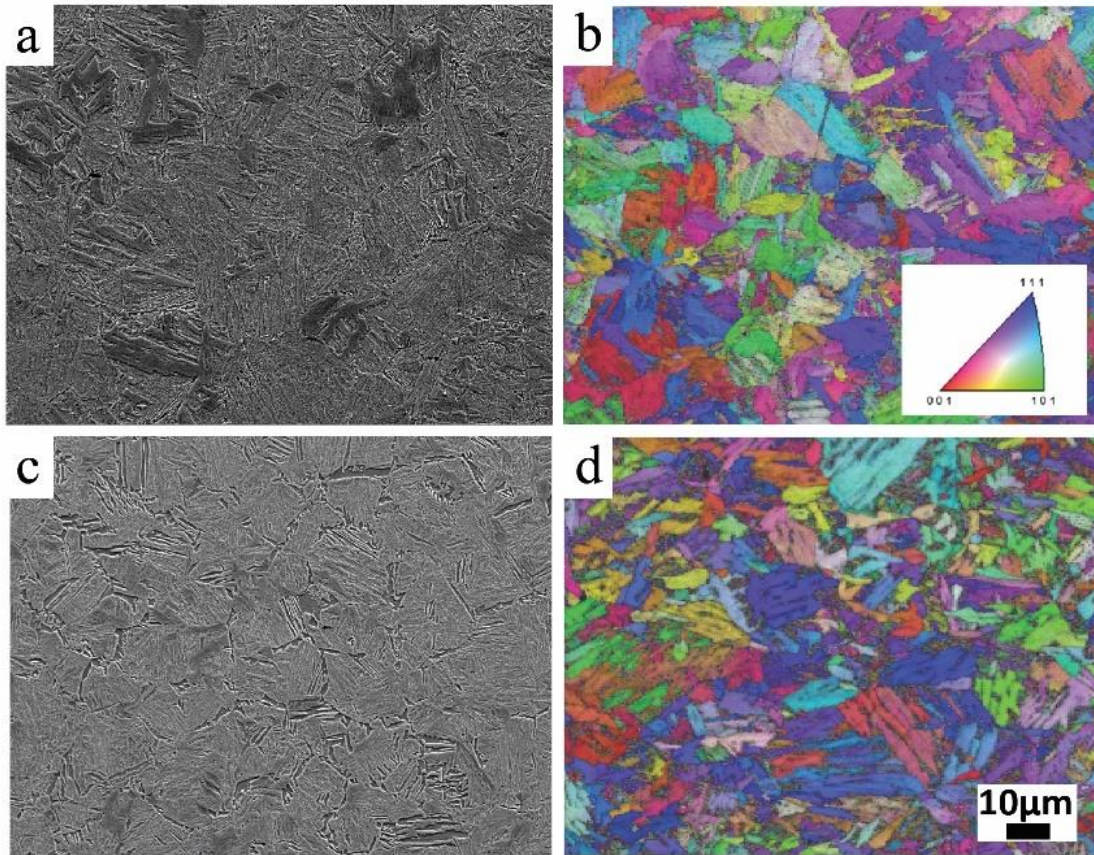
**Figure 18.** Time-temperature-transformation (TTT) diagram of the AISI 5160 steel. Reproduced with the permission from ref. 44 (Copyright 1991 ASM International).



**Figure 19.** The SE image and IQ+KAM maps at 1NN, 2NN, 3NN and 10NN of (a) Sample 8a; (b) Sample 2a; (c) Sample 12a; (d) Sample 6a in Table I (KAM values are binned in 1 degree increments as shown in the color scale at right).

KAM mapping was investigated for its efficacy in identifying different phases or constituents in the samples of series *a*. Figure 19 shows the change of the Image Quality (IQ, gray scale) + KAM (color scale) maps with the increase of the nearest neighbor number (NN#) for different phases or constituents under the premise that other influencing factors are fixed. The hexagonal grid type when collecting EBSD data was used in all cases. Figure 19a corresponds to the SE image and KAM maps created with 1<sup>st</sup>, 2<sup>nd</sup>, 3<sup>rd</sup> and 10<sup>th</sup> NN# of Sample 8a (which contains ferrite and pearlite Table I). It is observed that ferrite has an almost stable KAM value with the growth in NN# (typically remaining in the lowest KAM value range, 0-1°) while for the pearlite part, the KAM value increases with increasing number of nearest neighbors (#NN) included in the

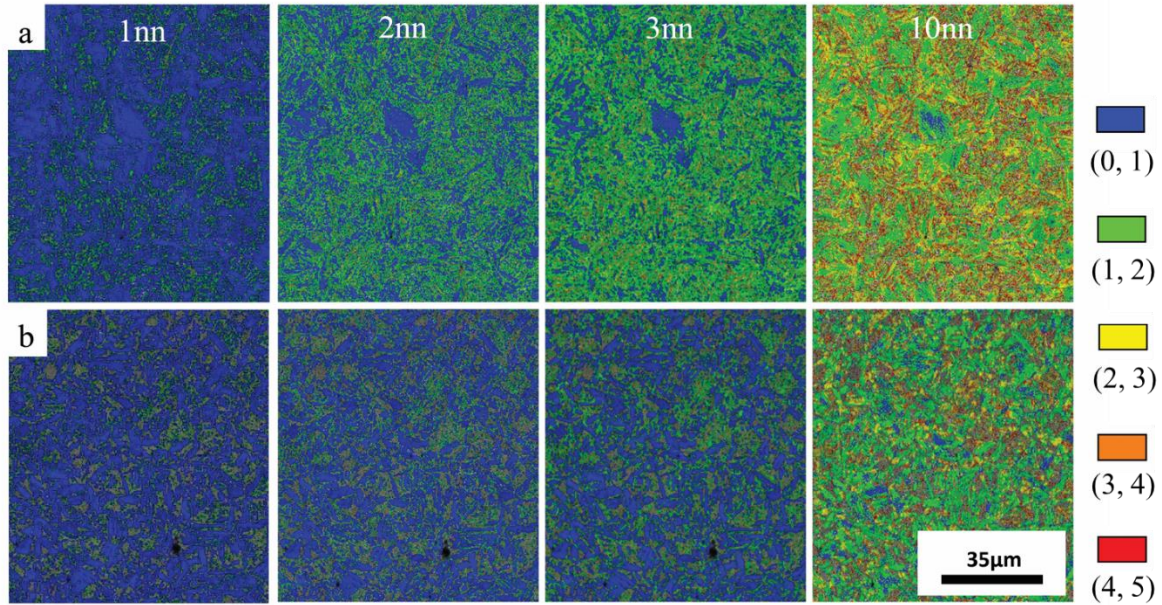
kernel. Figure 19b corresponds to Sample 2a, which consists almost entirely of bainite, while Figure 19c corresponds to Sample 12a which consists almost entirely of pearlite. When comparing Figures 19b and 19c, it is found that bainite and pearlite at small NN# exhibited no conspicuous characteristics that would enable them to be distinguished from ferrite. As NN# increases, however, the values in the KAM map gradually are observed to increase gradually (which can be observed by the change in color). Bainite and pearlite can thus be distinguished by comparison of the IQ+KAM maps of them at large NN#, such as 10th NN# -- the interface between the bainitic laths is more obvious in the KAM maps than the interface between pearlite laths at large NN#. Furthermore, at the same NN# and the other conditions are the same, such as the strain from external is the same and the coarsening of the microstructure features is the same, the color of the KAM maps which belong to bainite should always reveal a larger KAM value than the pearlite KAM maps. Figure 19d is from Sample 6a which contains martensite and ferrite. For this sample, the KAM value of ferrite in the KAM maps will change with the increase of the NN#, which means the ferrite part contains more strain in the martensite+ferrite sample than in the pearlite/bainite+ferrite samples. From Figure 19d, it is also observed that martensite, even at small NN#, will have already shown large KAM values in the map. In brief, with the increase of the NN#, the KAM value increases for every constituent; however, the rate of increase varies for the microstructural constituents. Ferrite exhibits the slowest increase in KAM values with NN#, while martensite exhibits the fastest increase.



**Figure 20.** (a) SE images of Sample 1a; (b) IPF maps of Sample 1a; (c) SE images of Sample 11a; (d) IPF maps of Sample 11a in Table I.

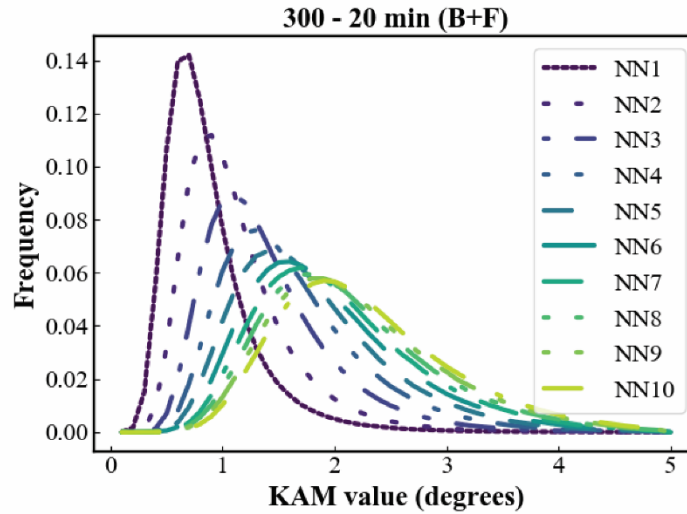
Figure 20 shows the SE images (left) and Inverse Pole figure (IPF) maps (right) for Samples 1a and 11a. Bainite, martensite and ferrite are observed in Sample 1a (Figure 20a and 20b). Pearlite, martensite, and ferrite are observed in Sample 11a (Figure 20c and 20d). KAM maps corresponding to the specimens in Figure 20, Samples 1a and 11a, are shown in Figure 21a and 21b, respectively. It is difficult to identify the martensitic microstructure regions by morphology in the SE image or IPF map alone for each sample; the KAM map is helpful in locating the martensitic regions, which have systematically higher KAM values. Comparison of Figures 12 and 13 demonstrates how easy it can be to make an incorrect estimate that the samples only contain

bainite/pearlite with very little ferrite. Even in the 1NN KAM maps in Figure 21, some regions of large KAM values are seen, indicating the spatial locations of martensitic regions.



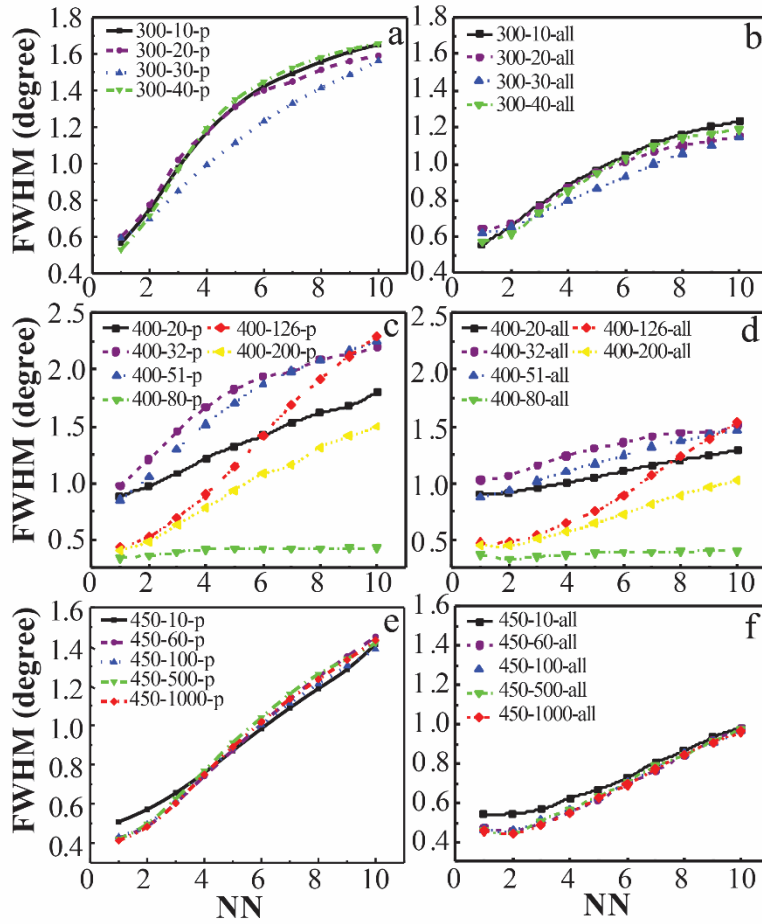
**Figure 21.** KAM maps at 1NN, 2NN, 3NN and 10NN of (a) Sample 1a; and (b) Sample 11a in Table III (KAM values are binned in 1 degree increments as shown in the color scale at right).

Figure 22 shows the frequency distribution curves of the KAM value at different NN# for the related KAM map of Sample 2a. The abscissa of the curve is the KAM value ranging from 0-5°, and the ordinate is the frequency of the corresponding KAM value. In Figure 22, there are 50 KAM values at the interval of 0.1° ranging from 0-5° to be chosen together with their frequencies to make each curve. Figure 22 shows that, with the increase of the NN#, the frequency distribution curves widen and the peak frequency for each KAM value declines. The same characteristics of the frequency distribution curves were observed for every sample in Table I.



**Figure 22.** KAM frequency distribution plots of Sample 2a in Table I.

Figure 23 reveals the capability of FWHM for reducing the variation in KAM distribution (cf. Figure 22) into a single parameter by plotting FWHM against NN#. FWHM is influenced by the lowest and the largest KAM value of the sample, the peak frequency, and peak position. A comparison of Figure 22 and Figure 23 shows that the trend of the frequency vs. KAM curves with increased NN# is consistent with the trend of the FWHM vs. NN# plots; i.e., the FWHM value can appropriately capture differences between specimens and serve as a proxy for the distribution of KAM values in a KAM map. Figure 23 also shows the same trend that perimeter (left column) offers and all points in the kernel offer (right column) - with the increase of NN#, the FWHM value increases. Compared with all points, perimeter gave rise to better FWHM sensitivity to NN# and shorter calculation time compared with the calculation of KAM with all points in the kernel. Thus, perimeter is used in the subsequent analysis when creating KAM maps.



**Figure 23.** FWHM of KAM distribution vs NN# plots for (a) 300°C group, perimeter offers; (b) 300°C group, all points in the kernel offer; (c) 400°C group, perimeter offers; (d) 400°C group, all points in the kernel offer; (e) 450°C group, perimeter offers; (f) 450°C group, all points in the kernel offer.

Some correlations between FWHM value and hardness were observed in the three isothermal processing groups of samples. For both 300°C (Samples 1a-4a) and 450°C (Sample 11a-15a) groups, all samples except the first one (shortest soak) in each group contain the same microstructural constituents. Only with longer isothermal holding time does the microstructure coarsen which will influence the hardness of the samples. Figure 24a shows the FWHM value vs. hardness plots at different NN# for samples processed at 450°C that contain a single constituent

pearlite and Figure 24b shows the corresponding regularity of slope, intercept, and R-squared value of the plots from Figure 24a. Figure 24c shows the FWHM value vs. hardness plots at different NN# for the three samples processed at 300°C that contain a single constituent bainite and Figure 24d shows the corresponding regularity of slope, intercept and R-squared value of the plots in Figure 24c. As shown in Figure 24b and 24d that the FWHM value stays almost stable while hardness varies for a given sample that contains the same constituents. The influences of different constituents exert a much greater influence on the FWHM value than the scale of the microstructure (i.e., coarsening).

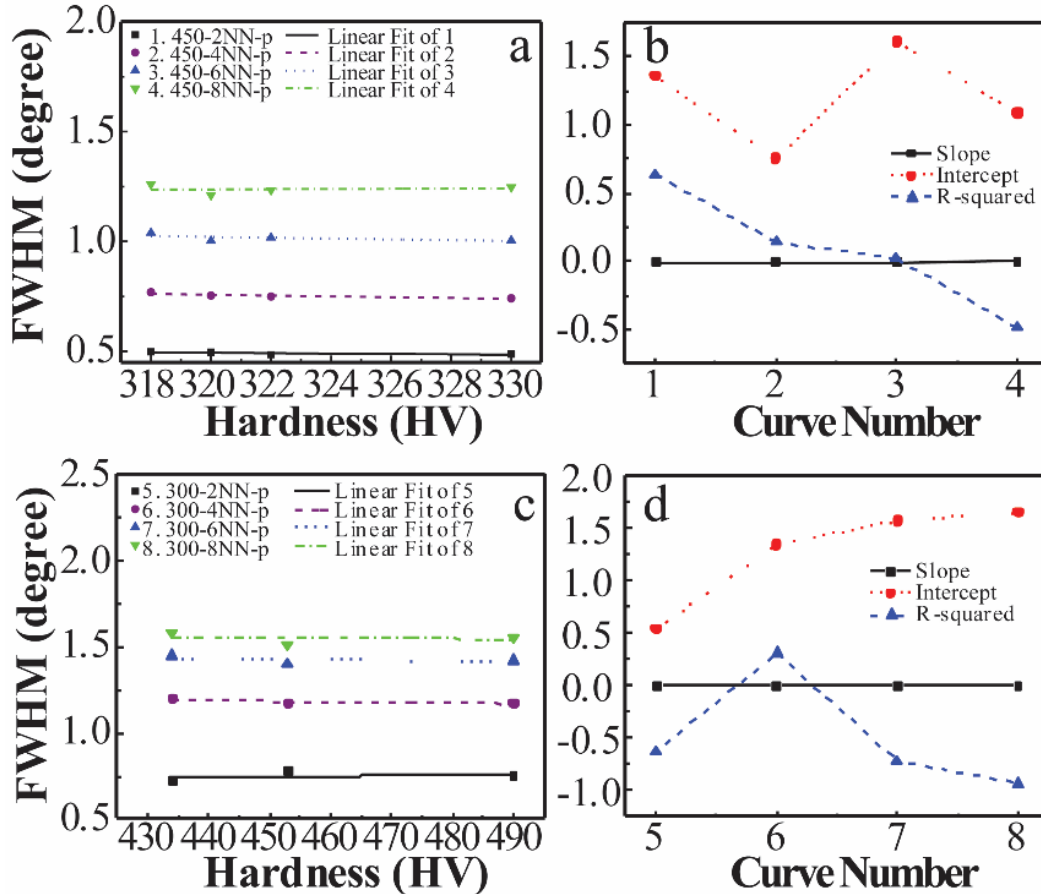


**Figure 24.** (a) FWHM vs Hardness plots for 450°C group; (b) the change of slope, intercept and R-squared value with different curve number for 450°C group; (c) FWHM vs Hardness plots for 300°C group; (d) the change of slope, intercept and R-squared value with different curve number for 300°C group.

Considering the samples in series *a* together, it is found that there is almost a linear relationship between FWHM value and hardness of different samples, as shown in Figure 25a. The linearity between the FWHM and HV is shown for KAM calculations performed with 1NN, 2NN, 4NN and 9NN. Figure 25b shows the slope, intercept and R-squared values for these plots. The slope increases with the increase of the NN#. The R-squared value decreases indicating that the deviation of the raw data from the linear fit increases as the kernel size increases.

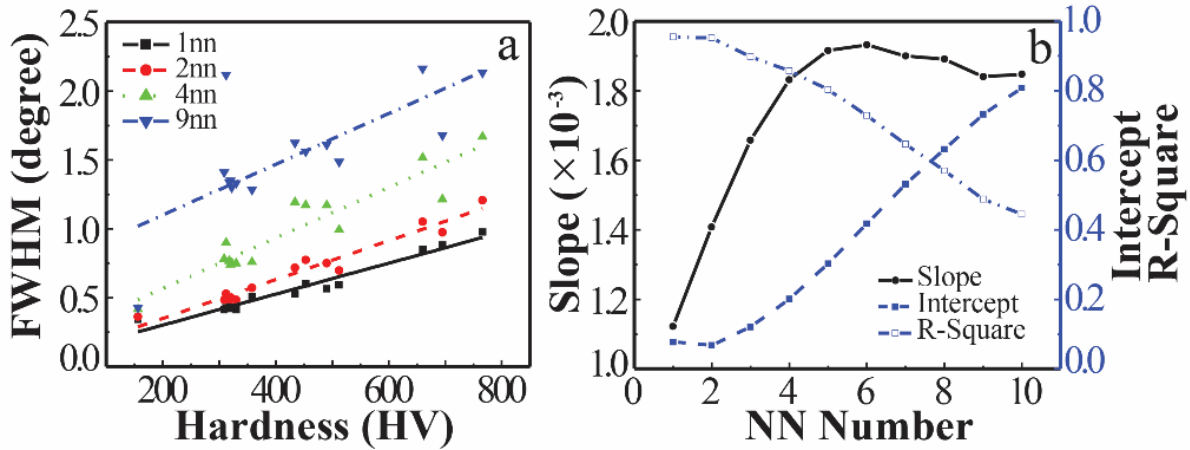


**Figure 25.** (a) Linear relationship between FWHM and Hardness with the influence of NN#; (b) the change of slope, intercept and R-squared value with different NN# for all samples in series *a*.

The quantification of different constituents is based on the obvious change of the reducing rate of the fraction of KAM values under  $1^\circ$  in the KAM maps (let  $\lambda$  = the fraction of KAM values under  $1^\circ$ ). Figure 26 shows some typical 1<sup>st</sup> derivative  $d\lambda/d(NN\#)$  vs. NN# plots for different constituents which include Sample 2a (almost pure bainite), Sample 6a (almost pure martensite), Sample 8a (contains roughly 80% ferrite and 20% pearlite), and Sample 10a (almost pure pearlite). The common features of these 1<sup>st</sup> derivative plots are that (1) the value of the 1<sup>st</sup> derivative is always negative, indicating the decreasing of the fraction of KAM values under  $1^\circ$ ; (2) the shape

of the curve indicates that the reducing rate of the fraction of KAM values under  $1^\circ$  is fast at smaller NN# and then slows down with the increase of the NN#. From comparison among these 1<sup>st</sup> derivative plots of different constituents, it is found that with increasing NN#, ferrite has the slowest reducing rate of the fraction of KAM values under  $1^\circ$ , the second slowest reducing rate belongs to pearlite, bainite has a larger reducing rate than pearlite, and martensite has the fastest reducing rate. For a multiphase sample, the reducing rate is the sum of the reducing rate of each constituent, and the shape of the 1<sup>st</sup> derivative plot is similar to the plot of a single constituent. Nonetheless, the direct addition of the known reducing rate of the constituents from one sample cannot be used to predict the reducing rate for another multi-constituent sample. That is because a constituent may contain different amounts of strain in different samples. Take Sample 6a and 8a as the example for comparison. As shown in Figure 19a and 19d, the ferrite portion can still be blue (representing the KAM value is in the range of  $0-1^\circ$ ) in the KAM maps at 10NN for Sample 8a (a ferrite+pearlite sample), while the ferrite begins to turn color at 3NN for Sample 6a (a martensite+ferrite sample).

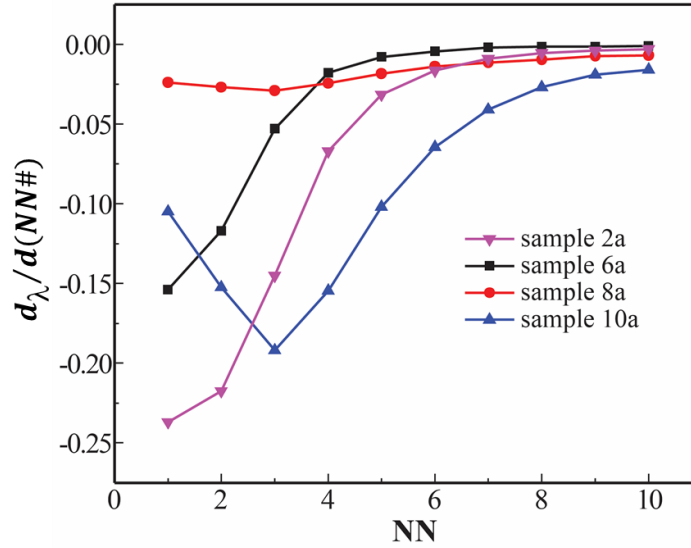


**Figure 26.** The typical  $d\lambda/d(NN\#)$  vs. NN# plots for Sample 2a (bainitic microstructure), 6a (martensitic microstructure), 8a (roughly 80% ferrite and 20% perlite) and 10a (perlite microstructure) in Table I.

Figure 27 shows the fraction of KAM values less than  $1^\circ$  in the KAM maps ( $\lambda$ ) vs. NN# plot together with the 1<sup>st</sup> derivative  $d\lambda/d(NN\#)$  vs. NN# for Sample 5b and 7a which both contain martensite, bainite and ferrite. It can be seen in the Figure that the volume fraction of KAM values under  $1^\circ$  decreases with increasing NN# for both samples. The 1<sup>st</sup> derivative curve is used to show the reducing rate of the fraction of KAM values under  $1^\circ$ . Both the 1<sup>st</sup> derivative curves show that the rate at which the fraction of KAM values less than  $1^\circ$  is at a maximum for small NN# and gradually decreases with increasing NN#. As it was shown in Figure 22, the common features of the KAM frequency distribution curve for every constituent are that (1) the shape of the curves are similar; (2) at 1NN, every curve begins in the range of 0-1 degree which is blue color in the KAM map; and (3) with the increase of the NN#, the curve widens and moves towards to a larger KAM value. For the KAM map at 1NN, each constituent contains the fraction of KAM

values under  $1^\circ$ . However, with the increase of the NN#, each different constituent has a different reducing rate of the fraction of KAM values under  $1^\circ$ . For Samples 5b and 7a, since martensite and ferrite have much different reducing rate of the fraction of KAM values under  $1^\circ$ , with the increase of NN# the reducing rate of the fraction of KAM values under  $1^\circ$  for martensite will gradually decrease while ferrite will still stay in the region with KAM values under  $1^\circ$ . At certain NN#, the blue fraction of martensite will totally disappear, and the remaining fraction of KAM values under  $1^\circ$  in the KAM map are thus considered to be the volume fraction of ferrite. When the NN# continues to increase, the reducing rate of the fraction of KAM values under  $1^\circ$  will diminish. In the case of Sample 5b, the obvious reducing rate change happened between 5NN and 6NN on the 1<sup>st</sup> derivative curve, so the ferrite volume fraction is considered to be the fraction of KAM values under  $1^\circ$  in the KAM map between 5NN and 6NN. In the same way, for Sample 7a, the ferrite volume fraction is considered to be the fraction between 4NN and 5NN. Table III shows the volume fraction results by means of KAM method for the two samples and compares them with the results of the ASTM manual counting method with the 95% Confidence Interval. In the case of an inhomogeneous special distribution of the constituents, the ASTM method was directly applied on the IQ maps (Figure 16) of the samples. Samples 5b and 7a were selected for comparison due to the fact that the IQ maps of these two samples have very good contrast between martensite and ferrite+bainite, which is beneficial for the accuracy of the ASTM point count.

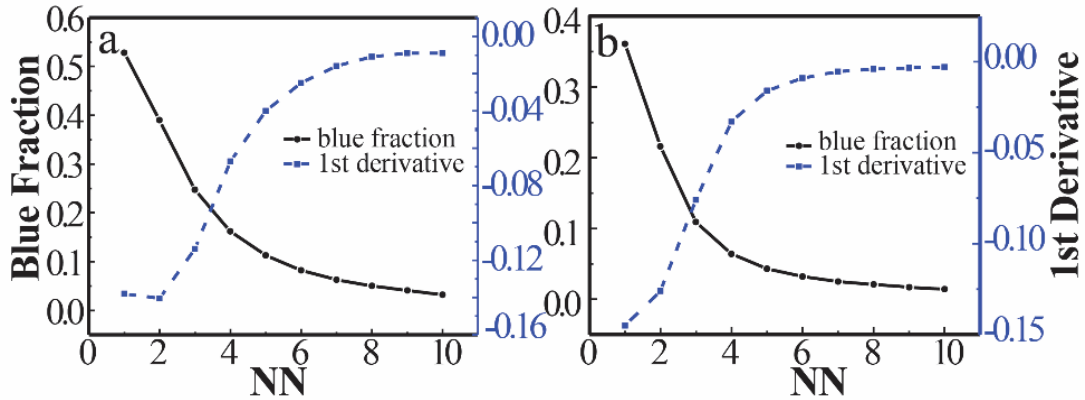


**Figure 27.** Fraction of the KAM values less than  $1^\circ$  (blue) in the KAM maps ( $\lambda$ ) vs NN# and 1<sup>st</sup> derivative  $d\lambda/d(NN\#)$  vs. NN# curves for (a) Sample 5b; and (b) Sample 7a both containing martensite and ferrite.

**Table III:** Comparison of Volume Fraction Results by KAM and ASTM

Sample number	Possible constituents	Calculated % by KAM	Calculated % by ASTM (based on IQ map) with 95% CI
5b	M + B + F	M+B = 91.8-88.7 F = 8.2-11.3	M+B = 88.67±3.13 F = 11.33±3.13
7a	M + F	M = 95.7-93.6 F = 4.3-6.4	M = 93.62±2.2 F = 6.38±2.2

## 2. Discussion

Different thermal processing yields different constituents or phases in steels which contain different amounts of plastic strain. For example, diffusion of carbon and other alloying elements in the steels during thermal processing cause distortion of the crystal lattice of iron; heat treatment conditions such as temperature, cooling rate, or annealing time may result in imperfections in the lattice of the polycrystalline samples. Lattice distortion and lattice imperfections are the forms of

plastic strain; therefore, the plastic strain in different thermal processing products can be visualized in KAM maps.

For samples of series *a*, it is found that only five samples satisfy the linear relationship between FWHM value and Vickers hardness at 1NN. They are Sample 2a (bainite + few ferrite, the 10<sup>th</sup> point in Figure 25a), 5a (martensite + few ferrite + few bainite, the 14<sup>th</sup> point in Figure 25a), 6a (martensite + few ferrite + few bainite, the 15<sup>th</sup> point in Figure 25a), 7a (martensite + few ferrite + few bainite, the 13<sup>th</sup> point in Figure 25a) and 12a (pearlite + few ferrite, the 7<sup>th</sup> point in Figure 25a). For the other samples which deviate from the linear relationship, the major reason is due to the hardness rather than the FWHM value. The hardness of a multiphase sample does not always follow a rule of mixtures type weighted summation of constituent hardness values.<sup>52</sup> From a micromechanics perspective, this makes sense since the rule of mixtures is fundamentally an averaging rule and ignores features arising from microstructural heterogeneity such as stress concentrations that might lead to local plastic deformation.<sup>52</sup> That is to say, when the hardness of the sample is not the summation of each component, the sample would be expected to deviate from the linear relationship shown in Figure 25.

There are four factors that influence the FWHM value and cause deviation from the linear relationship. The first factor is external stress. It will both change the FWHM value and the superposition property of it. The four room-temperature constituents of steel have different resistance to external stress (such as that experienced during polishing). From Figure 19a, it can be seen, at the same polishing condition, there are obvious scratches in the ferrite regions but fewer in the pearlite area. Thus, for quantification, gentler polishing methods may be better for the accuracy of the results.

The second factor is the choice of the NN# which alters the FWHM value but does not influence the superposition property of it. In the present study, 1NN corresponds to a kernel size of  $0.1\mu\text{m}$ , and 10NN equals to the kernel size of  $1\mu\text{m}$  when the step size of  $0.1\mu\text{m}$  was used for EBSD scan. In Figure 25, at small NN#, the points satisfy the linear relationship very well, while with an increase of the kernel size some points gradually deviate from linearity. This can be explained by the fact that the increase of the FWHM value is not linear with the increase of the NN#.

The third factor is the interval of the KAM distribution plots which will change both the FWHM value and its superposition property. In the present study, the interval of  $0.1^\circ$  was used to yield smooth curves for all the samples. Curves were found to fit well to the Poisson distribution. The smoothness of the curve influences the calculation of the FWHM value. The more the points that fall the curve, the more real the shape of the distribution plot may appear. Therefore, the combination of kernel size of the KAM map and the interval of the KAM distribution value should be balanced according to the specific microstructure features so that its KAM distribution plot can be smooth enough to calculate the FWHM value.

Lastly, the microstructure coarsening arising from a long soak time or other reasons also have a slight influence on the FWHM value and result in deviation from the linear relationship, but coarsening will not change the superposition property of the FWHM value.

#### **D. Conclusions**

- The KAM method can provide a rough estimate of the volume fraction of constituents in multi-constituent steels, and the results are comparable to the ASTM manual point counting results.

- KAM-based volume fraction measurement eliminates one source of variance in quantification because it does not require chemical etching, which can be spatially and compositionally inconsistent over the specimen surface.
- The ASTM manual point counting method gives the volume fraction results with a 95% Confidence Interval. However, the manual work is time-consuming, and it may be difficult to achieve sufficient contrast to distinguish the constituents. The KAM method is an automatic processing method, which can identify different constituents quantitatively by changing some parameters.
- Microstructure coarsening has less influence on the FWHM values than does the constituent.
- Scratches, strain from the polishing, or microstructure coarsening could deviate the points from the linear relationship, but if the scratches, strain from the polishing or microstructure coarsening are uniform for the sample, it will not influence the calculation of volume fractions, because the effects of the scratches, strain from the polishing or microstructure coarsening on the sample will be eliminated during the calculation of volume fraction.

### III. EBSD INVESTIGATION OF TETRAGONAL TO MONOCLINIC PHASE TRANSFORMATION IN 10 MOL% CERIA DOPED ZIRCONIA

#### A. Introduction

Bansal and Heuer showed that pure  $ZrO_2$  exhibits a martensitic transformation.<sup>53</sup> Zirconia is of interest for fundamental comparison to the martensitic transformations that occur in metals, such as steels and NiTi shape memory alloys, due to its high transformation temperature and the fact that it is a ceramic.<sup>53</sup> For pure  $ZrO_2$  at atmospheric pressure, the cubic phase is stable from 2370°C until the melting point which is 2715°C, the tetragonal phase is stable for temperatures between 1200°C and 2370°C, and the monoclinic phase is stable below 1200°C. The tetragonal to monoclinic transformation in pure  $ZrO_2$  is accompanied by a 3% volume increase. The high-temperature tetragonal and cubic phases of  $ZrO_2$  can be stabilized by doping  $Y_2O_3$ ,  $CeO_2$ , or  $MgO$  into solid solution,<sup>54</sup> which results in a pure metastable phase or a matrix of mixed cubic, tetragonal, or monoclinic phases at ambient temperature.<sup>55</sup>

The two major types of the “toughened” zirconia ceramics are partially stabilized zirconia (PSZ) and tetragonal zirconia polycrystals (TZP). For PSZ, with the addition of  $MgO$ ,  $CeO_2$ , or other selected dopants, the high-temperature metastable cubic and tetragonal phases are partially stabilized at room temperature to form a matrix of mixed cubic, tetragonal, or monoclinic phases. For TZP, by addition of proper amount of  $Y_2O_3$ ,  $CeO_2$  or other selected dopants, TZP contains almost purely tetragonal fine, equiaxed grains (0.5-3  $\mu m$  diameter) at room temperature.<sup>1</sup> These stabilized systems give rise to a useful application of the martensitic transformation<sup>55</sup>: transformation toughening utilizes the shape and volume distortion of the martensitic

transformation as a toughening mechanism. The discovery of transformation toughening in zirconia ceramics in the 1970s aroused worldwide interest in the study of martensite transformation in non-metallic materials.<sup>56</sup> Zirconia-based ceramics were found to be among the strongest and toughest monolithic oxide ceramics to date. Transformation toughening applies the strain field of the martensite transformations to reduce and inhibit cracking. The transformation produces interact with the crack-tip stresses so as to consume part of the energy and thus to prevent or blunt crack extension. Even if there is no crack in/on the sample, the transformation generates local stresses in the form of crack shielding to ensure a net increase in toughness of the materials.<sup>57</sup>

Zirconia-toughened ceramics are designed so as to retain the metastable tetragonal phase to room temperature. Additional mechanical stress, such as that experienced ahead of an advancing crack tip, can provide the energy necessary to induce transformation to the monoclinic phase with an increase in volume. To understand the strain field of the martensitic transformation, it is necessary to gain a clear idea of the transformation crystallography including the lattice correspondence and orientation relationship (OR) between the parent and product crystal. The martensitic transformation is a homogeneous deformation of the crystal structure from parent to product, which means the points which were colinear in the parent structure remain colinear after phase transformation, and so do the lines which are coplanar initially. The lattice correspondence is a 3×3 matrix which determines which lattice points, directions and planes in the parent and product crystal lattices are corresponding to each other uniquely. Such as in the case of Figure 12b, the relation between the FCC and BCT cells of austenite are that:

$$a_1 = 1b_1 + 1b_2 + 0b_3 \quad (1)$$

$$a_2 = -1b_1 + 1b_2 + 0b_3 \quad (2)$$

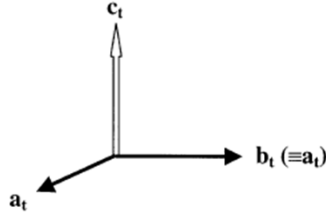
$$a_3 = 0b_1 + 0b_2 + 1b_3 \quad (3)$$

The above equations can be rewritten as:

$$(a_1 \quad a_2 \quad a_3) = (b_1 \quad b_2 \quad b_3) \begin{pmatrix} 1 & -1 & 0 \\ 1 & 1 & 0 \\ 0 & 0 & 1 \end{pmatrix} \quad (4)$$

The matrix in equation 4 is called the lattice correspondence matrix or just correspondence.

The orientation relationship relates the planes and directions of the parent and product crystal as roughly parallel.<sup>58</sup> For the tetragonal to monoclinic transformation in zirconia, there are three possible correspondences between the parent and product crystal structures, and in each correspondence there are two different orientation relationships between the parent and product phases. Kriven<sup>59</sup> denoted the three correspondences as A, B, and C. The two orientation relationships, for example in correspondence A, are denoted as A-1 and A-2 separately. Since the angle  $\beta$  between  $a_m$  and  $c_m$  of the monoclinic phase is not equal to  $90^\circ$ , the orientational relationships (OR) A-1 and A-2 differ by  $(\beta-90)^\circ$  along  $a_m$  axis. The ORs in the other two correspondences can be denoted in the same way. Figure 28 shows the schematic of the three correspondences for one case of the tetragonal to monoclinic transformation in zirconia, with the two different ORs in each correspondence.<sup>60</sup> The ORs are expressed as a set of parallelism relations including a pair of parallel planes and two pairs of parallel directions.



This tetragonal crystal can transform to monoclinic so that the  $c_t$  axis becomes:  $a_m$  (far left – correspondence A), or  $b_m$  (middle – correspondence B), or  $c_m$  (far right – correspondence C).

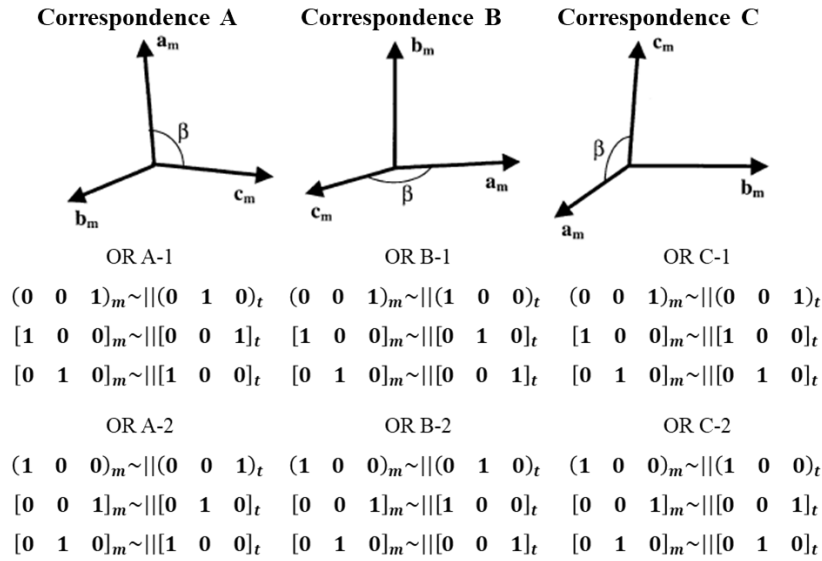


**Figure 28.** The schematic of the three correspondences for one case of the tetragonal to monoclinic transformation in zirconia, and the two different ORs in each correspondence. Reproduced with the permission from ref. 55 (Copyright 2002 Elsevier Science Ltd.).

However, for each orientation relationship, there are eight different variants. To distinguish these variants, Hayakawa introduced a more comprehensive notation.<sup>61-63</sup> According to Hayakawa's notation, such as for correspondence A, the eight different variants are denoted as  $BCA$ ,  $\bar{B}\bar{C}\bar{A}$ ,  $\bar{C}\bar{B}\bar{A}$ ,  $C\bar{B}\bar{A}$ ,  $\bar{B}\bar{C}\bar{A}$ ,  $B\bar{C}\bar{A}$ ,  $\bar{C}\bar{B}\bar{A}$  and  $CB\bar{A}$ . Table IV shows the lattice correspondence matrix for the eight variants based on the case in Figure 28. Taking lattice correspondence  $BCA$  as an example, the correspondence matrix converts the  $a$  axis of the tetragonal phase to  $b$  axis of the monoclinic phase by:

$$\begin{bmatrix} 0 & 0 & 1 \\ 1 & 0 & 0 \\ 0 & 1 & 0 \end{bmatrix} \begin{bmatrix} 1 \\ 0 \\ 0 \end{bmatrix}_t = \begin{bmatrix} 0 \\ 1 \\ 0 \end{bmatrix}_m \quad (5)$$

and converts the (1 0 0) plane of the tetragonal phase to (0 1 0) plane of the monoclinic phase by:

$$(1 \ 0 \ 0)_t \begin{bmatrix} 0 & 0 & 1 \\ 1 & 0 & 0 \\ 0 & 1 & 0 \end{bmatrix}^{-1} = (0 \ 1 \ 0)_m \quad (6)$$

**Table IV.** The Eight Variants for Correspondence A Following Hayakawa

Lattice correspondence	matrix
<i>BCA</i>	$\begin{bmatrix} 0 & 0 & 1 \\ 1 & 0 & 0 \\ 0 & 1 & 0 \end{bmatrix}$
$\overline{BCA}$	$\begin{bmatrix} 0 & 0 & 1 \\ -1 & 0 & 0 \\ 0 & -1 & 0 \end{bmatrix}$
$\overline{CBA}$	$\begin{bmatrix} 0 & 0 & 1 \\ 0 & 1 & 0 \\ -1 & 0 & 0 \end{bmatrix}$
<i>CBA</i>	$\begin{bmatrix} 0 & 0 & 1 \\ 0 & -1 & 0 \\ 1 & 0 & 0 \end{bmatrix}$
$\overline{BC\overline{A}}$	$\begin{bmatrix} 0 & 0 & -1 \\ -1 & 0 & 0 \\ 0 & 1 & 0 \end{bmatrix}$
$\overline{BC\overline{A}}$	$\begin{bmatrix} 0 & 0 & -1 \\ 1 & 0 & 0 \\ 0 & -1 & 0 \end{bmatrix}$
$\overline{C\overline{B\overline{A}}}$	$\begin{bmatrix} 0 & 0 & -1 \\ 0 & -1 & 0 \\ -1 & 0 & 0 \end{bmatrix}$
<i>C\overline{B\overline{A}}</i>	$\begin{bmatrix} 0 & 0 & -1 \\ 0 & 1 & 0 \\ 1 & 0 & 0 \end{bmatrix}$

Phenomenological theory describes the crystallography of a martensite transformation in purely mathematical terms.<sup>64</sup> The theory assumes that macroscopic deformation of a martensitic transformation is represented by a shape strain (S), which is resolved by the operation of lattice invariant strain (L), lattice deformation or Bain strain (B), and the rigid body rotation (R) sequentially on the parent crystal, as the equation below shows:

$$S = RBL \quad (7)$$

These strain and rotation are represented by 3×3 matrices.

The shape strain is an invariant plane strain which keeps a plane of the crystal (both shape and position) unaltered after the martensitic transformation. Bain strain transforms the parent crystal structure to the product crystal structure, but Bain strain is not an invariant plane strain. The function of the lattice invariant strain is to change the shape of the transformed volume, but not to change the crystal structure so as to get an undistorted plane. Typical lattice invariant strain involves slip and twinning. After L and B strain are accommodated, a rigid body rotation of the crystal is required to ensure that the undistorted plane is also unrotated. Based on the crystal structures and lattice parameters of the parent and product phases, the lattice correspondence between these two structures and the elements (plane and direction) of the lattice invariant strain L, the calculation of the PTMT can give rise to information like the habit plane of the martensite plates (the invariant plane), the magnitude of the lattice invariant strain, the magnitude and direction of the shape strain, and the orientation relationship between the parent and product phases.

The calculation of Bain strain requires knowledges of the lattice parameters of the parent and product crystal structures. As Figure 28 illustrates, for correspondence A, the tetragonal crystal structure transformation is achieved by compressing along the  $[100]_t$  axis, and expanding along

both the  $[001]_t$  and  $[010]_t$  axes. The deformations  $\eta_i$  along  $[100]_t$ ,  $[010]_t$ , and  $[001]_t$  axes are:

$$\eta_1 = c_m/a_t \quad (8)$$

$$\eta_2 = b_m/b_t \quad (9)$$

$$\eta_3 = a_m/c_t \quad (10)$$

The matrix below is called the Bain strain:

$$\begin{pmatrix} \eta_1 & 0 & 0 \\ 0 & \eta_2 & 0 \\ 0 & 0 & \eta_3 \end{pmatrix} \quad (11)$$

The calculation of shape strain and the lattice invariant strain is not as simple as for Bain strain.

In the tetragonal to monoclinic phase transformation, there are multiple sets of lattice parameters for tetragonal ceria stabilized zirconia based on different compositions and/or thermal processing. The most common case is that the parent and product phases have similar lattice parameters as shown in Table V, and the correspondences and ORs as are shown in Figure 28. In this case, according to the calculation of PTMT, for correspondences A and B, the lattice parameters of the parent and product phases have the worst match, so they have the largest Bain strain. However, for correspondence B, the lattice invariant strain (L) of the  $\{101\}\{10\bar{1}\}_t$  slip system is almost zero, which compensates for the large Bain strain, making correspondence B more likely than correspondence A. For correspondence variant  $CAB$ , the magnitude of the lattice invariant strain is 0.00268, and the magnitude of the shape strain is 0.164; for correspondence variant  $ABC$ , the magnitude of the lattice invariant strain is 0.0344, and the magnitude of the shape strain is 0.164, which are the two favored correspondences of this martensitic transformation.<sup>60</sup> In addition, the two most common orientation relationships for this case reported by Hugo<sup>27,29</sup> are:

OR B-1	OR B-2
$(0\ 0\ 1)_m \sim    (1\ 0\ 0)_t$	$(1\ 0\ 0)_m \sim    (0\ 1\ 0)_t$
$[1\ 0\ 0]_m \sim    [0\ 1\ 0]_t$	$[0\ 0\ 1]_m \sim    [1\ 0\ 0]_t$
$[0\ 1\ 0]_m \sim    [0\ 0\ 1]_t$	$[0\ 1\ 0]_m \sim    [0\ 0\ 1]_t$

B-1 and B-2 differ by approximately  $9^\circ$  along the  $b_m$  axis as Figure 28 shows. A third, but less common OR C-2 is also reported <sup>29</sup>:

OR C-2
$(1\ 0\ 0)_m \sim    (1\ 0\ 0)_t$
$[0\ 0\ 1]_m \sim    [0\ 0\ 1]_t$
$[0\ 1\ 0]_m \sim    [0\ 1\ 0]_t$

**Table V:** Lattice Parameters of Monoclinic and Tetragonal Phases as Reported in Ref. 55 for 12mol% Ce-ZrO<sub>2</sub><sup>60</sup>

Phase	a (Å)	b (Å)	c (Å)	$\beta$
<b>Monoclinic</b>	5.203	5.217	5.388	98.91°
<b>Tetragonal</b>	5.128	-	5.224	-

Based on the CeO<sub>2</sub>-ZrO<sub>2</sub> phase diagram (Figure 29), a 10 mol% CeO<sub>2</sub>-ZrO<sub>2</sub> or 10Ce-PSZ composition was selected for this study to ensure a partially transformed microstructure could be observed at room temperature.<sup>65</sup> In this study, EBSD was used to quantify the crystallography of the t→m transformation in a sample of 10Ce-PSZ. PTCLab<sup>66</sup> was used to calculate the output of the phenomenological theory of the martensitic transformation and simulate pole figures to show the orientation relationships between the parent and product phases.

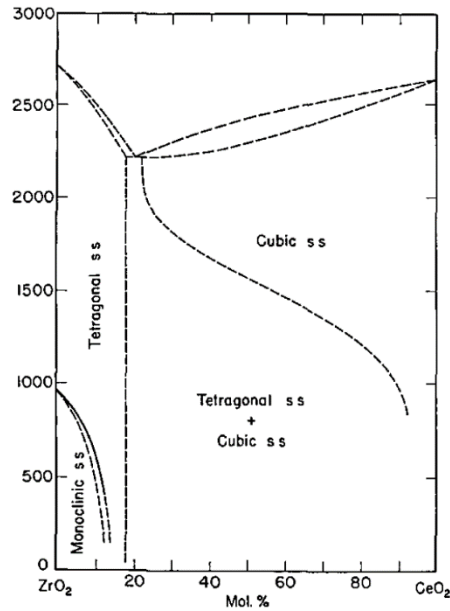


**Figure 29.** The phase diagram of CeO<sub>2</sub>-ZrO<sub>2</sub>. Reproduced with the permission from ref. 60 (Copyright 1975 American Ceramic Society, Inc).

## B. Experimental Procedure

### 1. Sample Preparation and Phase Identification

Sample 10Ce-PSZ was prepared by a solid-state reaction and sintering approach. Stoichiometric amounts of CeO<sub>2</sub> and ZrO<sub>2</sub> were blended in isopropanol with the molar ratio of 1:9. The mixture was then milled, dried, and formed into compacts by dry pressing. The compacts were sintered to 1600°C at 5K/minute with a two-hour dwell at maximum temperature, and then furnace cooled to room temperature. The phase structures were determined by X-ray Diffraction (XRD, Bruker D8) on a Scintag diffractometer with Cu K $\alpha_1$  radiation ( $\lambda=1.54 \text{ \AA}$ ) at a scanning rate of 0.01°/s in the 2 $\theta$  range from 5° to 120°. Phase identification was performed on the diffraction data with MDI-Jade 9 and the ICDD PDF 4+ database.

For scanning electron microscopy and electron backscatter diffraction (EBSD), the Ce-PSZ compact was impregnated into the automatic mounting press (TERAPRESS TP-7001B, PACE Technologies) with conductive (graphite) compression resin powder (PACE Technologies). Polishing was achieved with SiC grinding paper to 6.5  $\mu\text{m}$ , followed by vibratory polishing with a suspension of 0.05  $\mu\text{m}$  SIAMAT blue colloidal silica for 10 hours. To increase sample conductivity for EBSD studies, the vibratory polished 10Ce-PSZ sample was carbon coated using a high vacuum evaporator (Ladd Research) to a thickness of 10 nanometers.

## 2. PTMT Calculation

PTCLab<sup>66</sup>, a freely licensed software program, was used for calculation to show the predictions of PTMT and simulate the pole figures which denote the ORs. The two Crystallographic Information files (cif) provided by XRD phase identification were used as the input for PTCLab's calculation. For the purposes of this calculation, the slip system was chosen as the shear system with shear plane  $(110)_m$  and shear direction  $[\bar{1}\bar{1}0]_m$ . Tables VII, VIII, and IX indicate the lattice correspondence matrices utilized in assessing the martensitic transformation parameters. PTCLab<sup>66</sup> was used to simulate the pole figures to show the orientation relationships according to the principles described above.

## 3. Electron Microscopy

For EBSD analysis, the carbon coated sample was tilted 70° toward the EDAX Hikari Plus EBSD camera (EDAX, Inc., Mahwah, NJ USA) in a JEOL JSM-7800F field emission scanning electron microscope (JEOL USA Inc., Peabody, MA USA). The scan was taken at 15kV in high vacuum. The EBSD data were collected by TSL OIM DC 7 and automatically indexed with the

monoclinic and tetragonal \*.bmt files which were produced according to the crystallographic information of the sample from its XRD data using the TSL OIM Data Collection software.

## C. Results and Discussion

### 1. Results

Figure 30 shows the phase identification from XRD, shows that tetragonal and monoclinic phases are present in the polished sample. The lattice parameters of the two phases are provided in Table VI. Figure 31 shows the secondary electron image of a polished surface.

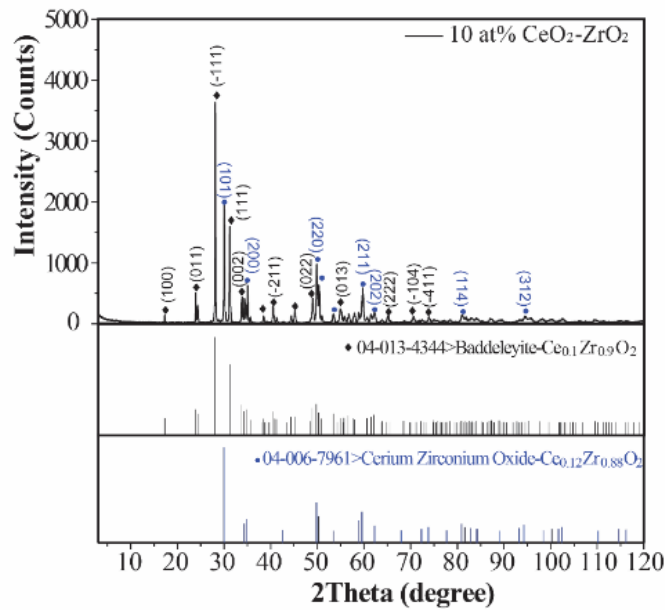


**Figure 30.** XRD data of the 10 mol% Ceria Doped Zirconia sample. Cu  $K\alpha_1$  radiation ( $\lambda=1.54$  Å), scanning rate 0.01°/s.

**Table VI.** Lattice Parameters of the Monoclinic and Tetragonal Ce-ZrO<sub>2</sub> Phases from the Closest Matching PDF Cards

Phase	a (Å)	b (Å)	c (Å)	$\beta$	Symmetry
Monoclinic	5.194	5.225	5.363	98.99	P21/c
Tetragonal	3.630	-	5.222	-	P42/nmc

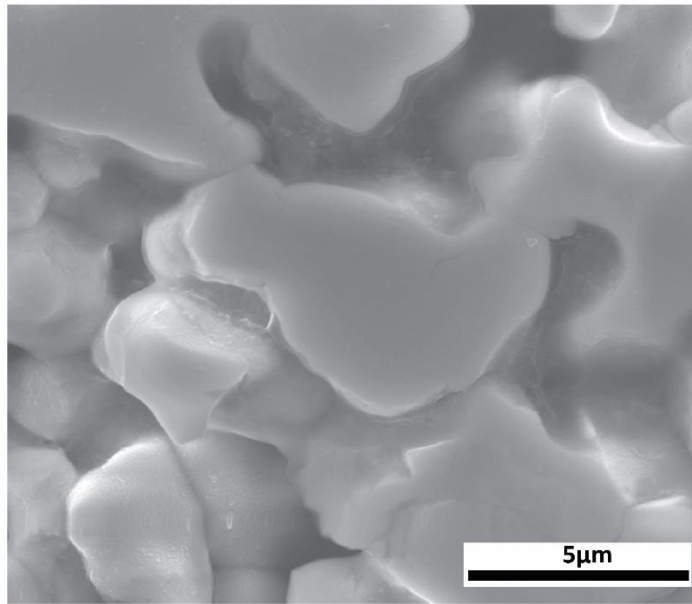


**Figure 31.** Secondary electron image of the polished Ce-ZrO<sub>2</sub> sample surface indicating porous structure.

Figure 32 shows the schematic of the deformation of unit cells during the tetragonal to monoclinic transformation for correspondence C of the 10 mol% Ce-ZrO<sub>2</sub> material according to the EBSD analysis. Figure 32a shows the unit cell of the parent tetragonal phase with the lattice parameters shown in Table VI. Figure 32b shows the co-ordinate transformation from tetragonal unit cell with lattice parameters  $a_{t1}$ ,  $b_{t1}$ , and  $c_{t1}$  to tetragonal unit cell with lattice parameters  $a_{t2}$ ,

$b_{t2}$ , and  $c_{t2}$ . Four tetragonal unit cells ( $a_{t1}$ ,  $b_{t1}$ , and  $c_{t1}$ ) are involved in the coordinate transformation, and the relationship between the lattice parameters of the two tetragonal unit cells are:

$$a_{t2} = b_{t2} = \sqrt{a_{t1}^2 + b_{t1}^2} \quad (12)$$

$$c_{t2} = c_{t1} \quad (13)$$

Figure 32c shows the monoclinic unit cell with the lattice parameters shown in Table VI after Bain strain. Note that, the smallest unit cell possible, after the Bain strain, is no longer the tetragonal phase ( $a_{t1}$ ,  $b_{t1}$ , and  $c_{t1}$ ) but is monoclinic phase ( $a_m$ ,  $b_m$ ,  $c_m$ , and  $\beta$ ).

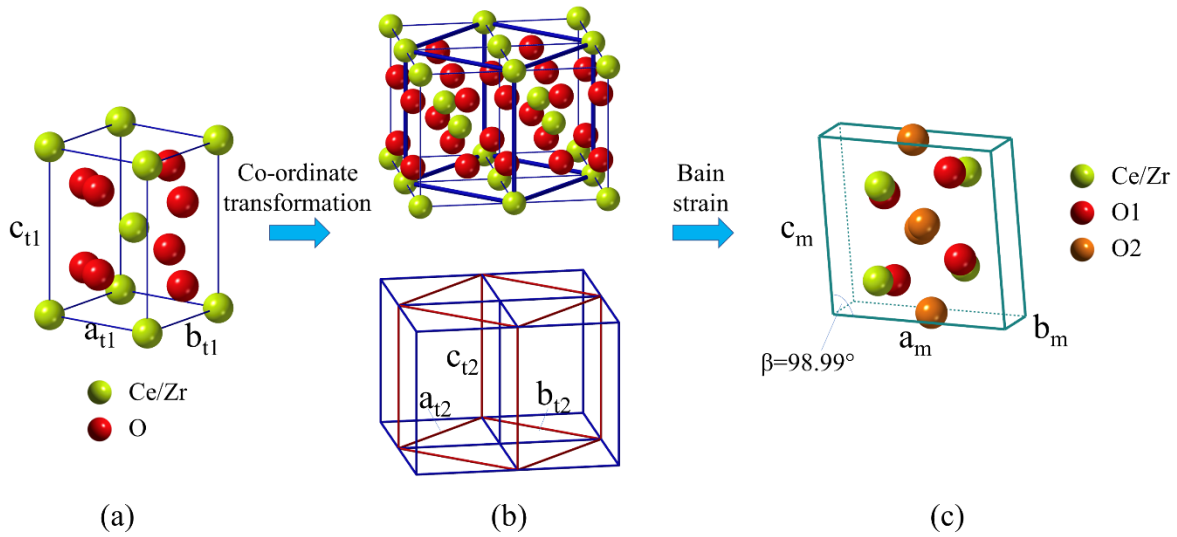


**Figure 32.** The schematic of the deformation of unit cells during the tetragonal to monoclinic transformation for correspondence C of the 10 mol% Ce-ZrO<sub>2</sub> sample, (a) the tetragonal unit cell; (b) co-ordinate transformation from tetragonal unit cell with lattice parameters  $a_{t1}$ ,  $b_{t1}$ , and  $c_{t1}$  to tetragonal unit cell with lattice parameters  $a_{t2}$ ,  $b_{t2}$ , and  $c_{t2}$ ; (c) after Bain strain, the transformed monoclinic unit cell.

The six orientation relationships are found to be that:

<b>OR A-1</b>	<b>OR A-2</b>
$(0\ 0\ 1)_m \sim    (1\ \bar{1}\ 0)_t$	$(1\ 0\ 0)_m \sim    (0\ 0\ 1)_t$
$[1\ 0\ 0]_m \sim    [0\ 0\ 1]_t$	$[0\ 0\ 1]_m \sim    [1\ 1\ 0]_t$
$[0\ 1\ 0]_m \sim    [1\ \bar{1}\ 0]_t$	$[0\ 1\ 0]_m \sim    [1\ \bar{1}\ 0]_t$
<b>OR B-1</b>	<b>OR B-2</b>
$(0\ 0\ 1)_m \sim    (1\ \bar{1}\ 0)_t$	$(1\ 0\ 0)_m \sim    (1\ 1\ 0)_t$
$[1\ 0\ 0]_m \sim    [1\ 1\ 0]_t$	$[0\ 0\ 1]_m \sim    [1\ \bar{1}\ 0]_t$
$[0\ 1\ 0]_m \sim    [0\ 0\ 1]_t$	$[0\ 1\ 0]_m \sim    [0\ 0\ 1]_t$
<b>OR C-1</b>	<b>OR C-2</b>
$(0\ 0\ 1)_m \sim    (0\ 0\ 1)_t$	$(1\ 0\ 0)_m \sim    (1\ \bar{1}\ 0)_t$
$[1\ 0\ 0]_m \sim    [1\ \bar{1}\ 0]_t$	$[0\ 0\ 1]_m \sim    [0\ 0\ 1]_t$
$[0\ 1\ 0]_m \sim    [1\ 1\ 0]_t$	$[0\ 1\ 0]_m \sim    [1\ 1\ 0]_t$

Tables VII, VIII and IX show the PTCLab<sup>66</sup> output of the PTMT prediction for correspondence A, B, and C, respectively. Comparing the magnitude of the shape strain  $S$  for the three correspondences, they are almost the same. Comparing the magnitude of the lattice invariant shear  $g$  among different ORs, A-1, A-2, C-1, and C-2 have more or less the same  $g$  values, while the  $g$  values for B-1 and B-2 are much smaller.

**Table VII.** PTCLab Output of the PTMT Calculation for Correspondence A

Solution #	1	2
<b>s</b>	-0.16448	0.16448
<b>d</b>	$[-0.70723 \ -0.70699 \ -0.00005]_t$	$[-0.17914 \ -0.21396 \ 0.96028]_t$
<b>g</b>	0.03556	0.0379
<b>h</b>	$(0.1279 \ 0.14508 \ -0.98112)_t$	$(-0.70192 \ -0.70362 \ 0.96028)_t$
<b>OR</b>	A-1	A-2
	Lattice correspondence matrix $\begin{bmatrix} \mathbf{0} & \mathbf{0} & \mathbf{1} \\ \mathbf{0.5} & \mathbf{-0.5} & \mathbf{0} \\ \mathbf{0.5} & \mathbf{0.5} & \mathbf{0} \end{bmatrix}$	
	Slip plane $(\mathbf{0.5} \ \mathbf{-0.5} \ \mathbf{1})_t$ slip direction $[\mathbf{-1} \ \mathbf{1} \ \mathbf{1}]_t$	

\* s - Magnitude of shape strain; d - Shape strain direction; g - Magnitude of Lattice invariant shear; h - Habit plane.

**Table VIII.** PTCLab Output of the PTMT Calculation for Correspondence B

Solution #	1	2
<b>s</b>	-0.16448	0.16448
<b>d</b>	$[-0.55376 \ 0.83268 \ -0.00049]_t$	$[0.70716 \ 0.70705 \ 0.00012]_t$
<b>g</b>	0.00132	0.00132
<b>h</b>	$(-0.65049 \ -0.75952 \ -0.00016)_t$	$(-0.48785 \ 0.87293 \ 0.00098)_t$
<b>OR</b>	B-1	B-2
	Lattice correspondence matrix $\begin{bmatrix} \mathbf{0.5} & \mathbf{-0.5} & \mathbf{0} \\ \mathbf{0} & \mathbf{0} & \mathbf{1} \\ \mathbf{0.5} & \mathbf{0.5} & \mathbf{0} \end{bmatrix}$	
	Slip plane $(\mathbf{0.5} \ \mathbf{-0.5} \ \mathbf{1})_t$ slip direction $[\mathbf{-1} \ \mathbf{1} \ \mathbf{1}]_t$	

\* s - Magnitude of shape strain; d - Shape strain direction; g - Magnitude of Lattice invariant shear; h - Habit plane.

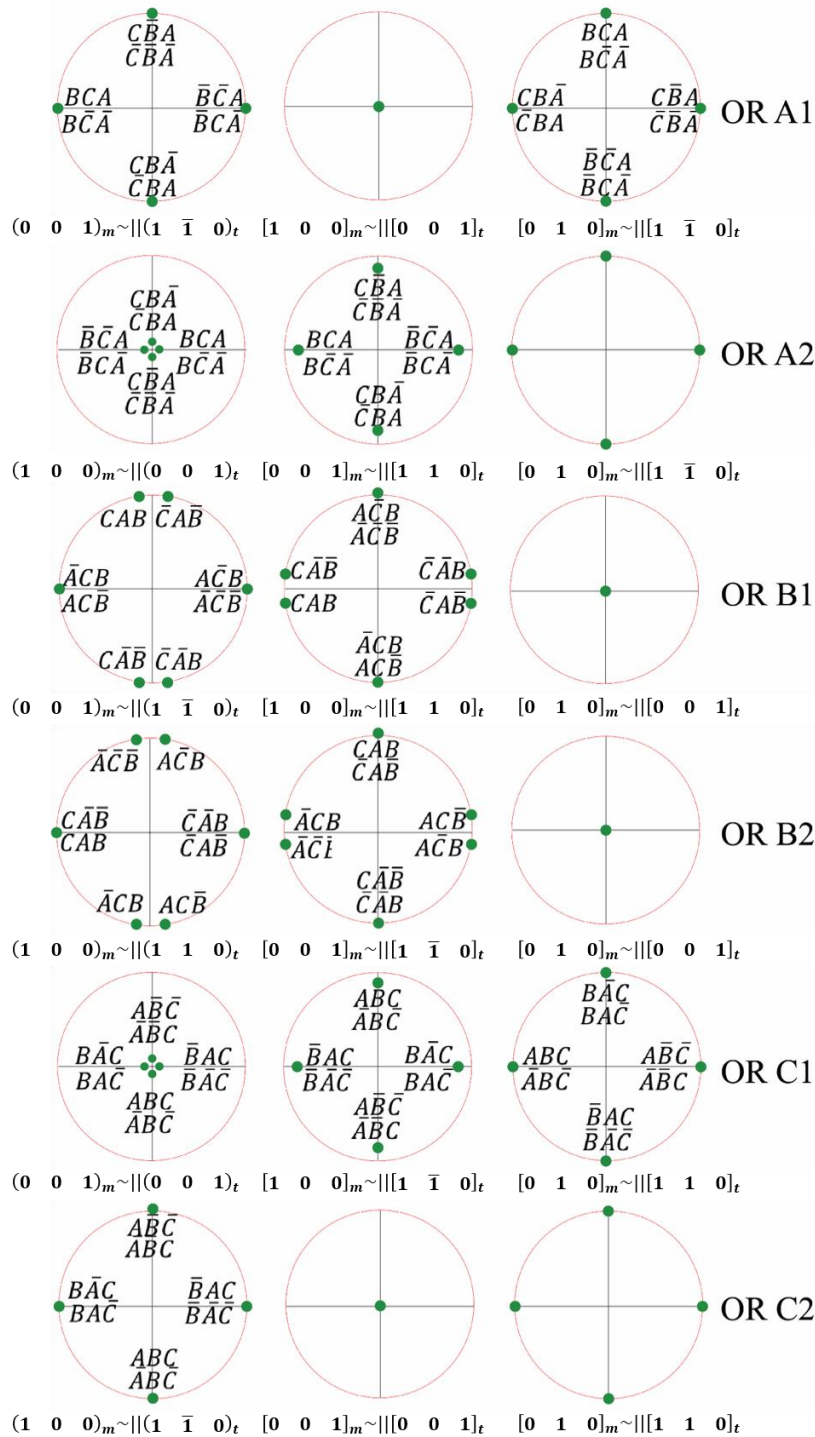
**Table IX.** PTCLab Output of the PTMT Calculation for Correspondence C

<b>Solution #</b>	<b>1</b>	<b>2</b>
<b>s</b>	0.16129	0.16129
<b>d</b>	$[0.71853 \quad -0.69242 \quad -0.06542]_t$	$[0.11038 \quad -0.11489 \quad -0.98723]_t$
<b>g</b>	0.03158	0.03964
<b>h</b>	$(0.09198 \quad -0.09274 \quad -0.99143)_t$	$(0.28793 \quad -0.90246 \quad -0.32042)_t$
<b>OR</b>	C-1	C-2
	Lattice correspondence matrix $\begin{bmatrix} 0.5 & -0.5 & 0 \\ 0.5 & 0.5 & 0 \\ 0 & 0 & 1 \end{bmatrix}$	
	Slip plane $(1 \ 0 \ 0)_t$ slip direction $[0 \ -2 \ 0]_t$	

\* s - Magnitude of shape strain; d - Shape strain direction; g - Magnitude of Lattice invariant

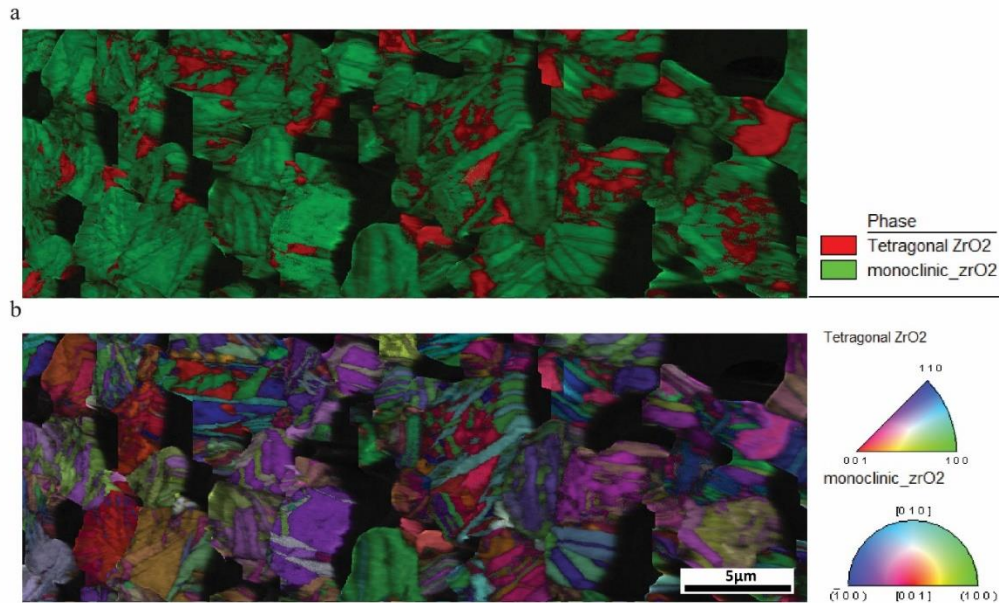
shear; h - Habit plane.

Figure 33 shows the simulated pole figures, to denote the parallel relationships in OR A-1, A-2, B-1, B-2, C-1, and C-2. There are eight different variants for each OR. In some of the pole figures the points of different variants coincide. It is worth noting that when plotting the parallel relationships between planes, the point denoting plane normal is shown in the stereographic projection rather than the big circle.



**Figure 33.** The simulated pole figures, to denote the parallel relationships in OR A-1, A-2, B-1, B-2, C-1, and C-2.

Figure 34 shows the Image Quality (IQ) (grayscale) + phase map (color scale) (fig. 34a) and the Image Quality (IQ) (grayscale) + Inverse Pole figure (IPF) map (color scale) (fig. 34b) of one  $12.54 \times 36.67 \mu\text{m}^2$  region. Figure 35 shows the IQ + phase map (fig. 35a) and the IQ + IPF map (fig. 35b) of another  $12.54 \times 36.67 \mu\text{m}^2$  region. The volume fraction of the monoclinic phase is found to be 70-80% in both. It can be seen from Figures 34 and 35 that in different tetragonal grains, the product monoclinic phase has a different morphology - needle like or martensite laths. In each tetragonal grain, either the martensitic needles or laths are twin-related. Upon further inspection of the EBSD maps in Figure 34 and 35, it is found that in one tetragonal grain, several sets of twin-related martensite plates may have formed. As seen in Figure 36, in one set of the twin-related martensite plates, the orientation relationship come from the same correspondence; in another set of twin-related martensite plates, the orientation relationship come from two different correspondence (the detailed description is shown in the following paragraph). It is also found that all the six orientation relationships are observed in the studied system.



**Figure 34.** (a) The IQ + phase map and (b) the IQ + IPF map of a  $12.54 \times 36.67 \mu\text{m}^2$  region on the sample surface.

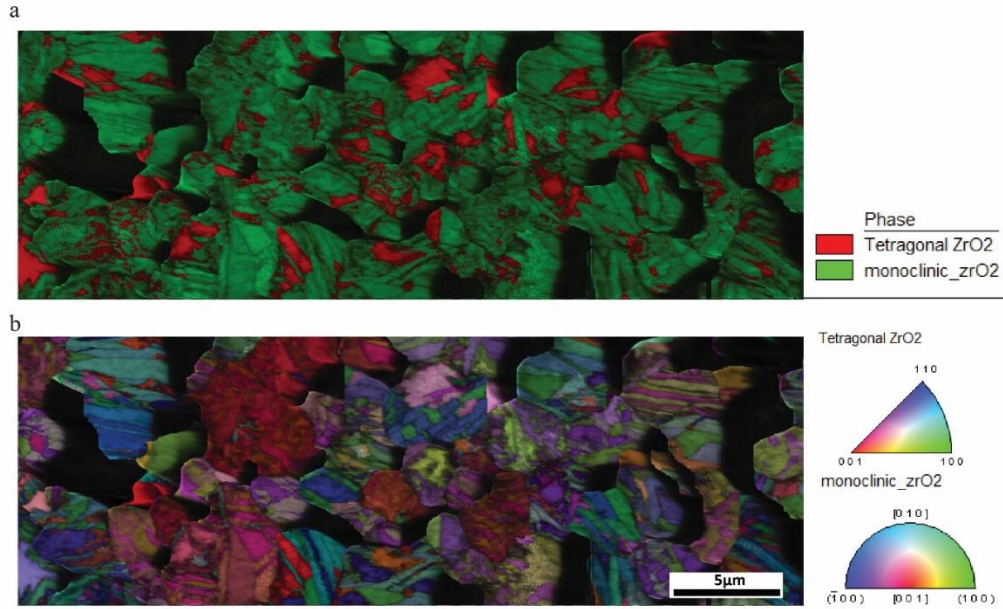


**Figure 35.** (a) The IQ + phase map and (b) the IQ + IPF map of another  $12.54 \times 36.67 \mu\text{m}^2$  region on the sample surface.

If tetragonal grains are extracted individually, they can be rotated for consistency, and the (100), (001), [100], [010] and [001] pole figures of the monoclinic phase shown (Figures 36, 37, and 38). Figure 36 shows the EBSD maps and the pole figures of the multi-oriented martensite plates in a tetragonal grain. Figure 36a and 36b shows the phase and IPF map before rotation. Figure 36c shows the IPF map after rotation. In Figure 36c, there is a marked rectangular area composed of four martensite plates labeled as 1, 2, 3 and 4. The four martensite plates have the orientation relationship of C-1 and C-2. This rectangle morphology is similar to the observation of the pyramid-type martensite plates by Deville<sup>30</sup> and Onda<sup>25</sup> with Atomic Force Microscopy technology. Figure 36d shows the (100), (001), [100], [010] and [001] pole figures of the monoclinic phase after rotation, and the color of the poles corresponds to the colors of Figure 36c. Comparing Figure 36d with Figure 33, it is found that this grain contains all six ORs: A-1, A-2, B-1, B-2, C-1, and C-2. Comparing Figure 36c and 36d, some interesting features are found: (1)

the aqua colored martensite plates in Figure 36c have the B-1 or B-2 OR and they are twin-related with the blue martensite plates whose have the A-1 OR; (2) the blue colored martensite plates in Figure 36c which have the A-1 and A-2 ORs are twin-related with each other; (3) the marked red region of the monoclinic phase in Figure 36c is composed of four martensite plates which have C-1 and C-2 ORs; (4) the OR of green martensite plates do not match any of the six previously-identified ORs.

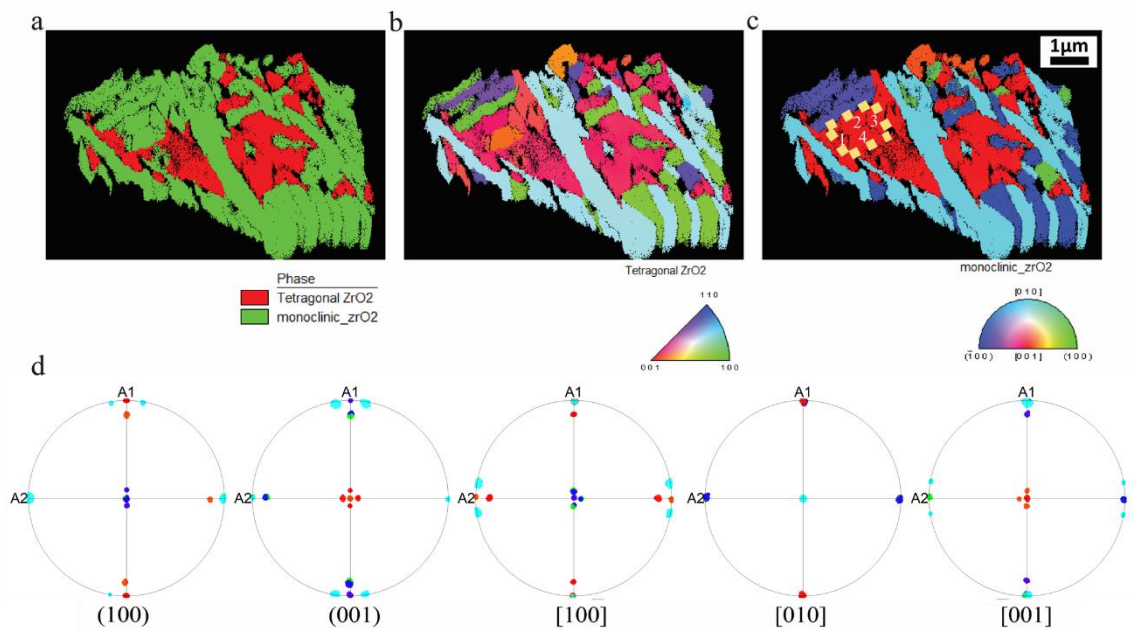


**Figure 36.** The EBSD maps and the pole figures of the multi-oriented martensite plates in a tetragonal grain (a) the phase map; (b) the IPF map of the extracted tetragonal grain; and (c) the IPF map after rotation; (d) the (100), (001), [100], [010] and [001] pole figures of the monoclinic phase after rotation.

Figure 37 shows the EBSD maps and the pole figures of the needle like martensite plates in another tetragonal grain. Figure 37a and 37b shows the phase and IPF map before rotation. From Figure 37b, it can be seen that martensite plates are parallel to each other. The end of each two adjacent plates form an angle that denotes different habit planes. The angle between plate 1 and 2

is roughly  $35^\circ$ . There are two angles between plate 2 and 3. The angle is roughly  $23^\circ$  or  $42^\circ$  (see callout in Figure 37b). The angle between plates 4 and 5 is  $23^\circ$ . The angle between plates 6 and 7 is roughly  $35^\circ$ . Figure 37c shows the IPF map after rotation, and Figure 37d shows the (100), (001), [100], [010] and [001] pole figures of the monoclinic phase after rotation. Comparing Figure 37d with Figure 33, it is found that this grain contains B-1 and B-2 ORs. The B-1 and B-2 ORs plates formed pairs, and the “V” shape space between each pair was either untransformed or transformed to martensite plates whose OR does not match any of the six ORs.

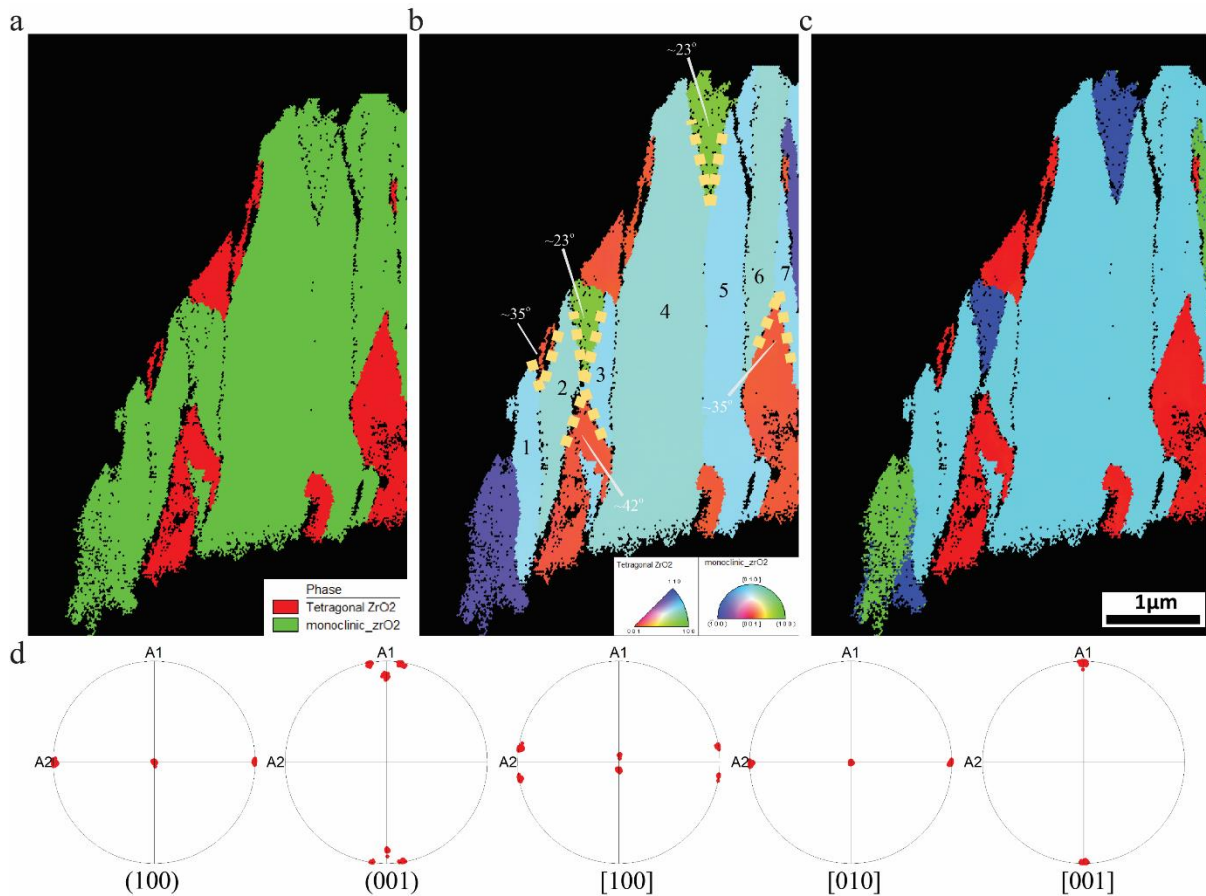


**Figure 37.** The EBSD maps and the pole figures of the needle like martensite plates in another tetragonal grain (a) the phase map; (b) the IPF map of the extracted tetragonal grain; and (c) the IPF map after rotation; (d) the (100), (001), [100], [010] and [001] pole figures of the monoclinic phase after rotation.

Figure 38 shows the EBSD maps and the pole figures of the twin-related martensite laths in a tetragonal grain. Figure 38a and 38b shows the phase and IPF map before rotation. Figure 38c shows the IPF map after rotation, and Figure 38d shows the (100), (001), [100], [010] and [001] pole figures of the monoclinic phase after rotation. Comparing Figure 38d with Figure 33, it can be concluded that this grain contains both C-1 and C-2 ORs. These two ORs alternate from left to right in the grain.

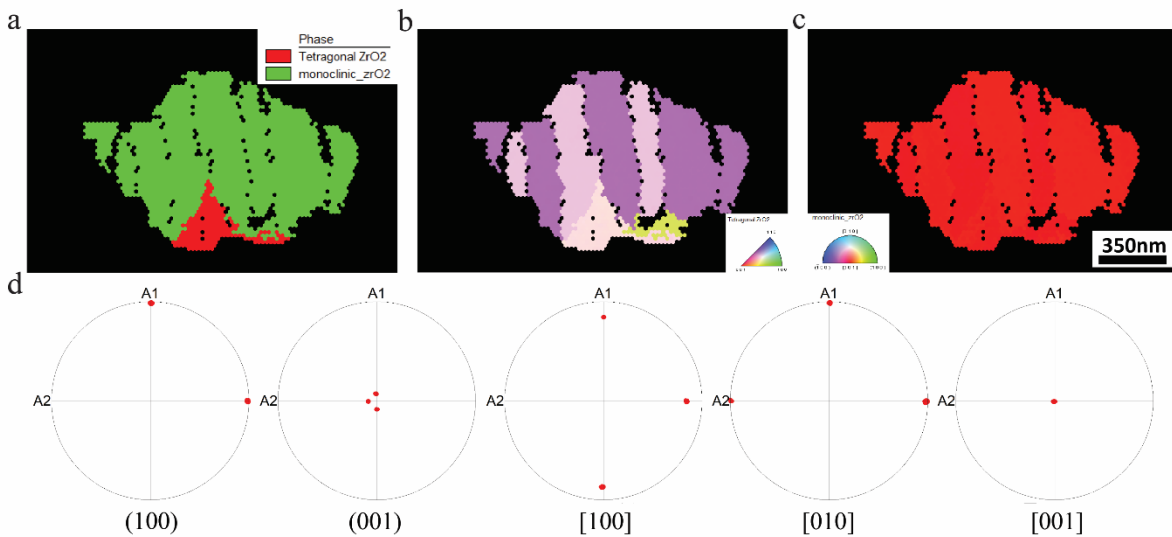


**Figure 38.** The EBSD maps and the pole figures of the twin-related martensite laths in a tetragonal grain (a) the phase map; (b) the IPF map of the extracted tetragonal grain; and (c) the IPF map after rotation; (d) the (100), (001), [100], [010] and [001] pole figures of the monoclinic phase after rotation.

## 2. Discussion

### 2.1 Martensite Transformation in 10 mol% Ceria Doped Zirconia

Martensite plates are known to be self-accommodating, and there are two ways to realize the self-accomodation.<sup>60</sup> One way is to form twin-related martensite plate pairs; the other way is

that the transformation in one grain catalyzes the transformation in the neighboring grains. As seen in Figures 34 and 35, the twin-related martensite plates are omnipresent, while the autocatalysis of phase transformation between grains is rarely observed. The more common case is that the martensite transformation happens in each grain individually - the martensite plates grow towards each other in parallel fashion or at intersecting angles.

For the twin-related martensite plates, the morphology can be martensite laths in which case the orientation relationship of the plates with the parent grain belong to the same correspondence, as shown in Figure 38 for the case of C-1 and C-2 OR plates. The angular difference between the B-1 and B-2 OR plates is roughly  $9^\circ$  along the  $c_m$  axis. This observation is in agreement with prior observations in the literature.<sup>60</sup> The twin-related pair can also be needle-like martensite plates. Figure 39 shows the schematic of the twin-related needle-like martensite plate pair.<sup>60</sup> The angle of the “V” shape is either  $35^\circ$  or  $10.5^\circ$ , when the orientation relationship of the plates belong to correspondence B. As shown in Figure 37, the orientation relationship of the plates is either B-1 or B-2 which matched the case in Figure 39. However, some of the observed angles of the “V” shape are different from the predicted angles. An angle of Figure 38b was observed to be  $35^\circ$ , but the  $10.5^\circ$  angle was not observed, replaced instead by two  $23^\circ$  angles and a  $42^\circ$  angle as seen in Figure 37.

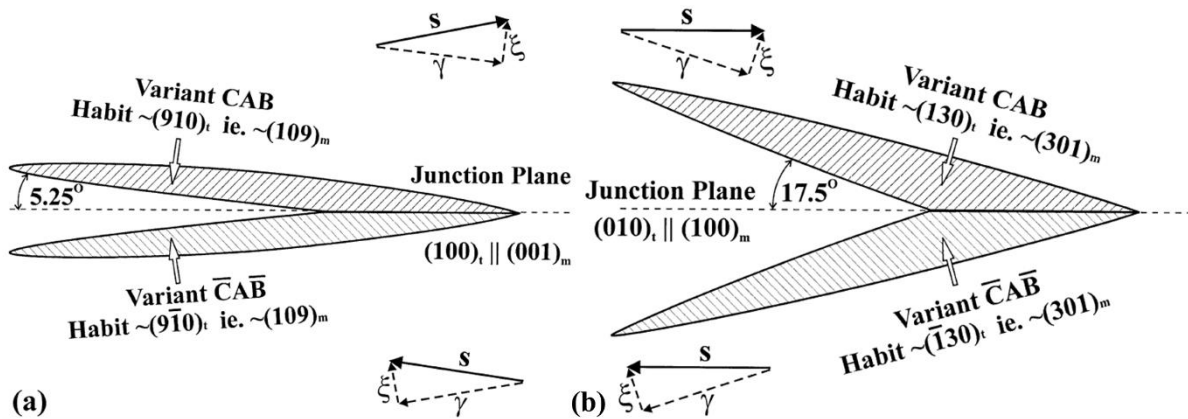


**Figure 39.** The schematic of the twin-related needle-like martensite plate pair. The arrangement is predicted by PTMT. Reproduced with the permission from ref. 55 (Copyright 2002 Elsevier).

The last, but still noteworthy is, feature that all the six orientation relationships appeared in the present work. No conclusion as to preferred ORs can be drawn from the present work.

## 2.2 Interpretation and Improvement of the Automatic Indexing Procedure

The application of EBSD to ceramics or other electrically insulative materials can provide some unique information unavailable from other techniques, such as morphology and orientation information simultaneously for the materials at the micrometer scale. However, there are two major challenges that limit the utilization of EBSD on these materials: charging and indexing low symmetry crystal structures.

When the incident electron beam interacts with non-conducting materials, a charge accumulates on the surface, which causes issues such as scanning faults, image drift, or charging contamination on the scanning region. To solve this problem, conductive coatings on the sample surface or low vacuum EBSD is usually used. Nevertheless, both methods can reduce the quality of the EBSD patterns, resulting in increased pattern contrast blurring, diminishing the ability to accurately index the pattern.<sup>67</sup>

The other challenge is the low symmetry of the crystal structures.<sup>67,68</sup> Misindexing happens more often in low symmetry ceramics as compared to higher symmetry metals.<sup>23</sup> EI-Dasher showed an example of an AlN-TiB<sub>2</sub> ceramic composite in which AlN structure exhibits P6<sub>3</sub>mc symmetry and TiB<sub>2</sub> exhibits P6/mmm symmetry.<sup>67</sup> There are low index reflectors in both crystal structures whose interplanar angles are similar. The automatic indexing routine determines the reflectors (planes) via the unique interplanar angle between different planes of the crystal structure, so the automatic indexing routine may fail to identify which phase the Kikuchi patterns belong to if the interplanar angles of the two phases are the same or similar.

According to Field, if the Average Confidence Index (CI) value for the whole map is below 0.1, it means that some of the automatic indexing points may be wrong.<sup>69</sup> To interpret and improve the automatic indexing route, it's necessary to make clear what the procedures of the automatic indexing process are. According to Wright,<sup>3,8</sup> the automatic indexing steps are: (1) background noise subtraction for the EBSP images; (2) finding bands for each EBSP by Hough transform; (3) band analysis calculation including interplanar angle, bandwidth angle and lattice orientation calculation; (4) comparing the calculated results with the interplanar look-up tables which were constructed according to the crystallographic information of the phases in the sample; (5) finding the most possible solution of the orientation.

In this procedure, the Hough transform is a crucial step to get a good CI value for automatic indexing. Hough transform is used to find the bands of the Kikuchi pattern. The gray scale band is recorded as a bright point in the Hough space. The size of the point corresponds to the width of the band. When a butterfly shaped mask is applied on the Hough space, the center of the point which represents the center line of the band is enhanced and easily localized. In this way the band position is localized.<sup>70</sup> It is found that the Hough transform can measure the band position

correctly, but that the calculated bandwidth is different from the one in the interplanar look-up table.

The other key step to get a good CI value is choosing proper reflectors in the look-up table so that the Hough transform calculated reflectors accurately match the look-up table. As Nowell showed, with the decrease of the interplanar angle tolerances, the votes number (means the number of the matched reflectors) and the difference of the votes number between solution 1 and 2 (which influence the CI value) reduced significantly. An interplanar angle tolerance of  $3^\circ$  is typically needed for most of the materials.<sup>44</sup> For some crystal materials, such as the monoclinic structure of Figure 30, there are many reflectors. The angular difference between any certain two reflector pairs can be less than  $3^\circ$ , so for these materials, choosing proper reflectors in the look-up table to avoid misindexing between the reflectors with the angular difference less than  $3^\circ$  is important to get a good CI value.

The coexistence of two phases will also influence the correctness of the indexing. If two band pairs from the two phases separately have similar interplanar angles, the CI value in that case is usually very low, even though the CI value is larger than 0.1 if the pattern is indexed individually with tetragonal or monoclinic look-up table. For improving the indexing of the coexistent phases, increasing the Max Peak Count number in the Hough page of the data collection software can lead to a solution. In the case where the tetragonal and monoclinic phases coexist, a Max Peak Count number of 10 can get the acceptable CI value for indexing. The increase of the Max Peak Count number will decrease the CI value, but the phases can be effectively distinguished, so there is a balance between the selection of the Max Peak Count number and the CI value.

## D. Conclusion

The tetragonal to monoclinic martensitic transformation in a 10 mol% Ceria doped Zirconia was studied via EBSD, XRD, and SEM. The prediction via PTMT for this material was also calculated by PTCLab software.

The lattice parameters measured by XRD according to the closest matching PDF cards are  $a_t = b_t = 3.63 \text{ \AA}$ , and  $c_t = 5.222 \text{ \AA}$  for the parent tetragonal phase;  $a_m = 5.194 \text{ \AA}$ ,  $b_m = 5.225 \text{ \AA}$ ,  $c_m = 5.363 \text{ \AA}$ , and  $\beta = 98.99^\circ$  for the product monoclinic phase. The SEM showed that the sample is porous.

SEM-based EBSD was used to observe the morphology of the transformed phase and measure the orientation relationship between parent and product phases simultaneously. Three different morphologies were observed for the monoclinic phase - martensite lath, needle-like martensite plate, and pyramid-type martensite plate. The correspondence between the parent and product lattice was found to be that the diagonal of the plane which is perpendicular to the  $c_t$  axis in the parent unit cell becomes one edge of the product unit cell by EBSD. The six different orientation relationships (A-1, A-2, B-1, B-2, C-1 and C-2) were simultaneously observed from the material via EBSD.

The calculation of PTMT for this material shows that the shape strain is similar for the different orientation relationships, while the lattice invariant strain is not the same for different orientation relationships. The A-1, A-2, C-1 and C-2 orientations have similar lattice invariant strain, B-1 and B-2 have the same lattice invariant strain, but the magnitude is much smaller (close to 0) than the other four orientation relationships.

The experimental results and the theoretical prediction together show that from the energy point of view B-1 and B-2 are the preferential orientation relationships, while the experimental

observation of all the six orientation relationships means that the material can handle the energy variance of different orientation relationships, which gives a comprehensive understanding of the martensitic transformation in ceria partially stabilized zirconia. The new features revealed in the present work are valuable complements to the prior study of martensitic transformation in ceramics.

There are low index reflectors in both the tetragonal and monoclinic crystal structures whose interplanar angles are similar. By choosing proper reflectors in the look-up table of both the tetragonal and monoclinic phases, misindexing of those low difference reflectors can be avoided. In the current study, it was also found that the band position of the Kikuchi pattern can be located correctly via the Hough transform, but that the measured bandwidth is then different from the theoretical value in the look-up table.

## IV. SUMMARY AND CONCLUSIONS

This dissertation focused on the study of phase transformation in AISI 5160 steel and ceria partially stabilized zirconia via Electron Backscatter Diffraction. For the AISI 5160 steel, a new method based on Kernel Average Misorientation (KAM) was developed to quantitatively identify different phase transformation products, such as martensite, bainite, pearlite, and ferrite by EBSD. For the ceria partially stabilized zirconia, the martensitic transformation was investigated by EBSD. The phenomenological theory of martensitic transformations (PTMT) was calculated and matched with experiment. The experimental results and the theoretical prediction together gave a comprehensive understanding of the martensitic transformation in ceria partially stabilized zirconia.

For steel, there are four room-temperature constituents which form under different thermal process conditions. These four room-temperature constituents are: martensite, bainite, pearlite, and ferrite. After chemical etching, they appear morphologically different under the microscope. However, their crystal structures are too similar to be precisely identified.

To date, the most efficient methods for quantitatively identifying the four constituents are color etching and the ASTM manual point count method. The color etching method applies etchants to yield distinct colors for different constituents under the optical microscope. One drawback of the color etching method is that the spatial resolution of the optical microscope is too limited to work with fine grain steels, such as nanoscale grains. The ASTM manual point count method applies a statistical method to measure the volume fraction of the constituents, and gives a confidence interval for the volume fraction results. The disadvantage of the ASTM manual point count method is that it needs tedious manual work, and it relies on etching so that the results can be influenced by etchant types or etching conditions.

To minimize the influence of etching, and to reduce the manual work, a method based on EBSD was developed for identifying and quantifying the four room-temperature constituents in steels. KAM was found to be a good indicator of plastic strain in crystalline materials, and KAM maps enabled visualization of microscale plastic strain. Different thermal processing yield different constituents or phases in steels which contain different amount of plastic strain. For example, diffusion of carbon and other alloying atoms in the steels during thermal processing causes the distortion of the crystal lattice of iron; heat treatment conditions such as temperature, cooling rate, or annealing time may result in imperfections in the lattice of the polycrystalline samples. Lattice distortion and lattice imperfections are forms of plastic strain; therefore, the plastic strain in different thermal processing products can be visualized in KAM maps.

After careful investigation of the KAM value and the KAM map for different constituents in AISI 5160 steel, it was found that the features of the KAM frequency distribution curve for every constituent are: (1) the shape of the curves are similar; (2) at 1NN, every curve begins in the range of 0-1 degree, i.e. a false blue color in the KAM map; and (3) with an increase of the NN#, the curve will broaden and move towards the direction of larger KAM value. Nevertheless, for different constituents, the difference of the curves is that with the increase of the NN#, the reducing rate of the fraction of KAM values under  $1^\circ$  in the KAM maps is unique to the constituent. Therefore, for a two-constituent steel, at certain NN#, the fraction of the KAM values under  $1^\circ$  for one constituent will completely disappear, and the remaining fraction of KAM values under  $1^\circ$  in the KAM map can be considered to be the volume fraction of the other constituent.

For ceria partially stabilized zirconia, the tetragonal to monoclinic martensitic transformation in a 10 mol% CeO<sub>2</sub> doped ZrO<sub>2</sub> was investigated. Because transformation toughening in ceramics utilizes the shape and volume distortion, the martensitic transformation is

as a toughening mechanism. Therefore, understanding the details of the martensitic transformation is helpful for the improvement of the toughness of ceramics and commercial application of these materials.

The martensitic transformation (tetragonal to monoclinic) in zirconia has been extensively studied by researchers via TEM, XRD, or AFM. Nowadays, SEM-based EBSD is increasingly applied to the study. The advantage of EBSD technology is that it can observe the region on the micron scale of the sample surface and can simultaneously give microstructural and crystallographic information. This is a valuable complement to the prior study of martensitic transformation in ceramics and would facilitate a more comprehensive understanding of the martensitic transformation in zirconia.

It is found by researchers that there are several sets of lattice parameters of the parent and product crystal structures for ceria stabilized zirconia based on different composition or thermal processing. In this work the lattice parameters measured by XRD are  $a_t = b_t = 3.63 \text{ \AA}$ , and  $c_t = 5.222 \text{ \AA}$  for the parent tetragonal phase;  $a_m = 5.194 \text{ \AA}$ ,  $b_m = 5.225 \text{ \AA}$ ,  $c_m = 5.363 \text{ \AA}$ , and  $\beta = 98.99^\circ$  for the product monoclinic phase. For this material and these lattice parameters, the correspondence between the parent and product lattice was found to be that the diagonal of the plane which is perpendicular to the  $c_t$  axis in the parent unit cell becomes one edge of the product unit cell, and the six different orientation relationships (A-1, A-2, B-1, B-2, C-1 and C-2) were observed from the material via EBSD experimentally.

The calculation of PTMT for this 10 mol% CeO<sub>2</sub> doped ZrO<sub>2</sub> showed that the shape strain is similar for different orientation relationship, while the lattice invariant strain differs specifically, the A-1, A-2, C-1 and C-2 have similar lattice invariant strain; B-1 and B-2 have the same lattice

invariant strain, but the magnitude is much smaller (close to 0) than the other four orientation relationships.

## V. FUTURE WORK

The KAM method reduced the dependency of volume fraction measurement for different constituents in steels on etching and drastically limited manual work time when compared to color etching and ASTM manual point count methods. Nevertheless, there are still some drawbacks of this method:

- The results of the KAM method presently yield only semi-quantitative volume fractions, rather than precise values.
- Furthermore, the choice of the points of the 1<sup>st</sup> derivative  $d\lambda/d(NN\#)$  vs.  $NN\#$  curves for volume fraction is still artificial.  $\lambda$  = the fraction of KAM values under 1°.
- It is found that there is a linear relationship between KAM FWHM value and Vickers hardness. However, full understanding and application of this information is still not clear.

Future, efforts to improve the precision of the KAM method and on the interpretation of the linear relationship between KAM FWHM value and Vickers hardness are indicated. This would enable the KAM method to be a rapid quantitative method for steels.

The investigation of the martensitic transformation of zirconia revealed new features not previously reported in other zirconia system. Although these features have been explained, additional work remains:

- More grains should be investigated to get a statistical conclusion for the lattice correspondences, orientation relationships, and presence of preferential correspondence/orientation relationship for surface transformation or bulk transformation.
- Other characterization techniques can be applied, such as TEM, to precisely measure the habit planes, also the junction plane and angle of the twin-related martensite plates.

- In addition, efforts should be made to identify the relations among different processing, composition, lattice parameters, and the resulting crystallography of the martensitic transformation. This would give a comprehensive guideline for fabrication and commercial application.

## REFERENCES

1. R.H. Hannink, P.M. Kelly, and B.C. Muddle, "Transformation Toughening in Zirconia - Containing Ceramics," *J. Am. Ceram. Soc.*, **83** [3] 461-87 (2000).
2. S. Kikuchi, "Diffraction of Cathode Rays by Mica," *Proc. Imp. Acad (Tokyo)*, **4** [6] 271-4 (1928).
3. S.I. Wright and B.L. Adams, "Automatic Analysis of Electron Backscatter Diffraction Patterns," *Metall. Trans. A*, **23** [3] 759-67 (1992).
4. D.J. Dingley, "The Development of Automated Diffraction in Scanning and Transmission Electron Microscopy"; pp. 1-18 in *Electron Backscatter Diffraction in Materials Science*. Springer, Medford, MA, 2000.
5. P.J. Goodhew, J. Humphreys, and R. Beanland, *Electron Microscopy and Analysis*; pp. 34-7. CRC Press, Boca Raton, FL, 2000.
6. D.B. Williams, C.B. Carter, and P. Veysiere, *Transmission Electron Microscopy: A Textbook for Materials Science*, Vol. 10; pp. 290-7. Springer, Medford, MA, 1998.
7. S.I. Wright, "Fundamentals of Automated EBSD"; pp. 51-64 in *Electron Backscatter Diffraction in Materials Science*. Springer, Medford, MA, 2000.
8. S.I. Wright, "Individual Lattice Orientation Measurements Development and Application of A Fully Automatic Technique"; Ph.D. Thesis. Yale University, Ann Arbor, MI, 1992.
9. A.J. Schwartz, M. Kumar, B.L. Adams, and D.P. Field, *Electron Backscatter Diffraction in Materials Science*, Vol. 2; pp. 35-50. Springer, Medford, MA, 2009.
10. A.J. Schwartz, M. Kumar, B.L. Adams, and D.P. Field, *Electron Backscatter Diffraction in Materials Science*, Vol. 2; pp. 317-26. Springer, Medford, MA, 2009.
11. A.J. Schwartz, M. Kumar, B.L. Adams, and D.P. Field, *Electron Backscatter Diffraction in Materials Science*, Vol. 2; pp. 316-90. Springer, Medford, MA, 2009.
12. A.J. Schwartz, M. Kumar, B.L. Adams, and D.P. Field, *Electron Backscatter Diffraction in Materials Science*, Vol. 2; pp. 329-35. Springer, Medford, MA, 2009.
13. A.J. Schwartz, M. Kumar, B.L. Adams, and D.P. Field, *Electron Backscatter Diffraction in Materials Science*, Vol. 2; pp. 231-47. Springer, Medford, MA, 2009.
14. K. Rajan, "Representations of Texture in Orientation Space"; pp. 31-8 in *Electron Backscatter Diffraction in Materials Science*. Springer, Medford, MA, 2000.

15. N.C.K. Lassen, "Automated Determination of Crystal Orientations from Electron Backscattering Patterns"; Ph.D. Thesis. The Technical University of Denmark, Kongens Lyngby, Denmark, 1994.
16. S. Suwas and N.P. Gurao, *Crystallographic Texture in Materials*, Vol. 88; pp. 39-72. Springer, Medford, MA, 2008.
17. J.R. Michael, "Phase Identification Using Electron Backscatter Diffraction in the Scanning Electron Microscope"; pp. 75-89 in *Electron Backscatter Diffraction in Materials Science*. Springer, Medford, MA, 2000.
18. A.J. Wilkinson, "Measuring Strains Using Electron Backscatter Diffraction"; pp. 231-46 in *Electron Backscatter Diffraction in Materials Science*. Springer, Medford, MA, 2000.
19. S.I. Wright, M.M. Nowell, and D.P. Field, "A Review of Strain Analysis Using Electron Backscatter Diffraction," *Microsc. Microanal.*, **17** [3] 316-29 (2011).
20. R. Keller, A. Roshko, R. Geiss, K.A. Bertness, and T. Quinn, "EBSD Measurement of Strains in GaAs Due to Oxidation of Buried AlGaAs Layers," *Microelectron. Eng.*, **75** [1] 96-102 (2004).
21. L.N. Brewer, D.P. Field, and C.C. Merriman, "Mapping and Assessing Plastic Deformation Using EBSD"; pp. 251-62 in *Electron Backscatter Diffraction in Materials Science*. Springer, Medford, MA, 2009.
22. Z. Nishiyama, *Martensitic Transformation*; pp. 232-7. Elsevier, Atlanta, GA, 2012.
23. H.K.D.H. Bhadeshia, *Worked Examples in the Geometry of Crystals*, 2nd ed.; pp. 1-3. Institute of Materials, Brookfield, VT, 2001.
24. Z. Nishiyama, *Martensitic Transformation*; p. 7. Elsevier, Atlanta, GA, 2012.
25. T. Onda, S. Iwagaki, S. Morito, and M. Hayakawa, "Shape-Strain Analysis of Martensite in Ceria-Doped Zirconia," *Mater. Trans.*, **51** [5] 899-905 (2010).
26. A. Standard, "Standard Test Method for Determining Volume Fraction by Systematic Manual Point Count," *ASTM E562-08*, (2008).
27. G. Hugo, B.C. Muddle, and R. Hannink, "Crystallography of the Tetragonal to Monoclinic Transformation in Ceria-Zirconia," *Mater. Sci. Forum*, **34** 165-9 (1988).
28. R. Hannink, G. Hugo, and B.C. Muddle, "Reversal of the Tetragonal-Monoclinic Transformation in Ceria-Zirconia," *Mater. Sci. Forum*, **56**, 371-6 (1990).
29. G. Hugo and B.C. Muddle, "The Tetragonal to Monoclinic Transformation in Ceria-Zirconia," *Mater. Sci. Forum*, **56**, 357-62 (1990).

30. S. Deville, G. Guénin, and J. Chevalier, "Martensitic Transformation in Zirconia: Part II. Martensite Growth," *Acta Mater.*, **52** [19] 5709-21 (2004).
31. S. Dziazyk, E. Payton, F. Friedel, V. Marx, and G. Eggeler, "On the Characterization of Recrystallized Fraction Using Electron Backscatter Diffraction: A Direct Comparison to Local Hardness in an IF Steel Using Nanoindentation," *Mater. Sci. Eng., A*, **527** [29] 7854-64 (2010).
32. P. Jacques, S. Allain, O. Bouaziz, A. De, A.-F. Gourgues, B. Hance, Y. Houbaert, J. Huang, A. Iza-Mendia, and S. Kruger, "On Measurement of Retained Austenite in Multiphase TRIP Steels - Results of Blind Round Robin Test Involving Six Different Techniques," *Mater. Sci. Technol.*, **25** [5] 567-74 (2009).
33. R. Davies, "Influence of Martensite Composition and Content on the Properties of Dual Phase Steels," *Metall. Trans. A*, **9** [5] 671-9 (1978).
34. H.K.D.H. Bhadeshia, *Bainite in Steels*, 2nd ed.; pp. 1-16. IOM Communications, London, UK, 2001.
35. F.S. Lepera, "Improved Etching Technique for the Determination of Percent Martensite in High-Strength Dual-Phase Steels," *Metallography*, **12** [3] 263-8 (1979).
36. J. Angeli, E. Fureder, M. Panholzer, and A.C. Kneissl, "Etching Techniques for Characterizing the Phases of Low-Alloy Dual-Phase and TRIP Steels," *Prakt. Metallogr.*, **43** [10] 489-504 (2006).
37. E. Girault, P. Jacques, P. Harlet, K. Mols, J. Van Humbeeck, E. Aernoudt, and F. Delannay, "Metallographic Methods for Revealing the Multiphase Microstructure of TRIP-Assisted Steels," *Mater. Charact.*, **40** [2] 111-8 (1998).
38. "Standard Test Method for Determining Volume Fraction by Systematic Manual Point Count," ASTM Standard E562-11. American Society for Testing and Materials, West Conshohocken, PA.
39. L. Ryde, "Application of EBSD to Analysis of Microstructures in Commercial Steels," *Mater. Sci. Technol.*, **22** [11] 1297-306 (2006).
40. S.I. Wright and M.M. Nowell, "EBSD Image Quality Mapping," *Microsc. Microanal.*, **12** [01] 72-84 (2006).
41. M. De Meyer, L. Kestens, and B. De Cooman, "Texture Development in Cold Rolled and Annealed C-Mn-Si and C-Mn-Al-Si TRIP Steels," *Mater. Sci. Technol.*, **17** [11] 1353-9 (2001).

42. R. Petrov, L. Kestens, A. Wasilkowska, and Y. Houbaert, "Microstructure and Texture of a Lightly Deformed TRIP-Assisted Steel Characterized by Means of the EBSD Technique," *Mater. Sci. Eng., A*, **447** [1] 285-97 (2007).
43. A. Wilson, J. Madison, and G. Spanos, "Determining Phase Volume Fraction in Steels by Electron Backscattered Diffraction," *Scr. Mater.*, **45** [12] 1335-40 (2001).
44. M.M. Nowell and S.I. Wright, "Orientation Effects on Indexing of Electron Backscatter Diffraction Patterns," *Ultramicroscopy*, **103** [1] 41-58 (2005).
45. T. Waterschoot, L. Kestens, and B. De Cooman, "Hot Rolling Texture Development in CMnCrSi Dual-Phase Steels," *Metall. Mater. Trans. A*, **33** [4] 1091-102 (2002).
46. C. Mesplont and B. De Cooman, "Effect of Austenite Deformation on Crystallographic Texture During Transformations in Microalloyed Bainitic Steel," *Mater. Sci. Technol.*, **19** [7] 875-86 (2003).
47. S. Zaefferer, J. Ohlert, and W. Bleck, "A Study of Microstructure, Transformation Mechanisms and Correlation Between Microstructure and Mechanical Properties of a Low Alloyed TRIP Steel," *Acta Mater.*, **52** [9] 2765-78 (2004).
48. S. Zaefferer, P. Romano, and F. Friedel, "EBSD as a Tool to Identify and Quantify Bainite and Ferrite in Low - Alloyed Al - TRIP Steels," *J. Microsc. (Oxford, U.K.)*, **230** [3] 499-508 (2008).
49. G.F. Vander Voort, *Atlas of Time-Temperature Diagrams for Irons and Steels*; p. 22. ASM International, Novelty, OH, 1991.
50. "Standard Test Method for Knoop and Vickers Hardness of Materials," ASTM Standard E384 (2010e2). American Society for Testing and Materials, West Conshohocken, PA.
51. S. Kimball and P. Mattis, GNU Image Manipulation Program (GIMP) 2.8.10, the GIMP Development Team, 2014.
52. H.S. Kim, "On the Rule of Mixtures for the Hardness of Particle Reinforced Composites," *Mater. Sci. Eng., A*, **289** [1] 30-3 (2000).
53. G. Bansal and A. Heuer, "On a Martensitic Phase Transformation in Zirconia (ZrO<sub>2</sub>) - II. Crystallographic Aspects," *Acta Metall.*, **22** [4] 409-17 (1974).
54. O. Ruff, F. Ebert, and E. Stephen, "Contributions to the Ceramics of Highly Refractory Materials: Li. System Zirconia-Lime," *Z. Anorg. Allg. Chem.*, **180** [1] 215-24 (1929).
55. P. Kelly and C. Ball, "Crystallography of Stress - Induced Martensitic Transformations in Partially Stabilized Zirconia," *J. Am. Ceram. Soc.*, **69** [3] 259-64 (1986).

56. R. Garvie, R. Hannink, and R. Pascoe, "Ceramic Steel?," *Nature*, **258** [5537] 703-4 (1975).
57. D.J. Green, R.H. Hannink, and M.V. Swain, *Transformation Toughening of Ceramics*, 1st ed.; pp. 57-93. CRC Press, Medford, MA, 1989.
58. H.K.D.H. Bhadeshia, *Worked Examples in the Geometry of Crystals*, 2nd ed.; pp. 12-24. Institute of Materials, Brookfield, VT, 2001.
59. W. Kriven, W. Fraser, and S. Kennedy, "The Martensite Crystallography of Tetragonal Zirconia," *'Science and Technology of Zirconia'. Proc. 1 st. Int. Conf. held at Cleveland, Ohio, June 16-18, 1980. Advances in Ceramics*, **3** 82 (1980).
60. P.M. Kelly and L.F. Rose, "The Martensitic Transformation in Ceramics - Its Role in Transformation Toughening," *Prog. Mater Sci.*, **47** [5] 463-557 (2002).
61. M. Hayakawa, K. Adachi, and M. Oka, "Crystallographic Analysis of the Monoclinic Herringbone Structure in an Arc-Melted ZrO<sub>2</sub>-2 mol% Y<sub>2</sub>O<sub>3</sub> alloy," *Acta Metall. Mater.*, **38** [9] 1753-9 (1990).
62. M. Hayakawa, N. Kuntani, and M. Oka, "Structural Study on the Tetragonal to Monoclinic Transformation in Arc-melted ZrO<sub>2</sub>-2mol.% Y<sub>2</sub>O<sub>3</sub> - I. Experimental Observations," *Acta Metall.*, **37** [8] 2223-8 (1989).
63. M. Hayakawa and M. Oka, "Structural Study on the Tetragonal to Monoclinic Transformation in Arc-Melted ZrO<sub>2</sub>-2mol.% Y<sub>2</sub>O<sub>3</sub> - II. Quantitative Analysis," *Acta Metall.*, **37** [8] 2229-35 (1989).
64. H.K.D.H. Bhadeshia, *Worked Examples in the Geometry of Crystals*; pp. 51-7. Institute of Materials, Brookfield, VT, 2001.
65. E. Levin and H. McMurdie, *Phase Diagrams for Ceramists*, 3rd ed.; p. 140. The American Ceramic Society, Westerville, OH, 1974.
66. X.-F. Gu, T. Furuhashi, and W.-Z. Zhang, "PTCLab: Free and Open-Source Software for Calculating Phase Transformation Crystallography," *J. Appl. Crystallogr.*, **49** [3] 1099-106 (2016).
67. B.S. El-Dasher and S.G. Torres, "Electron Backscatter Diffraction in Low Vacuum Conditions"; pp. 339-44 in *Electron Backscatter Diffraction in Materials Science*. Springer, Medford, MA, 2009.
68. D.J. Prior, E. Mariani, and J. Wheeler, "EBSD in the Earth Sciences: Applications, Common Practice, and Challenges"; pp. 345-60 in *Electron Backscatter Diffraction in Materials Science*. Springer, Medford, MA, 2009.

69. D.P. Field, "Recent Advances in the Application of Orientation Imaging," *Ultramicroscopy*, **67** [1] 1-9 (1997).
70. N.K. Lassen, D.J. Jensen, and K. Conradsen, "Image Processing Procedures for Analysis of Electron Back scattering Patterns," *Scanning Microsc.*, **6** 115-21 (1992).

## APPENDICES

### A. The calculation of shape strain and the lattice invariant strain for martensitic transformation

According to Bowles-Mackenzie theory,<sup>22</sup> the equation (7) can be rewritten as:

$$SL^{-1} = RB = S_1 = SL_2 \quad (14)$$

where  $L_2$  can be expressed as:

$$L_2 = I + d_2 p_2' \quad (15)$$

where  $d_2$  is the direction of the lattice invariant strain (L) and  $p_2'$  is the normalized plane of L. By inserting the two elements (plane and direction) into equation 13, the lattice invariant strain can be calculated. Both  $S$  and  $L_2$  are invariant plane strain, so the intersection of the two invariant planes is an invariant line, and  $S_1$  is an invariant line strain.

For the invariant line strain  $S_1$ , suppose  $x_i$  is the unit vector which is parallel to the invariant line, and  $n_i'$  is the normalized plane which is vertical to the  $x_i$ . For  $x_i$  and  $n_i'$ , they satisfy three equations, separately:

$$x_i' x_i = 1 \quad (16)$$

$$x_i' B^2 x_i = 1 \quad (17)$$

$$p_2' x_i = 0 \quad (18)$$

where  $x_i'$  indicates the transpose of  $x_i$ .

From the three equations above, two solutions of  $x_i$  can be obtained.

$$n_i' n_i = 1 \quad (19)$$

$$n_i' B^{-2} n_i = 1 \quad (20)$$

$$n_i' d_2 = 0 \quad (21)$$

From the three equations above, two solutions of  $n'_i$  can be obtained.

There are four combinations of  $x_i$  and  $n'_i$ , so there are four solutions for the invariant line strain  $S_1$ . However, for the calculation of  $S_1$ , a rotation matrix ( $R_0$ ) also needs to be known. The rotation matrix satisfies the two equations below:

$$R_0 x_i = x_i \quad (22)$$

$$n'_i R_0^{-1} = n'_i \quad (23)$$

In addition, for solving the rotation matrix, the properties of an orthogonal matrix needs to apply so that the crystal coordinate matches the Cartesian coordinate system.<sup>66</sup> The solving of the rotation matrix  $R_0$  is bothersome by hand. The computer is usually used for the assistance of the calculation.

When the invariant line strain  $S_1$  is calculated, the shape strain ( $S$ ) and the lattice invariant strain ( $L$ ) can be calculated. Suppose  $p'_1$  is the normalized invariant plane of the shape strain, and  $d_1$  is the displacement vector of the shape strain.  $d_1$  can be calculated by the equation below:

$$d_1 = \frac{S_1 d_2 - d_2}{p'_1 d_2} \quad (24)$$

The magnitude of the shape strain is equal to  $|d_1|$ .

Let  $d'_2$  to be the direction of  $L_2$  which is the inverse of the lattice invariant strain ( $L$ ).  $d'_2$  can be calculated by the equation below:

$$d'_2 = \frac{y - S_1^{-1} y}{p'_2 y} \quad (25)$$

where  $y$  is an arbitrary vector in the invariant plane  $p'_1$ . The magnitude of the shape strain is equal to  $|d'_2|$ .

**B. The procedure of simulating pole figure in PTCLab to represent orientation relationship for tetragonal to monoclinic phase transformation in 10 mol% Ce-ZrO<sub>2</sub>.**

Taking variant *BCA* as an example, the steps of operation in PTCLab are that, (1) Click the “stereo proj.” button of the monoclinic phase; (2) on the right of the window, for the pole figure information, input [100] as the Projection Direction, and [010] as the Horizontal Direction; (3) choose U V W (direct) as the plot type; (4) in the “Add Data” region, click the ellipsis behind SP, and then in the pop-up window, input [010] in the pole region and click “OK”, a blue point will appear in the pole figure of the monoclinic phase, and it represents the  $[010]_m \sim || [1\bar{1}0]_t$  relationship for correspondence variant *BCA*. In the same way, the parallel relationship for the other seven variants can be plotted in this pole figure. In this way, the pole figure used to denote the  $[010]_m \sim || [1\bar{1}0]_t$  relationship for correspondence A is created. For each correspondence, there are two kinds of orientation relationships. In the OR of series 1, the parallel relationships are that the  $(001)_m$  plane parallel to the related tetragonal plane, the  $[100]_m$  direction parallel to the related tetragonal direction, and the  $[010]_m$  direction parallel to the related tetragonal direction; in the OR of series 2, the parallel relationships are that the  $(100)_m$  plane parallel to the related tetragonal plane, the  $[001]_m$  direction parallel to the related tetragonal direction, and the  $[010]_m$  direction parallel to the related tetragonal direction.<sup>60</sup> By the way showed above, these parallel relationships for each OR can be presented in related pole figures.

**C. TSL OIM DC 7 software setting ahead of EBSD data collection for 10 mol% Ce-ZrO<sub>2</sub>.**

Before data collection, the points need to note for the setting in the TSL OIM DC 7 are: (1) load the two monoclinic and tetragonal bmt files in the “Phase” window, choose  $(0\bar{1}1)$ ,  $(0\bar{2}0)$ ,  $(1\bar{1}\bar{2})$ ,  $(2\bar{2}0)$  and  $(1\bar{2}\bar{1})$  as the reflectors for tetragonal phase, and choose  $(1\bar{1}\bar{1})$ ,  $(1\bar{1}1)$ ,

(202), ( $2\bar{2}0$ ), ( $30\bar{2}$ ), ( $0\bar{2}2$ ), ( $0\bar{2}\bar{2}$ ), ( $1\bar{3}1$ ), ( $10\bar{4}$ ) and ( $3\bar{1}1$ ) as the reflectors for monoclinic phase; (2) in the “hough” window, choose 10 as the Max Peak Count.

**D. Software setting of plotting pole figures in TSL OIM Analysis 7 to show orientation relationship for tetragonal to monoclinic phase transformation in 10 mol% Ce-ZrO<sub>2</sub> experimentally.**

The collected data was then analyzed by TSL OIM Analysis 7 to show the morphology and ORs. The steps to analyze the ORs in each parent grain are that: (1) a single tetragonal grain was extracted from the collected data (2) this grain was rotated to orient the tetragonal phase as the reference frame, which is the [001] direction of the crystal coordinate parallel to the sample normal direction, the [ $1\bar{1}0$ ] direction parallel to the A1 direction and the [110] direction parallel to the A2 direction; (3) plot the (100), (001), [100], [010] and [001] pole figures separately for the monoclinic phase.

**E. An example to show the band finding via Hough transform**

As an example, the pattern shown in Figure 41 was analyzed on the Hough page of the TSL OIM DC 7 software. Figure 41a shows the pattern after background noise subtraction. Figure 41b shows the band finding via Hough transform. Figure 41c shows the indexing of the pattern with CI and Fit value. Figure 41d shows the setting of the Hough page. Table X shows the positions ( $\theta$ ,  $\rho$ ) of the ten bands located by Hough transform, the measured bandwidth and the information of the reflectors in the tetragonal phase look-up table. From Figure 41b, it can be seen that the band position is found correctly by Hough transform, while table VI showed that the measured bandwidth is not the same as in the look-up table. The indexing of the pattern is via a voting

scheme<sup>44</sup>. Even though the d-spacing are not corresponding between the measured one and the look-up table, it can get a good CI as Figure 41c shows.

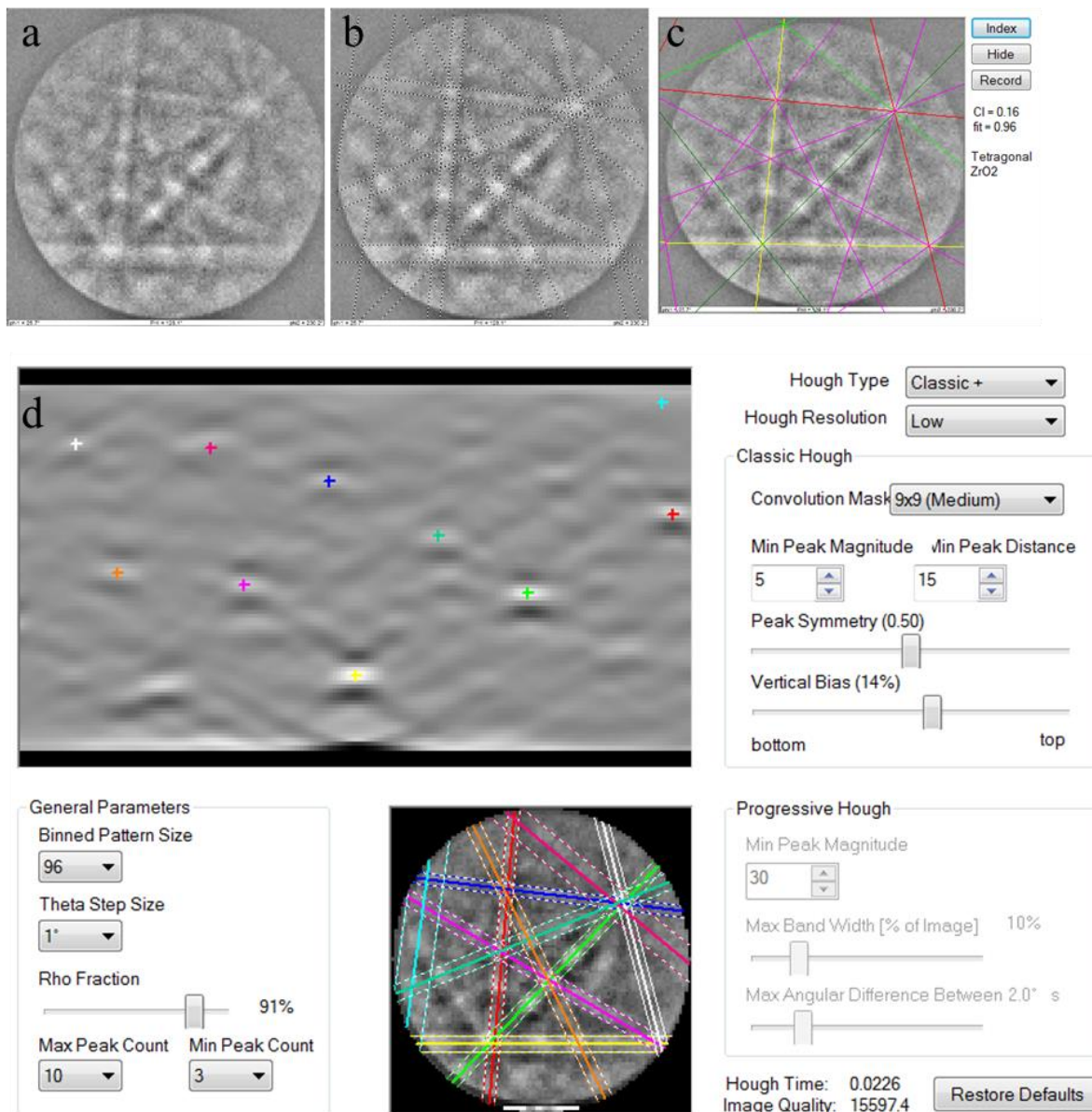


**Figure 40.** (a) the Kikuchi pattern after background noise subtraction; (b) the band finding via Hough transform; (c) the indexing of the pattern with CI and Fit value; and (d) the setting of the Hough page.

**Table X.** The Positions of the Ten Bands Located by Hough Transform, Together with Their Corresponding Reflectors, and the Information of the Reflectors in the Look-Up Table of the Tetragonal Phase in 10 mol% Ce-ZrO<sub>2</sub>

<b>Color</b>	<b>Position (<math>\theta</math>, <math>\rho</math>)</b>	<b>Measured d- spacing</b>	<b>(hkl) in the tetragonal look- up table</b>	<b>d-spacing value in the look-up table</b>
<b>Red</b>	(175.0, 13.0)	1.66	0 $\bar{2}$ 0	1.815
<b>Green</b>	(136.0, -6.0)	1.46	2 $\bar{2}$ 0	1.283
<b>Yellow</b>	(90.0, -26.0)	1.71	0 $\bar{2}$ 0	1.815
<b>Blue</b>	(83.0, 21.0)	1.68	0 $\bar{1}$ 1	2.981
<b>Magenta</b>	(60.0, -4.0)	1.35	1 $\bar{2}$ $\bar{1}$	1.55
<b>Cyan</b>	(172.0, 40.0)	0.699	n/a	n/a
<b>White</b>	(15.0, 30.0)	1.78	0 $\bar{1}$ 1	2.981
<b>Pink</b>	(51.0, 29.0)	0.737	1 $\bar{1}$ $\bar{2}$	1.83
<b>Turquoise</b>	(112.0, 8.0)	1.23	1 $\bar{2}$ $\bar{1}$	1.55
<b>Orange</b>	(26.0, -1.0)	1.3	1 $\bar{2}$ $\bar{1}$	1.55